Microfabrication Approaches for Understanding the Role of Vascular Mechanics
in Progressive Diseases

A DISSERTATION
SUBMITTED TO THE FACULTY OF
UNIVERSITY OF MINNESOTA
BY

Eric Scott Hald

IN PARTIAL FULFILLMENT OF THE REQUIREMENTS
FOR THE DEGREE OF
DOCTOR OF PHILOSOPHY

Dr. Patrick W. Alford, Advisor

August 2016

Acknowledgements

While this work encompasses the last six years of my life, it really would not have been possible without all of the tremendous love and support from the very beginning that I have received from family, friends, teachers, and mentors over the last 29+ years. To those I mistakenly omit, thank you.

First, I must express my gratitude to my advisor, Dr. Patrick Alford. I truly feel like we set forth an a mutual journey five and a half years ago in starting his lab and thank him for placing his trust and faith in me as his first student. Through all the trials and tribulations, he has been a rock and calm, steadying force. Without his mentorship, patience, attention to detail, and sarcasm, I would not have made it to this point. I am truly a better student, scientist, and writer thanks to him and his tireless efforts.

I would also like to thank my thesis committee members for their guidance, time, and support. Dr. Barocas, Dr. Odde, and Dr. Divani. Thank you. Additionally, I would like to thank Dr. Netoff and Dr. Lim for their occasional contributions in signal and noise processing and Dr. Wood for microfluidics assistance.

I need to expound on my gratitude for Victor (Barocas). He was instrumental in luring me to the University of Minnesota, in addition to warmly accepting me into his research group in Summer 2010, prior to my start in the program. In three short months, I learned so much from him, but more importantly, from his lab members, the truest reflection of a mentor.

Kerianne and Zaw. What can I say? You two are the epitome of wonderful colleagues, but more importantly, great supportive friends. Thank you for all of the laughs, metaphorical cries, general ridiculousness, The Oath, and yes, scientific advise/collaboration. Being a member of the Alford Lab has been the best team experience of my life, and that is thanks to you two (and Pat). Thank you to Nick for joining us and for hitting the ground running. I know the lab is in great hands

Dedication

To Dick, Thelma, Bernie, and Mary Ann

For showing me the true value of love, dedication, stubbornness, and hard work

Abstract

Vascular disease is a common cause of death that typically results from long-term alteration of vessel structure and function. The underlying mechanisms that lead to pathologic changes in the vasculature are largely unclear, especially in progressive diseases of the cerebral vessels. With the growing prevelance of blast traumatic brain injury in modern warfare, never before has investigation of cerebral vascular disease been more pertinent. Here, we focus on the development of microfabrication experimental approaches for probing the critical mechanical and biochemical pathways involved in progression of diseases, such as cerebral vasospasm, subarachnoid hemorrhage, and Alzheimer's disease, that often result from TBI.

First, we develop a microfluidic patterned deposition technique for studying functional mechanics in chronic vascular disease at the tissue scale. We modify substrate surfaces with genipin, a natural crosslinker, to extend culture times of *in vitro* vascular tissues that mimic native tissue structure and function. We successfully validate our technique, showing maintenance of patterned structural alignment and mechanical function over the course of two weeks.

Lastly, we investigate the relationship between vascular disease and Alzheimer's disease. Amyloid beta is a key precursor in the development of Alzheimer's disease that accumulates in neuronal and cerebrovascular tissue and can result in neurodegeneration. During the development of cerebral amyloid angiopathy (CAA), which is present in over 80% of Alzheimer's disease cases, amyloid beta plaques form in the cerebral vessel walls and lead to severe attenuation of physiologic vasodilation. We measured the effect of amyloid beta treatment on vascular smooth muscle cell functional contractility using a single-cell traction force microscopy technique and developed a thin-walled arterial model for growth and remodeling response to mechanical perturbations. We found that amyloid beta induces a reduction in vascular smooth muscle cell mechanical output. We implemented this loss of function into a constrained mixture arterial

model that suggests vessel growth and remodeling, in response to amyloid beta-mediated alteration of smooth muscle function, can lead to an inability of cerebral vessels to vasodilate. Our findings provide a possible explanation for the vascular injury and malfunction often associated with the development of neurodegeneration in Alzheimer's disease.

Table of Contents

ix

List of Figures

Chapter 1. Introduction

Vascular disease is a broad canopy under which a wide variety of disease mechanisms, afflicted areas of the human body, and complications reside. Given the continuous flow of blood and importance of its delivery of nutrients and oxygen to all tissues of the body, disruptions in vascular function can have devastating consequences. This is especially true in the cerebral vasculature, due to the limited regenerative capacity of brain tissue. With the advent of improved armor, modern warfare has led to a striking increase in blast traumatic brain injuries [1]. Soldiers who typically died in past wars are now surviving, yet sustaining invisible injuries that manifest themselves in lost brain function over time. The nature of these injury mechanisms can be difficult to isolate, due to the closely-knit interaction between the cerebral vasculature and neural networks of the brain [2]. Our goal is to develop techniques to allow investigation of the underlying mechanisms that can result in the wide array of downstream progressive diseases that manifest themselves after exposure to blast trauma.

Cerebral arteries, like most tissues, exist as a complex structure composed mainly of cells and extracellular matrix. The unique metabolic loads of brain tissue require cerebral arteries to be highly dynamic in nature [3]. Arteries contract or relax to modify blood flow rates and maintain fluid shear stress [4], a direct correlate to the activity of the tissues to which they deliver blood containing oxygen and nutrients. Thus, the mechanical function of arteries is paramount to the function of the surrounding tissue as a whole. The main contractile component of arteries is the vascular smooth muscle cells **(VSMCs)**, which typically exist in concentric sheets of circumferentially-aligned cells alternating with layers of collagen and elastin in the media layer of arteries [5]. The mechanical function of these cells tends to become perturbed in development of vascular disease. A common theory in vascular function, growth and remodeling theory, suggests that vascular smooth muscle has an ideal stress level which, when perturbed away from, the smooth muscle adapts to return to this so-called target stress [6]. This

1

mechano-adaptation can occur via proliferation or hypertrophy of VSMCs [7, 8] or changes in the active contractile force exerted by the cells within the arterial wall [9]. A method to capture the mechano-adaptive behavior of VSMCs is highly-desirable, as this behavior is often a hallmark of disease progression.

The role of mechanics in VSMC function has been extensively studied. Several experimental techniques can be employed to determine mechanical properties of VSMCs, in addition to direct mechanical stimulation of cells [10]. Mann et al. utilized a flexible micropost array and employed vacuum pressure to apply stretch directly to VSMCs [11]. Traction force microscopy **(TFM)** has been used extensively to assess a wide variety of cell types and their mechanical output in highly-controlled experimental conditions, both in 2-D and 3-D culture [12-14]. However, TFM does not allow for tissue-level assessment of vascular mechanical function. Vascular muscular thin films have been employed to measure stress in a monolayer of highly-aligned, confluence sheets of VSMCs designed to mimic the *in vivo* tissue structure [15].

To investigate the role of vascular mechanics in progressive diseases, we have developed a two-pronged approach. Our first aim is to develop an improved technique for probing vascular mechanics over disease-relevant time courses and in a relatively high-throughput manner. Second, we invoke existing techniques to investigate specific pathological effects on vascular mechanics in a highly-controlled *in vitro* assay. The primary motivation for both aims is the induction of vascular injury that occurs in blast traumatic injury. We investigate the literature findings in depth to frame the many diseases that may arise (Chapter 2). To provide a more relevant system for assessing the chronic nature of most vascular diseases, we develop a microfluidic deposition technique for crosslinking extracellular matrix to PDMS substrates previously used in vascular muscular thin films (Chapter 3) [15].

Next, we attempt to elucidate the effects of blood-borne factors that are released and shown to have higher concentrations in the blood and cerebral spinal

2

fluid after subarachnoid hemorrhage that often occurs with TBI (Chapter 4). These factors are thought to contribute to the development of cerebral vasospasm **(CVS)**, which is a mechanically-characterized vascular disease with acute hyper-contractility, followed by prolonged arterial remodeling that leads to further occlusion of cerebral arteries. CVS is an example of the maladaptive outcomes that often arise from the arterial growth and remodeling response.

Lastly, we turn toward Alzheimer's disease, which has many connections to vascular disease, especially considering the common progression with presentation of cerebral amyloid angiopathy **(CAA)** in which amyloid beta deposits become prevalent in the cerebral vessel walls [16, 17]. The so-called amyloid hypothesis implicates amyloid beta in Alzheimer's disease progression, but it is largely disputed as to how amyloid beta leads to neurodegeneration. We investigate the functional mechanics of VSMCs when exposed to amyloid beta to determine if vascular mechanics may play a critical role (Chapter 5).

Chapter 2. Smooth Muscle Phenotype Switching in Blast Traumatic Brain Injury-Induced Cerebral Vasospasm

This chapter contains material from an invited review article previously published in *Translational Stroke Research* and is reproduced with permission. **Hald ES** and Alford PW. Smooth Muscle Phenotype Switching in Blast Traumatic Brain Injury-Induced Cerebral Vasospasm [18].

2.1 Summary

Due to increased survival rates among soldiers exposed to explosive blasts, blast traumatic brain injury **(bTBI)** has become much more prevalent in recent years. Cerebral vasospasm **(CVS)** is a common manifestation of brain injury whose incidence is significantly increased in bTBI. CVS is characterized by initial vascular smooth muscle cell **(VSMC)** hypercontractility, followed by prolonged vessel remodeling and lumen occlusion, and is traditionally associated with subarachnoid hemorrhage **(SAH)**. But, recent results suggest that mechanical injury during bTBI can cause mechanotransduced VSMC hypercontractility and phenotype switching necessary for CVS development, even in the absence of SAH. Here, we review the mechanisms by which mechanical stimulation and SAH can synergistically drive CVS progression, complicating treatment options in bTBI patients.

2.2 Introduction

Traumatic brain injury **(TBI)** affects as many as 1.7 million people in the United States each year [19]. Most TBIs are caused by blunt force blows to the head, but more rarely, bTBI can occur following exposure to an explosive blast wave. Due to the increased use of improvised explosive devices, along with

4

improved survival rates, soldiers returning from Iraq and Afghanistan suffer a higher prevalence of bTBI than those of previous wars [1, 20, 21]. Thus, it is important to determine the mechanisms of bTBI and subsequent neurodegeneration, which may vary from those of more common TBI injuries.

CVS is a secondary manifestation of TBI whose incidence is increased in bTBI, compared to other forms of TBI [22, 23]. CVS is characterized by acute vascular hypercontraction followed by chronic cell proliferation and extracellular matrix remodeling, typically resulting in delayed ischemia [24-26]. For chronic CVS to occur, VSMCs in cerebral arteries must undergo phenotypic switching from a contractile to a synthetic phenotype [26, 27]. Both SAH [26] and mechanical stimulation [27] can induce phenotypic transformation necessary to prolong CVS. These competing stimuli provide a complex signaling milieu that may lead to increased incidence and earlier onset of CVS in bTBI patients. Here, we review recent findings in the area of cerebral vascular mechanics associated with TBI and vascular injury, via modulation of VSMC phenotype. We then discuss some recent developments in clinical treatments of TBI-induced cerebral vasospasm that may be specifically of interest for bTBI patient treatment.

2.3 Acute Vascular Injury in TBI

The pathways of bTBI injury are not currently fully understood, but direct mechanical insult by the transient pressure wave produced by an explosive device clearly plays some role in injury progression. The blast shock wave produces localized particle motion in the tissues it passes through, possibly transducing injury seen in bTBI. The injury may be caused by the wave passing directly through the skull or transmitting through soft tissue from other locations in the body. One provocative hypothesis is that kinetic energy from the blast may enter the body in the abdomen or chest and propagate through large blood vessels to the cerebral vasculature [28] (Fig. 2.1, center). Both rat and swine models exposed to blasts

support this hypothesis, suggesting direct interaction between the head and blast wave and vascular fluid transfer of injury synergistically contribute to bTBI [29, 30]. Blast propagation through the vasculature suggests a greater role for vascular mechanical stimulation in bTBI-induced CVS than in non-blast blunt-force TBI (Fig. 2.2).

Even small changes in mechanical environment can affect cellular function, so unsurprisingly the extreme forces associated with bTBI dramatically affect cells in the neurovascular unit **(NVU)**, which is composed of vascular cells, glial cells, and neurons [31]. In neurons, large strains can induce membrane poration, causing increased intracellular calcium **(Ca^{2+})** levels that lead to calponin upregulation and axonal collapse [32-34]. Small strains at high strain rates can also induce neuronal focal swelling through a similar Ca^{2+}-mediated pathway, suggesting integrin stimulation may also play a critical role in acute neuronal injury in TBI [35].

Blast wave-induced injury in cerebral arteries affects the vessels' acute mechanical function. Primary blast waves in the cerebrovasculature can cause small, focal lesions in the vessels that are distinct from those produced in studies of other forms of TBI [36]. In VSMCs, high-velocity strains can increase intracellular Ca^{2+} levels *in vitro*, resulting in acute hypercontractility, suggesting that that blast alone can elicit an early-stage vasospastic response in VSMCs [27].

Forces applied to cerebral arteries during bTBI via volumetric blood surge can lead to microvessel injury or disruption of the NVU's blood-brain barrier **(BBB)** [36-41], a layer of endothelial cells that limits the entry of harmful blood cells and plasma constituents into the brain tissue [31] (Fig 2.1, center). The resulting SAH, or bleeding in the subarachnoid space, exposes the NVU to whole blood and can cause a range of dysfunction due to induced activation of astrocytes and microglia [42]. In addition, SAH leads to secondary development of CVS. The classical view of SAH-induced CVS suggests that activated platelets in SAH-related extravascular clots are responsible for producing a wide variety of proteins that

6

promote contraction of the injured blood vessel [26], limiting blood loss, and growth of new vascular tissue, accelerating repair [43]. Hemoglobin, found in SAH blood, scavenges the endothelium-produced vasodilator nitric oxide **(NO)**, limiting NO's relaxation effect on VSMCs [44-46]. In addition, common SAH-associated vasoconstrictors, including serotonin [47], thromboxane [48], thrombin [48], and endothelin-1 **(ET-1)** [48-50], may play a role in SAH-CVS progression by inducing increased intracellular calcium and thus, hypercontractility [51], similar to that seen due to mechanical stimulation [27].

Additionally, TBI has been shown to activate endothelial cells [52], and SAH often results in endothelial injury [53], which can affect the ability of cerebral vasculature to adapt to the pathological environment immediately following a TBI. For example, many of the factors released in SAH have been shown to increase synthesis and release of the vasoconstrictor ET-1 by endothelial cells [54] possibly initiating CVS [55]. In addition to this increased ET-1 production, recent results suggest ET-receptors in VSMCs are also affected in CVS. Two subtypes of ET receptors, ET(A) and ET(B), modulate mechanical pathways in VSMCs and endothelial cells. ET(A)-receptor is prevalent in VSMCs and mediates the contractile effects associated with CVS. ET(B)-receptor is responsible for vasorelaxation via stimulation of NO-synthase and downstream NO release from endothelial cells. The ET(B)-receptor signaling cascade is lost in CVS, though the mechanism is not clear [56].

Shortly following bTBI injury, the VSMCs' mechanical function is significantly perturbed. VSMCs are more inherently contractile, while being simultaneously stimulated with elevated vasoconstrictor signaling from the endothelium and extravascular SAH. The resulting hypercontractility increases the stress borne by the VSMCs and causes the vessel lumen to narrow. This hypercontractility by itself is reversible. However, when coupled with vessel remodeling, which can be occur in response to both mechanical stimulation and

SAH, prolonged narrowing of the lumen can occur, leading to the serious pathologies associated with CVS [26].

2.4 Phenotype Switching and Chronic Vascular Injury in TBI

VSMCs express two distinct phenotypes: contractile and synthetic. Healthy homeostatic vessels are predominantly populated with contractile VSMCs, which produce greater contractile forces and minimally migrate, proliferate, or remodel surrounding extracellular matrix **(ECM)**. Synthetic VSMCs, characterized by increased migration, proliferation, and remodeling as well as decreased contractility, are often present in injured vessels [57]. Thus, large-scale remodeling necessary for CVS progression requires phenotypic switching in VSMCs [58, 59]. Among the stimuli that can induce phenotype switching in VSMCs are mechanical stimulation [27, 60, 61] and a number of clot-related factors present in SAH [25, 26, 48-50, 62-67]. Given the extreme mechanical loads and presence of SAH in bTBI [23], the elevated incidence of CVS in bTBI suggests a possible synergistic mechanism between mechanotransduced and SAH-induced CVS may be at work.

2.5 Mechanics and VSMC Phenotype

A long-standing theory in biomechanics posits that tissues maintain a homeostatic preferred stress and that perturbations in their mechanics induce them to remodel to return their stress to this preferred value [68]. An example of this mechanism is thickening and stiffening of arteries in hypertension [6, 69-73]. For this remodeling to occur, mechanics must modulate VSMC function. Many studies have shown a complex milieu of mechanical effects on phenotype behavior, suggesting a mixture of VSMC phenotype in arterial walls undergoing pathological strains. *In vivo* hypertensive arteries show increased expression of matrix metalloproteinases **(MMPs)**, consistent with a switch toward a synthetic

population [74, 75]. Conversely, serum response factor **(SRF)** and myocardin are prevalent transcription factors upregulated in hypertension and CVS, as their overexpression produces the contractile VSMC phenotype [76]. *In vitro* cyclic strains induce both contractile [77, 78] and synthetic [79, 80] shifting, depending on the experimental conditions. Large strains have been shown to result in VSMC behavior often associated with the synthetic phenotype, such as hypertrophy and increased matrix synthesis [81]. VSMCs have also been shown to modulate their phenotype in response to changes in substrate mechanics [82], with higher ECM stiffness inducing increased cell-substrate interaction and increased synthetic phenotype expression [83]. Furthermore, changes in ECM mechanics affect cell morphology [84] and motility [85], which can correlate with phenotype transformation. Taken together, these data suggest that phenotype switching plays an important role in tissue stress maintenance.

A population study of bTBI patients found that post-traumatic vasospasm can occur secondary to primary blast alone, suggesting that mechanotransduced CVS can occur independent of SAH in bTBI [86]. This observation is supported by *in vitro* results wherein vascular tissues exposed to blast-like stretch showed differences in functional contractility and phenotype expression, depending on the severity of the stretch, one day post-blast injury [27]. Mild injury induced hypersensitivity to ET-1 stimulation, while severe injury decreased response to ET-1. Consistent with these results, key contractile phenotype markers were down-regulated in the severe injury, suggesting that mechanical injury alone could drive phenotype switching necessary to prolong CVS. Notably, inhibition of tissue hypercontractility with a rho kinase inhibitor reduced phenotype switching following blast-like stretch [27]. Considering acute injury, hypercontractility, hypertension, and hypotension [87], which occur after blast, mechanically-induced growth and remodeling likely play a role in the progression of CVS after blast injury.

9

2.6 SAH and VSMC Phenotype

While CVS can occur in bTBI in the absence of SAH, normally SAH is present, so its contribution must also be considered. SAH-borne factors can modulate VSMC behavior via a variety of signaling cascades that shift VSMC phenotype. These pathways are quite complex, complicating determination of exactly how SAH leads to CVS.

Mitogens, such as transforming growth factor beta **(TGF-β)**, platelet-derived growth factor **(PDGF)** [74, 75], and ET-1 [88] (which can act as either a mitogen or a vasoconstrictor) promote VSMC proliferation and modulate VSMC phenotype. TGF-β induces expression of cytoskeletal genes associated with the VSMC contractile phenotype [89]. This switching occurs at least 16 hours post-exposure, consistent with delayed SAH-associated hypercontractility in CVS. TGF-β-induced increased expression of these genes coincides with that of cysteine and glycine-rich protein 2 **(CSRP2)**, a smooth muscle cell-restricted signaling molecule. This increase in CSRP2 is counter to the severe downregulation of CSRP2 typically seen when SMC proliferation is increased [90], further suggesting TGF-β acts to shift SMCs toward the contractile phenotype. TGF-β also directly upregulates CSRP2 in VSMCs by activating transcription factor 2 [91]. Thus, the pathologic exposure of SMCs to TGF-β, a common component of whole blood, could contribute to increased contractility via a phenotype transformation. In contrast, PDGF stimulates downregulation of SMC contractile markers, such as smooth muscle myosin heavy chain **(SM-MHC)** and smooth muscle α-actin **(SM-α)**, indicating a switch from contractile to synthetic phenotype [92-94]. Additionally, MT1-MMP, an enzyme responsible for degradation of ECM proteins, in conjunction with PDGF, contributes to the VSMC synthetic phenotype, as MT1-MMP deficiency results in decreased VSMC remodeling [95]. Further work elucidating the exact mechanism or mechanisms by which PDGF modulates transcription and SMC phenotype has been extensively reviewed [59].

Activation of store-operated Ca^{2+} channels **(SOCC)** is also associated with occurrence of CVS in a SAH rat model [96]. This activation occurs as a result of ET-1 stimulation, which is heightened in SAH. Various studies have also implicated SOCC in VSMC phenotype transformation, as VSMCs' contractile-to-synthetic switching is greatly increased by store-operated Ca^{2+} entry [97, 98]. Considering these findings, the complex role of ET-1 in both hypercontractility and VSMC phenotype switch from contractile to synthetic and its relation to calcium handling suggest the significant importance of ET-1 in SAH-associated CVS.

Both hypoxia and direct endothelial damage due to SAH upregulate MMP-9 and vascular endothelial growth factor **(VEGF)**, and induce increased VSMC proliferation [65]. Studies in adult sheep arteries found reduced levels of contractile phenotype marker SM-MHC colocalized to SM-α in hypoxic conditions as compared to normoxic, suggesting hypoxia plays a role in phenotypic transformation leading to vascular remodeling [99]. In fetal arteries, in addition to VEGF itself, hypoxia can also directly increase expression of VEGF receptors [100]. This has a similar effect on contractile phenotypic markers, suggesting the importance of VEGF and its receptors in a positive feedback mechanism influencing VSMC phenotype transformation and cerebral vascular remodeling that is associated with CVS and hypoxia.

2.7 Mechanico-Chemical Synergy in bTBI-induced CVS

Computational modeling provides insight into the possible synergy of mechanical and SAH pathways in bTBI-induced CVS. Clinically, bTBI accelerates CVS onset relative to SAH [23]. Mechanically-induced CVS can be initiated as soon as 24 hours post-injury *in vitro* [27], whereas SAH-induced CVS typically occurs over 3-7 days [101]. These temporal differences could play a key role in the mechanico-chemical synergy in CVS progression proposed by Humphrey et al. [26]. In this theory, several remodeling steps occur in response to hypercontractility

11

present in the early stages of CVS, which initially intensify hypercontractility, but eventually aide in returning the artery to a desired stress state. SAH clot-related mitogens, such as PDGF and TGF-β, promote VSMC proliferation and migration [24], causing a shift in the active force-length curve and leading to further tissue remodeling. Maladaptive vessel wall thickening and stiffening, which serve as a long-term means for returning the vessel to its normal state [6, 69-73], occur but are initially superseded by the shift in the force-length curve [26]. Flow dynamics, along with the altered mechanics of the remodeled vessel, continue to induce cell and matrix remodeling, eventually returning the vessel to its normal dimensions and stress state [26]. Computational modeling also predicts the importance of phenotypic switching in mechanotransduced CVS progression in bTBI, suggesting that VSMCs in CVS exhibit mixed populations of hypercontractile and synthetic cells [27]. Taken together, this work suggests that mechanical growth and remodeling theory can be used to better understand the gross mechanisms of bTBI-induced CVS progression.

2.8 Clinical Treatment of Vascular Injuries Associated with TBI

Treatments for CVS can target either short-term hypercontractility or long-term remodeling. Proposed treatments of CVS-associated sustained VSMC contraction have primarily targeted the Rho/Rho-kinase pathway. Pharmaceutical targeting of single proteins in the pathway, such as RhoA with statin or Rho-kinase with fasudil, has proven insufficient in attenuating CVS after SAH [102, 103]. Recent combination therapy using pitavastatin and fasudil showed increased attenuation of CVS in rabbit arteries, suggesting similar synergistic targeting of the Rho/Rho-kinase pathway may prove beneficial in combating CVS hypercontractility [104]. Direct targeting of calcium channels via calcium channel blockers, such as nicardipine [105, 106] and nimodipine [107], has also been

employed in the treatment CVS, though general outcomes do not necessarily improve as a result of such treatment.

TBI proteomics provides another significant research area of interest, both in pharmaceutical treatment of TBI and in cross-referencing with the biochemical pathways initiated by SAH [108]. A review of TBI mechanisms and current diagnostic methods found that a panel of biomarkers associated with damaged neurons and/or astrocytes shows the greatest promise for determining the type and level of TBI experienced by patients [109]. The high sensitivity and acute presence in the blood post-injury of these biomarkers make them a suitable target for expedited diagnosis via field diagnostic biosensors [109]. This is of particular interest for TBIs sustained on the battlefield.

Recent proposed gene therapies have also shown promise in attenuating CVS in SAH. For example, heme-oxygenase-1 **(HO-1)** is critical in heme catabolism, which can reduce the contractile effect of hemoglobin after SAH. Recently, transduction of HO-1 fused with a common protein transduction domain sequence of 11 consecutive arginine residues allowed integration of the fused protein into the membranes of arterial cells, significantly attenuating CVS after SAH [110]. Magnesium sulfate provides another alternative treatment for combating CVS hypercontractility and its pathological effects downstream of SAH. Magnesium sulfate blocks the release of amino acids that promote hypercontractility downstream of initial SAH, and acts as a direct vasodilator, maintaining cerebral blood flow in a physiologically-suitable range for maintaining tissue homeostasis [111]. Magnesium sulfate treatment has been shown to improve outcomes in SAH patients via reduction of delayed ischemia [112].

Specific factors and pathways associated with SAH have been targeted for therapeutic treatment of SAH-induced CVS. Treatment of CVS with ET-1 antagonists, such as clazosentan, has proven effective, further elucidating the critical role of ET-1 in CVS development and progression [113]. However, Clazosentan to Overcome Neurological Ischemia and Infarct Occuring after

Subarachnoid Hemorrhage (CONSCIOUS) clinical trials have not shown improved SAH outcome [114-116]. Treatment with a phosphodiesterase type III inhibitor, cilostazol, resulted in attenuation of vasospastic effects in concert with prevention of phenotype transformation [117], suggesting that SAH-induced CVS is maintained via phenotype switching. Hyperbaric oxygen treatment has also been shown to limit the damage to neural tissue caused by SAH-induced CVS [118]. Recent work has further elucidated a possible mechanism for this attenuation via decreased expression of hypoxia-inducible factor-1α and downstream inhibition of matrix MMPs [119] responsible for cleaving ECM proteins and tight junctions connecting endothelial cells. Downregulation reduces this effect, limiting BBB disruption and reducing damage to neural tissue. MMP inhibition has also been found to constrain rapid changes in vessel mechanical properties due to changes in flow dynamics and mechanical stimulation in carotid arteries [120, 121]. A similar mechanism may be at play in the cerebral vasculature, as MMPs have also been implicated in VSMC phenotype transformation. To date, no singular treatment has shown the ability to unilaterally attenuate the effects of CVS.

2.9 Alternative Pathomechanisms in bTBI

While CVS can directly lead to patient mortality, it is unclear whether it plays a primary role in long-term bTBI outcome in survivors. Reviews of clinical vasospasm treatment have shown limited improvement in patient outcome [122]. Ischemia can lead to cerebral infarction in TBI and CVS patients, but recent work suggests that the importance of CVS in delayed ischemia is limited [122-125]. Cerebral infarction, conversely, can have a direct negative effect on clinical outcomes, independent of vasospasm [125] and is a better determinant of outcome than CVS [124]. Cortical spreading ischemia follows SAH and contributes directly to focal necrosis of brain tissue [123]. In addition, other pathomechanisms may play significant roles in bTBI patient outcome, rendering treatment of CVS less

14

effective. Blast forces can directly injure neural tissue via metabolic disturbances [126, 127] and astroglial-induced neuronal swelling [128]. Activation of the neuroendocrine-immune system due to post blast injury release of autacoids into the blood also directly contributes to induction of secondary brain injury [129]. Further work is needed to fully elucidate the relative contributions of different pathomechanisms to secondary brain injury in bTBI and determine the best course of treatment to prevent and combat severe complications that result from bTBI.

2.10 Conclusion

With the rising incidence of bTBI worldwide, it is imperative to better understand the injury mechanisms that drive its progression. Due to the unique mechanical loading on cerebral vasculature during blast injury, mechanisms of bTBI-induced CVS likely vary from those of more traditional CVS cases, likely accounting for the increased incidence of CVS in bTBI patients. Further exploration of the synergistic influence of mechanics and SAH in VSMC phenotype switching in CVS is vital for developing appropriate treatment strategies for future bTBI patients.
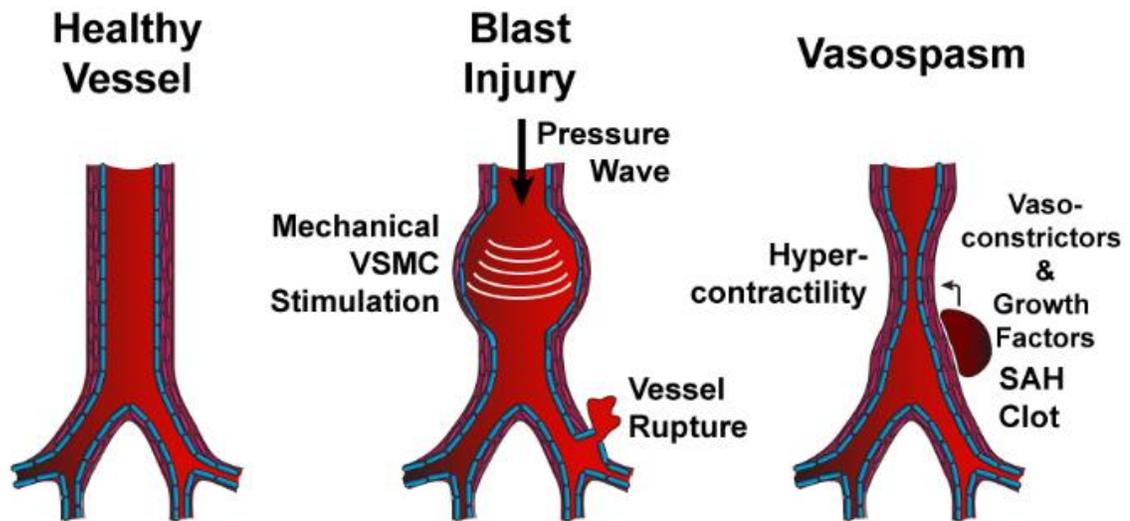
Figure 2.1. Acute injury of vasculature due blast injury.
Blast pressure waves propagate through the healthy vessel, resulting in mechanical VSMC stimulation and, in severe cases, vessel rupture and subsequent SAH. Clotting factors released from the SAH clot result in acute hypercontractility and remodeling consistent with CVS progression.
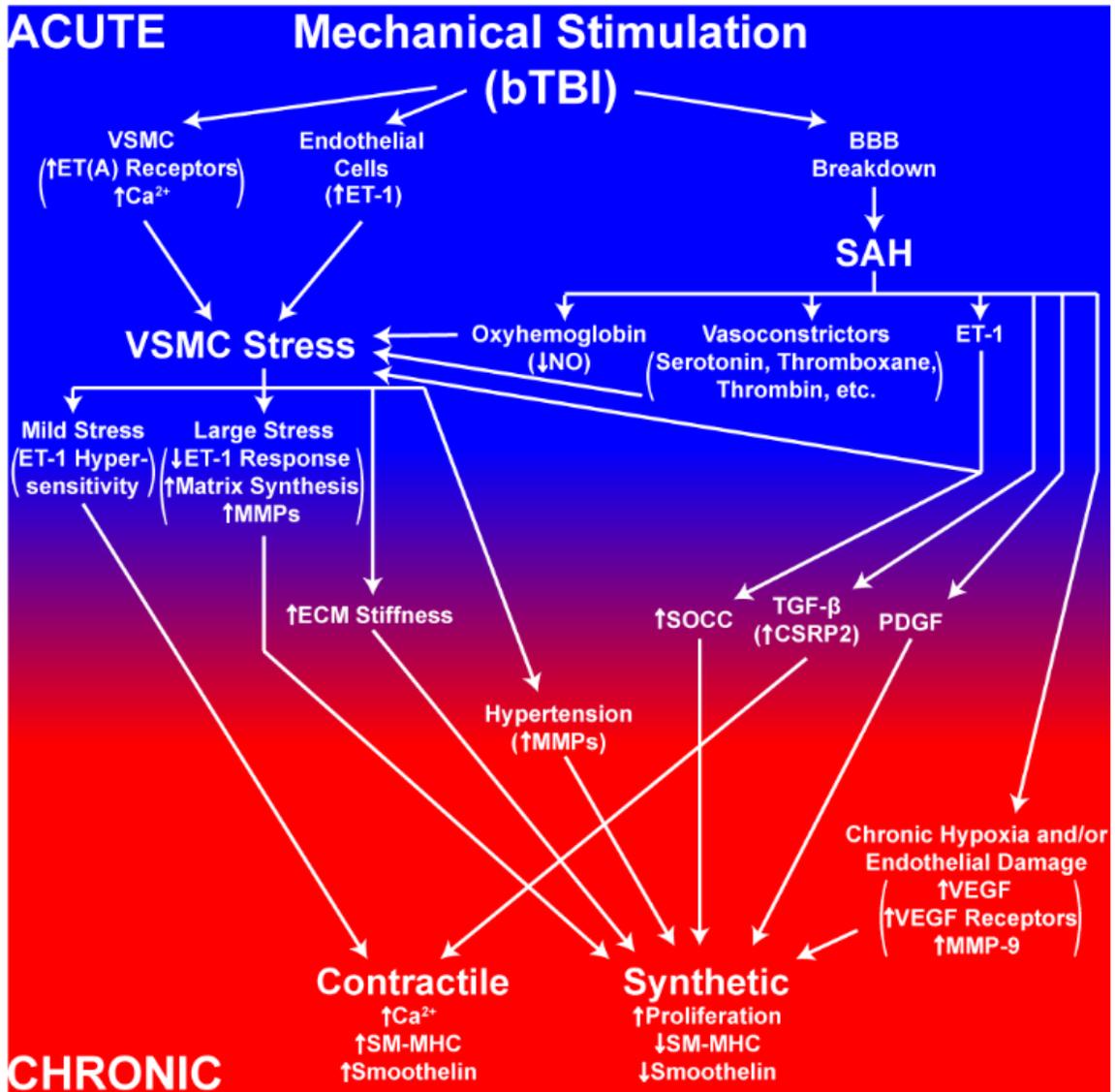
Figure 2.2. Schematic of complex milieu of mechanical and biochemical pathways linked to VSMC phenotype transformation as a result of bTBI. Acute mechanisms are in blue at top, chronic mechanisms/effects are in red at bottom.

Chapter 3. Microfluidic Genipin Deposition Technique for Extended Culture of Vascular Muscular Thin Film Contractility Assays

This chapter contains material previously published in *Biofabrication* and is reproduced with permission. **Hald ES**, Steucke KE, Reeves JA, Win Z, and Alford PW (2014) Long-Term Vascular Contractility Assay Using Genipin-Modified Muscular Thin Films [130]. © IOP Publishing. Reproduced with permission. All rights reserved.

3.1 Summary

Vascular disease is a leading cause of death globally and typically manifests chronically due to long-term maladaptive arterial growth and remodeling. To date, there is no *in vitro* technique for studying vascular function over relevant disease time courses that both mimics *in vivo*-like tissue structure and provides a simple readout of tissue stress. We aimed to extend tissue viability in our muscular thin film contractility assay by modifying the polydimethylsiloxane **(PDMS)** substrate with micropatterned genipin, allowing extracellular matrix turnover without cell loss. To achieve this, we developed a microfluidic delivery system to pattern genipin and extracellular matrix proteins on PDMS prior to cell seeding. Tissues constructed using this method showed improved viability and maintenance of *in vivo*-like lamellar structure. Functional contractility of tissues fabricated on genipin-modified substrates remained consistent throughout two weeks in culture. These results suggest that muscular thin films with genipin-modified PDMS substrates are a viable method for conducting functional studies of arterial growth and remodeling in vascular diseases.

18

3.2 Introduction

Cardiovascular disease accounts for an estimated 17.3 million deaths annually and is the leading cause of death globally [131]. Vascular diseases are rarely acute dysfunctions, but are instead slow-developing and often chronic. For example, cerebral vasospasm is typically diagnosed 3-7 days posttrauma [18, 132] and can persist for up to two weeks [133]. Atherosclerosis and aneurysms can develop for years prior to clinical complications [134, 135]. One hallmark of these diseases is the pathologic perturbation of vascular smooth muscle cell **(VSMC)** function. In the complex milieu of an *in vivo* artery, it is often difficult to isolate pathways that lead to VSMC dysfunction. Thus, it is desirable to develop *in vitro* methods with more highly-controlled experimental conditions. To date, an *in vitro* model that can explore vascular function over physiologically-relevant time scales of vascular pathologies does not exist.

The need to isolate underlying pathological mechanisms has long driven researchers toward development of reductionist *in vitro* methods, but with the consequence of lost functional integrity and system-level complexity. But, recent advances in organ-on-a-chip technologies have revolutionized the way researchers develop *in vitro* models for pathophysiological investigation by employing microfabrication and microfluidic techniques to control flow dynamics and temporospatial microenvironments [136, 137]. To date, liver-, kidney-, lung-, and heart-on-a-chip systems, which more closely mimic the tissue-level chemical, mechanical, and electrophysiological environments of *in vivo* organ systems, have shown great promise as pharmaceutical screening assays [138-141]. Arteries-on-a-chip that mimic the endothelium-blood interaction within the arterial lumen [142] and simulate physiologic blood flows [143] have been developed as well. An artery-on-a-chip that could simply measure VSMC function over pathophysiological time courses would provide an ideal platform for studying pathways and treatments for slower-developing vascular disorders.

Previously, we developed a method for measuring VSMC function called vascular muscular thin films **(MTFs)** that can be implemented into an artery-on-a-chip platform. The MTF is a two-layer biohybrid construct consisting of a monolayer of VSMCs patterned via microcontact printing **(µCP)** [144] of extracellular matrix **(ECM)** onto a PDMS substrate [15, 145]. Stress in the cell layer due to muscle contraction, the key measure of vascular muscle function, causes the construct to bend. This stress can then be calculated using the radius of curvature and known mechanical properties of the MTF layers. MTF technology has proven useful in studying acute mechanical and biochemical dynamics of arteries [145], as well as cardiomyocytes [15] and valve endothelial cells [146]. However, we observed that vascular tissue integrity decreased rapidly starting four days after seeding on these constructs. This decrease in cellular attachment is likely due to the combination of hydrophobic recovery of PDMS [147] and enzymatic degradation of ECM [148] that results in delamination of tissues. Thus, for MTFs to be a robust method for studying vascular pathogenesis, a new method for constructing tissues with extended viability is necessary.

Most cells, including VSMCs, will not adhere to unmodified PDMS. Several surface modification techniques have been proposed to effectively 'mask' biological materials from the hydrophobicity of PDMS [149-152]. However, following these treatments, cells are rarely viable past one week. Recently, surface modification of PDMS with genipin, a commonly used crosslinking protein, has shown promise in prolonging viable culture of myoblasts [153]. Genipin features low toxicity compared to other common biological crosslinking agents and high versatility as a biomaterial with numerous applications in tissue repair [154-156] and ECM modification [157-159].

Here, we present a method for measuring vascular smooth muscle contractility over physiologically-relevant time scales. We modified our previous MTF method by micropatterning the PDMS layer with genipin to allow longer culture times, while maintaining tissue structure. We also assessed temporal

20

changes in tissue structure and contractile function of vascular tissues constructed on genipin-modified PDMS surfaces and compared to those fabricated using µCP. We found that tissues show improved viability on genipin-modified surfaces and maintain consistent basal tone with decreased responsiveness to endothelin-1-induced contraction over the course of 14 days. This method provides the framework for future investigations of pathological VSMC function in slow-developing vascular diseases.

3.3 Materials and Methods

3.3.1 Tissue Fabrication and Characterization

All tissues were fabricated on Sylgard 184 (Dow Corning) PDMS substrates. PDMS was spin coated on a 25-mm diameter glass cover slip and cured at 65 °C for 4 h. Two methods, microcontact printing **(µCP)** and microfluidic delivery were used to pattern micro-scale guidance cues for tissue organization onto PDMS substrates.

3.3.1.1 Microcontact Printing

Stamps with microscale features were fabricated using traditional photolithographic techniques. Briefly, photomask films were designed with alternating lines of 10-µm width with 10-µm pitch between (Fig. 3.1 A, top). The photomasks were used to selectively expose SU-8 photoresist (MicroChem) spin coated onto silicon wafers with a feature height of 5 µm. Stamps were fabricated by pouring PDMS onto respective patterned silicon wafers. After degassing, PDMS was cured at 65 °C for 4 h. Stamps were then cut into appropriate shapes for use in tissue fabrication. µCP was used to pattern fibronectin **(FN)** onto PDMS substrates. FN (BD Biosciences) at 50 µg/ml concentration was incubated on patterned PDMS stamps for 1 h at room temperature (Fig. 3.1 A). FN was

transferred to PDMS-coated cover slips after UVO surface treatment, yielding high-fidelity lines of FN on the PDMS substrates (Fig. 3.1 A). Samples were rinsed in 1X PBS (Corning) prior to seeding.

3.3.1.2 Microfluidic Protein Delivery

Microfluidic devices were fabricated using the same methods as μCP stamps, but using a modified photomask film with branching channels and SU-8 photoresist with 20-μm feature height. Starting as a single channel, the pattern branched in a binary fashion until channels of 10-μm width were separated by walls of 10-μm width, yielding the same pattern as μCP stamps (Fig. 3.1 A, bottom). Inlet and outlet vertical channels were made using a 1-mm biopsy punch. After UVO surface treatment, devices were sealed onto PDMS-coated cover slips via conformal contact. Devices were primed with 70% ethanol, then rinsed with 1X PBS. Microfluidic protein delivery was used to deposit either FN only or to serially deposit genipin and FN (Gen+FN). To deliver FN only, 100 μl of 50 μg/ml FN was placed at the inlet and drawn through via negative pressure. FN was incubated at 37 °C for 24 h. To deliver Gen+FN, genipin (Cayman Chemical) was resuspended in sterile ddH$_2$O at a concentration of 1 mg/ml. 50 μl of genipin solution was placed at the inlet and drawn through the device slowly using a house vacuum (Fig. 3.1 A, bottom). Drops of 1X PBS were placed at both inlet and outlet to maintain wetting while genipin was incubated at 37 °C for 4 h. After incubation, 1X PBS was drawn through the device to remove excess genipin. Next, 100 μl of 50 μg/ml FN was placed at the inlet and drawn through the device slowly via negative pressure. FN was incubated at 37 °C for 24 h. After FN incubation, devices were carefully peeled away, and cover slips were rinsed in 1X PBS prior to seeding.

3.3.1.3 Vascular Smooth Muscle Cell Culture and Seeding

Human umbilical artery vascular smooth muscle cells (VSMCs) were purchased at passage 3 from Lonza and cultured in growth medium containing M199 medium with 10% FBS, 50 U/ml penicillin, 50 U/ml streptomycin, 10 mM HEPES, 1X MEM Non-Essential Amino Acids, 2 mM L-glutamine, 3.5 g/L glucose, and 2 mg/L Vitamin B_{12} supplement. Passages 5-7 were used for seeding constructs coated in FN (Fig. 3.1 B). µCP substrates were seeded at 65,000 VSMCs/cm^2. All microfluidic patterned substrates were seeded at 80,000 VSMCs/cm^2 to ensure confluent tissues. Higher cell seeding density accounted for edge effects of microfluidic device branching. After 24 h, samples were serum starved. All time point designations (e.g. Day 1, Day 2, etc.) are relative to time in serum-free growth medium.

3.3.1.4 Staining and Imaging of Tissue Structure

Samples were fixed in 4% paraformaldehyde after 1, 2, 4, 7, 10, or 14 days and stored in PBS at 4 °C for concurrent staining. Tissues were treated with Triton X-100 for permeabilization, then stained with mouse anti-paxillin primary antibody (BD Transduction Laboratories) labeled with Alexa Fluor 546 (Life Technologies) secondary antibodies. Nuclei and f-actin fibers were stained with DAPI (Life Technologies) and Alexa Fluor 488 phalloidin (Life Technologies), respectively. Mounted samples were imaged with an Olympus IX81ZDC microscope with Disk Spinning Unit confocal attachment (Olympus).

3.3.1.5 Analysis of Tissue Structure

Tissue confluence and alignment were analyzed via staining of f-actin filaments (phalloidin) and nuclei (DAPI). Percent confluence was determined by thresholding actin images and calculating the percent coverage in each of ten

random fields of view within a single tissue. Tissue alignment was analyzed using both f-actin and nuclei images. Orientation order parameters **(OOPs)** for actin images were calculated as previously published [84, 146, 160]. Orientations were recorded for ten random fields of view on each single tissue with an OOP calculated for the total tissue. Nuclear orientation was quantified by fitting an ellipse to each individual nucleus in DAPI images and calculating a vector along the major axis of the resulting ellipse [161]. The orientations of these vectors were analyzed similar to actin orientation to find a nuclear OOP for each single tissue. Nuclear eccentricity, ε, for each nucleus was calculated from the fitted ellipses using,

$$\varepsilon = \sqrt{1 - \left(\frac{minor\ axis\ length}{major\ axis\ length}\right)^2}.$$ (Eq. 3.1)

Tissue thickness was measured as in Alford et al. [84] using f-actin confocal images.

3.3.1.6 Focal Adhesion Analysis

Paxillin was imaged at 60x magnification to assess focal adhesion **(FA)** density and plaque area as in Xing et al. [162]. Briefly, autothresholding of images was completed using a rolling ball background subtraction plugin for ImageJ. A single round of dilation and erosion was then applied to ensure complete FA fidelity. A particle analysis function in ImageJ was then used to quantify FA properties. FAs were defined as continuous particles containing no fewer than 10 pixels (~0.11 μm^2 [163]) and no greater than 2000 pixels (~23 μm^2 [164]). FA area was calculated as the average plaque area in pixels converted to microns using known microscope objective parameters. FA density was determined using an ImageJ particle analysis algorithm to quantify plaque counts and normalizing counts to the calculated field of view area. FA area and density values from ten random locations were averaged for each tissue.

3.3.2 Vascular Muscular Thin Films

Vascular muscular thin film **(vMTF)** constructs were fabricated according to previous methods [160]. Briefly, a 5-mm strip of poly(N-isopropylacrylamide) (PIPAAm, Polysciences, Inc.) dissolved in 1-butanol was spin coated across the center of the cover slip (Fig. 3.1 B). PDMS doped with 1.0 μm fluorescent microspheres (Polysciences, Inc.) at a concentration of <0.01% by volume was spin coated on top of the PIPAAm and then cured at 65 °C for 4 h.

3.3.2.1 MTF Contractility Assay

Tissue function was assessed using a MTF contractility assay. At the time of the experiment, a series of cuts were made as in Grosberg et al. [160], yielding eight parallel MTFs. Samples were cooled below 32 °C to dissolve the PIPAAm strip and release the MTFs (Fig. 3.1 C). The sample was then transferred to a dish containing Tyrode's solution (1.192 g HEPES, 0.901 g glucose, 0.265 g $CaCl_2$, 0.203 g $MgCl_2$, 0.403 g KCl, 7.889 g NaCl, and 0.040 g NaH_2PO_4 per liter of ddH_2O) maintained at 37 °C using a LCS-1 Thermal Cooling Module and Quick Exchange Heated/Cooled Platform (Warner Instruments). MTFs damaged during cutting were removed prior to the start of the contractility assay.

A Lumar V12 stereomicroscope (Carl Zeiss) was used to capture transmitted and fluorescent light images of MTFs every 30 s for 60 min. Tissues were allowed to equilibrate. They were then serially stimulated, first with 50 nM endothelin-1 to induce contraction [84], then with 100 μM HA-1077 (Sigma-Aldrich), a rho kinase inhibitor, to induce relaxation.

3.3.2.2 Analysis of Tissue Stress

Tissue stress in MTFs during the contractility assay was analyzed using custom MATLAB code built upon previously reported methods [15, 160]. Projection

lengths were used to determine radius of curvature in each MTF as in Grosberg et al. [160]. The mean cross-sectional stress was calculated from the observed radius of curvature and measured thickness and stiffness of the tissue and PDMS layers as previously published [15] (Fig. 3.1 C). Every fourth substrate sample was retained for PDMS thickness evaluation via a Tencor P-10 stylus profilometer (KLA-Tencor). Relationships between spin coating time and thickness were determined for every set of MTF cover slips.

Two stress states were used for comparison of VSMC contractile function. Basal tone was calculated by subtracting initial stress in the tissue at equilibrium from the stress in the tissue after HA-1077 inhibition of contraction. Induced contraction was calculated as the increase in stress due to application of endothelin-1. Mean values of both stress states were calculated for both μCP and Gen+FN fabrication techniques at Days 1, 2, 4, and 7. Tissues on Gen+FN were also tested on Days 10 and 14. μCP tissues were only maintained through Day 7 due to loss of tissue integrity.

3.3.2.3 Assessment of Tissue Metabolic Activity

Gen+FN tissue metabolic activity was assessed using an XTT (2,3-bis[2-Methoxy-4-nitro-5-sulfophenyl]-2H-tetrazolium-5-carboxyanilide inner salt) toxicology assay (Sigma-Aldrich) [165]. Briefly, Gen+FN tissues at Days 1, 2, 4, 7, 10 and 14 were treated with 500 μL of 0.2 mg/ml XTT in Tyrode's solution and incubated for 4 h at 37°C. Solutions were resuspended and two 250 μL samples were transferred to a 96-well plate for absorbance readings. Absorbance at 450 nm and 690 nm was recorded using a plate reader (Bio-Tek). Absorbance values with background and blank values subtracted were normalized to Day 1 values.

3.3.2.4 Assessment of Cell Viability

Gen+FN cell viability was measured using a calcein AM live/dead assay (Life Technologies) [166]. Gen+FN tissues were incubated in 2 µM calcein AM and 4 µM ethidium homodimer-1 (Life Technologies) for 45 min, followed by a 10 min Hoechst staining for nuclei. Live samples were imaged at 20x with an Olympus IX81ZDC microscope with Disk Spinning Unit confocal attachment. Nuclei were counted by fitting an ellipse to each individual nucleus in Hoechst images. Dead cells were manually counted in ethidium homodimer-1 images and subtracted from nuclei counts to yield number of live cells. Live cell values were normalized to Day 1 values. A linear best fit of the ratio of normalized XTT metabolic activity to normalized live cell counts at each time point was also calculated.

3.3.3 Statistical Analysis

Statistical comparisons for actin confluence and actin and nuclear alignment involved a natural logarithmic transformation of mean values for each condition (day and fabrication method) to account for unequal variance, followed by ANOVA with a Tukey pairwise multiple comparisons test. Contractility results were compared using ANOVA to determine if any significant differences occurred between fabrication techniques.

3.4 Results

3.4.1 Tissue Fabrication and Confluence Analysis

We aimed to develop a tissue microfabrication method that yields the high fidelity tissue structure of µCP, but with extended tissue viability necessary to study chronic vascular disease. To do this, we developed a microfluidic ECM deposition device for patterning genipin on PDMS substrates (see 3.3.1.2 for details). To

27

compare this method to more traditional methods, we considered three tissue construction methods: µCP, microfluidic delivery of FN only, and serial microfluidic delivery of genipin and FN (Gen+FN). In each case, the result of the micropatterning was 10-µm-wide lines of FN with a 10-µm pitch between (Fig. 3.1 A).

For each patterning protocol, when cells were seeded, they self-organized into aligned monolayers (Fig. 3.2). The tissues were then serum starved to induce an *in vivo*-like contractile phenotype [167] and incubated for 1-14 days in serum-free medium. Daily transmitted light images were captured to assess tissue integrity over time. Qualitatively, no differences were seen until Day 7, with noticeable decreases in tissue confluence and integrity starting at Day 7 in FN only and Day 10 in µCP (Fig. 3.2). Only sparse individual cells remained at Day 14 for both FN only and µCP samples. Gen+FN yielded confluent tissues throughout the course of two weeks that appear to maintain their integrity longer than tissues grown on PDMS without genipin modification. Tissue samples were fixed on Days 1, 2, 4, 7, 10, and 14 and stained for f-actin to quantitatively assess confluence. Cytoskeletal coverage was assessed via immunostaining for f-actin filaments. Images showed highly-confluent, anisotropic structure of f-actin filaments for both µCP and microfluidic delivery fabrication methods (Fig. 3.3 A). Using image thresholding (see 3.3.1.6 for details), we found that percent confluence of actin filaments showed consistent confluence through two weeks in tissues fabricated on Gen+FN substrates. Tissues fabricated on unmodified substrates displayed statistically significant decreases between Day 10 and Day 14, suggesting loss of tissue integrity and viability (Fig. 3.3 B).

3.4.2 Vascular Tissue Structure

Smooth muscle cells in arteries are aligned approximately circumferentially about the vessel in concentric lamellar sheets [5]. Thus, our *in vitro* model must

reproduce this highly-aligned tissue structure in addition to maintaining confluence. To assess tissue alignment, we characterized subcellular organization of tissues constructed with each of our three fabrication methods over a two-week incubation period. Alignment of f-actin filaments was quantitatively assessed using an orientational order parameter (OOP), where an OOP of 1.0 represents a perfectly aligned tissue and an OOP of 0.0 represents a perfectly isotropic tissue. OOP was >0.8 for all fabrication methods for Days 1-7 (Fig. 3.3 C). The µCP and FN only OOP decreased steadily after Day 7, consistent with the decrease in confluence (Fig. 3.3 B), further suggesting a loss of tissue integrity in conditions without genipin modification of PDMS. However, alignment was maintained through Day 14 for Gen+FN substrates, with OOP >0.74 throughout the time course.

To provide a more comprehensive analysis of subcellular tissue structure, we also considered nuclear alignment and shape. We expected nuclear alignment to mirror actin alignment based on prior work [84]. To determine if this persisted on Gen+FN substrates, OOP was also determined for nuclei across all three conditions. As expected, nuclear OOP results mirrored those of actin OOP (Fig. 3.3 D). In addition to nuclear alignment, nuclear eccentricity was also analyzed. We have previously found that nuclear eccentricity increased with increased VSMC contractility [84]. Here, no discernable trend existed in nuclear eccentricity across the fabrication techniques over time (Fig. 3.3 E), though nuclear eccentricity generally decreased over the culture time for each technique.

Focal adhesion (FA) maturation, which can be characterized by FA area and density, has been correlated with force generation in the cytoskeleton and are indicative of a contractile phenotype in VSMCs [168]. To determine whether VSMC maturation occurred with increasing culture time on Gen+FN samples, we immunostained for paxillin, an integral FA protein. Images of paxillin were used to quantitatively measure focal adhesions over time (Fig. 3.4 A, see Methods for details). A binary mask was used to quantify FA area and density (Fig. 3.4 B). Paxillin plaque area was found to be consistent over time, with a slight increase on

Day 7 (Fig. 3.4 C). FA density was also found to be consistent across all time points, with a slight decrease on Day 7 (Fig. 3.4 D). These results suggest maintenance of consistent tissue structure and maturity on Gen+FN substrates for the full two-week incubation.

3.4.3 MTF Analysis of Tissue Function

The importance of pathologic changes in VSMC function in vascular disease drove our interest in developing a method for assessing contractility over time scales longer than currently possible. We hypothesized that stress would remain consistent over time for viable tissues. To test this hypothesis, we employed vascular MTFs to directly measure VSMC function. Comparisons between traditional µCP and novel microfluidic patterning techniques were made to determine the viability of Gen+FN substrates for long-term vascular contractility assays with MTFs. MTFs consisted of a monolayer of VSMCs patterned on a thin layer of PDMS. As the tissue contracts, the passive PDMS layer bends (Fig. 3.5 A). The radius of curvature of the MTF is used to measure stress over time (Fig. 3.5 B). Tissues were serially stimulated with endothelin-1 (ET-1) to induce contraction and the rho-associated protein kinase inhibitor HA-1077 to induce relaxation. Gen+FN samples were evaluated on Days 1, 2, 4, 7, 10, and 14. Due to decreased tissue integrity at Day 10 on µCP substrates (Fig. 3.2), µCP tissue contractility was only assessed through Day 7.

Two tissue contractility measures were used to compare tissue fabrication techniques' effects on function: basal tone, which describes the contraction of the tissue with no external stimulation, and induced contractility, which is the additional stress due to ET-1 stimulation. Basal tone in µCP tissues started low at Day 1 (3.2±1.1 kPa) and steadily increased through Day 7, where the maximum basal tone was 4.1±0.8 kPa (Fig. 3.5 C). Gen+FN tissues demonstrated consistent basal tone throughout two weeks, with an average basal tone of 2.5±0.2 kPa over the

whole period (Fig. 3.5 C). Calculation of induced contraction yielded a nearly identical trend across the fabrication methods through Day 7. Both start high (~1 kPa) and decrease over time (Fig. 3.5 D). Tissue metabolic activity measured as change in absorbance due to reduction of the tetrazolium ring in XTT to formazan decreased over time, as did the number of live cells (Fig. 3.5 E). The ratio of these values remained relatively constant throughout the time course (Fig. 3.5 E, red dotted line). However, Gen+FN tissues showed the ability to contract on Day 14, suggesting a viable, fully-functional arterial tissue mimic for long-term experimentation.

3.5 Discussion

VSMC function is important for maintaining homeostasis in arteries. Maladaptive perturbation of VSMCs has also been implicated in a wide variety of vascular diseases, including hypertension [70], vasospasm [132], and aneurysm [135]. The central role of VSMC function in arterial growth and remodeling has led to development of mathematical [73, 169-174]and experimental [61, 78, 120, 145, 175] models of vascular disease states. Previous methods for isolating VSMC-driven disease mechanisms fail either to provide a simple readout of function or to recapitulate VSMC function over relevant time scales. Thus, long-term models must be developed to comprehensively investigate the mechanisms of vascular disease.

Here, we adapted our MTF assay for long-term studies by patterning the passive PDMS layer with genipin. Genipin adsorption yields a modified PDMS substrate, presenting hydrophilic residues for protein deposition and maintenance of focal adhesions. As cells remodel the ECM, the crosslinking property of genipin supports sustained adhesion of VSCMs to PDMS substrates. In substrates without genipin surface modification, ECM remodeling causes steady deterioration of adhesion and results in observed release and death of VSMCs. We found that

MTFs constructed on genipin-modified substrates remained viable for up to one week longer than those patterned using µCP or FN adsorption. This result suggests that genipin modification of PDMS is a viable method for long-term culture of VSMCs that can be implemented in the study and modeling of various vascular disease mechanisms and the associated mechanics of vascular tissues.

We found generally good correlation between Gen+FN MTFs and µCP MTFs in the early stages of tissue development. The one outlier we found was Day 7 basal tone (Fig. 3.5 C). We believe, however, that the elevated tone in the µCP tissues is an artifact of our method, which cannot account for tissue disconnecting from the substrate. Our stress measurement method assumes that the tissue layer of the MTF is fully connected to the PDMS layer. However, we have observed that in MTFs where cellular connection to the PDMS substrate is compromised, the tissue often locally separates, forming tissue bridges that can cause increased MTF curvature, and thus, increased perceived stress. Though we did not directly observe any bridges in the results presented here, we believe the elevated stress measured is due to microbridge formation and not to increased contractility in these samples.

Our results suggest decreased performance of MTFs at late stages of the assay, primarily between Day 10 and Day 14. We found both decreased induced contractility (Fig. 3.5 D) and decreased metabolic activity (Fig. 3.5 E) over time. This brings into question the viability of the presented assay at later time points. However, we also show a decrease in viable cells at later time points. This is expected as a result of culturing tissues in serum-free medium for extended time courses, mimicking the *in situ* conditions surrounding VSMCs in healthy arteries. VSMCs cultured in serum-free medium have been reported to have improved contractile properties and shift toward a contractile phenotype [167]. Contractile VSMCs rarely proliferate. Thus, over time, dead cells are not replaced in tissues cultured in serum-free conditions. The decreases in induced contractility and metabolic activity can be correlated to decreases in viable VSMCs in our tissues,

suggesting VSMC performance and function are not affected by genipin surface modification. To avoid this viable VSMC loss, futher studies may be performed with a small basal level of serum to allow greater cell proliferation and, thus, live VSMC population maintanence.

Long-term models of VSMC function are important because VSMCs play a critical role in both adaptive and maladaptive arterial growth and remodeling that can occur over on the scale of weeks, months, or even years. Pathogenesis of cerebral vasospasm has been shown to occur over 3-7 days post-injury with characteristic hypercontractility followed by responsive arterial remodeling [18, 132]. Hypertension studies have suggested that smooth muscle growth and collagen remodeling are critical factors in long-term structural changes to arteries [176, 177]. Rapid changes in artery residual stress (2-10 days) in hypertension models suggest non-uniform remodeling within arterial walls due to non-uniform stress distribution caused by increased pressure [6, 71]. Fridez et al. found that the early stages of hypertensive remodeling are primarily due to VSMC adaptation and hypercontractility with ECM remodeling playing a role later in the process, returning arterial basal tone to normal levels [178]. Jackson et al. showed VSMC proliferation and ECM remodeling occur in the vessel wall when longitudinal tension is applied, returning the artery to a normal strain state over time [121]. Computational models also suggest that there is a direct correlation between mechanical forces applied to VSMCs and these long-term remodeling phenomena [73, 171, 179-181]. However, the mechanotransduction pathways involved are not well established. Our extended MTF assay could provide a robust assay for studying these early stages of mechano-adaptation in chronic vascular diseases with the experimental control to isolate cell-signaling pathways. Extending the previous MTF method from 2-3 days to up to 14 days allows for broadened applicability and provides a more comprehensive method for studying disease pathways involving maladaptive remodeling.

While our current studies focus on cellular function, our results suggest MTFs could also be used to study the evolving interaction of cells with their ECM environment. We found that FA structural variation in Gen+FN samples (Fig. 3.4 C,D) corresponded temporally with both loss of tissue integrity (Fig. 3.2) and elevated apparent contractility in μCP samples (Fig. 3.5 C). We found a decrease in alignment of both actin (Fig. 3.3 C) and nuclei (Fig. 3.3 D) from Day 7 to 10 in all samples. In the μCP and FN only samples, this loss of alignment precedes delamination, but in Gen+FN samples, the alignment recovers by Day 14. At these time points, FA size decreased (Fig. 3.4 C) and density increased (Fig. 3.4 D), consistent with nascent FA formation [168, 182, 183]. This result suggests that the initially patterned FN is being replaced by cell-generated ECM in the Gen+FN samples. This aspect of our long-term MTF assay could be employed to study the dynamics of cell stress generation during ECM remodeling processes.

3.6 Conclusions

Here, we report a method for studying smooth muscle contractility *in vitro* over physiologically-relevant time scales by modifying our previous MTF assay. We functionalized PDMS substrates with genipin to sustain long-term culture of VSMCs. We validated our method by comparing the structure and function of tissues fabricated on substrates with genipin modification with traditional MTF construction methods. Genipin-modified MTFs yielded tissues with high alignment, sufficiently mimicking the circumferential alignment of VSMCs in arteries. In addition, these tissues showed sustained tissue contractility and integrity throughout two weeks, greatly improving upon previous fabrication techniques. Our assay allows for studies of pathological function and arterial growth and remodeling and can be integrated into an artery-on-a-chip system (see Appendix A) for pharmacological screening of treatment strategies for vascular disease.
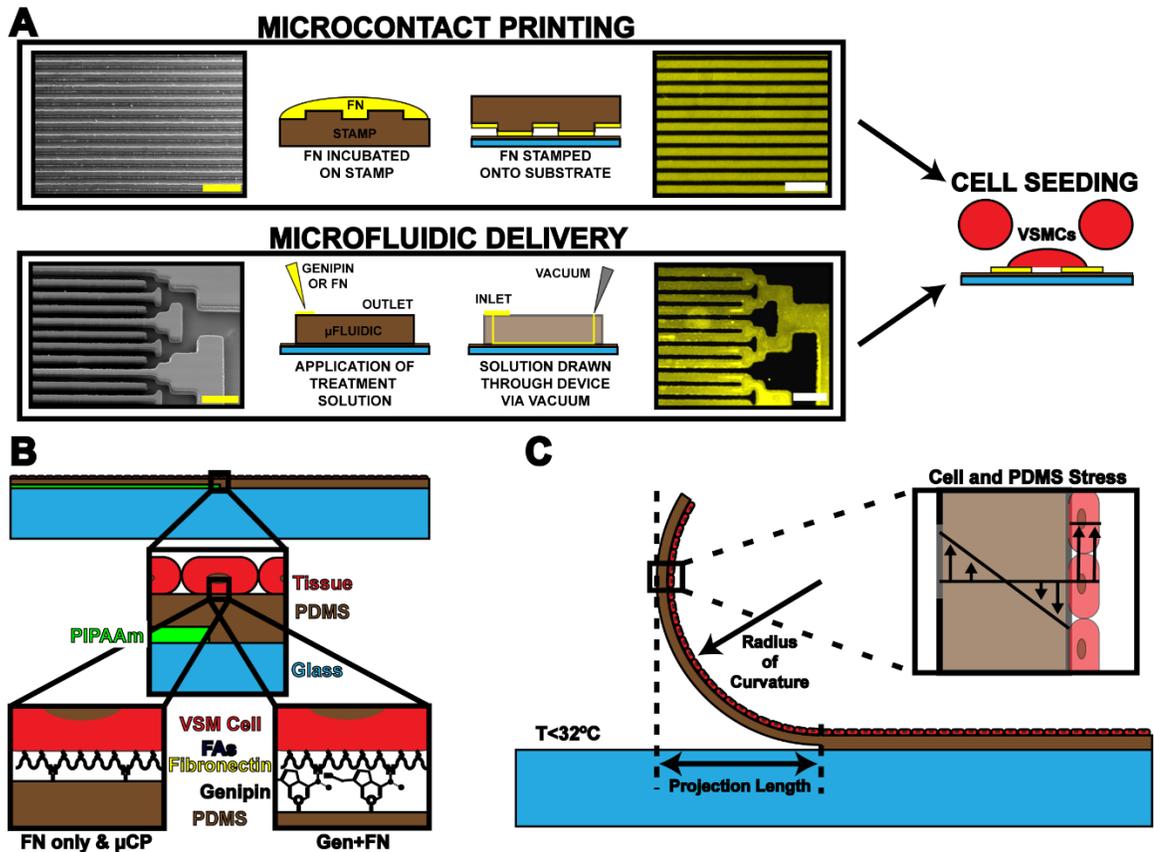
Figure 3.1. Extracellular matrix patterning and muscular thin film methods. (A) Microcontact printing (µCP) and microfluidic (µFluidic) delivery procedures. Left: Scanning electron microscopy images of PDMS stamps (µCP) and µFluidic devices (scale bar: 50 µm). Center: µCP and µFluidic device methods for ECM deposition. Right: Immunostained FN (scale bar: 50 µm). Far right: Cell seeding of FN-patterned substrates. (B) Tissue construct structure for MTF experiments. (Green: PIPAAm, brown: PDMS, Blue: glass cover slip, Red: cells, Purple: focal adhesions, Yellow: fibronectin, Black: genipin). Left bottom inset: Non-genipin-modified substrates. Right bottom inset: Genipin-modified substrates. (C) Schematic representation of MTF release. Inset: Representative transmural stress in the PDMS and cell layers.
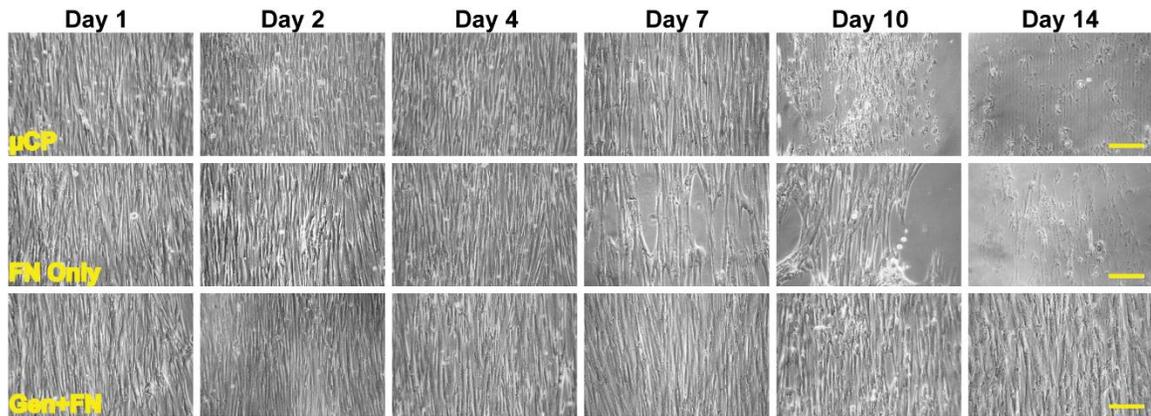
Figure 3.2. Tissues constructed on genipin-modified substrates maintain viability longer than traditional methods.

Representative transmitted light images of tissues constructed using three fabrication techniques: 1) traditional µCP of fibronectin (µCP) 2) fibronectin delivered via microfluidic device (FN only) 3) genipin and fibronectin delivered via microfluidic device (Gen+FN). Time represents days after serum-starvation of tissues. (Scale bars: 200 µm).
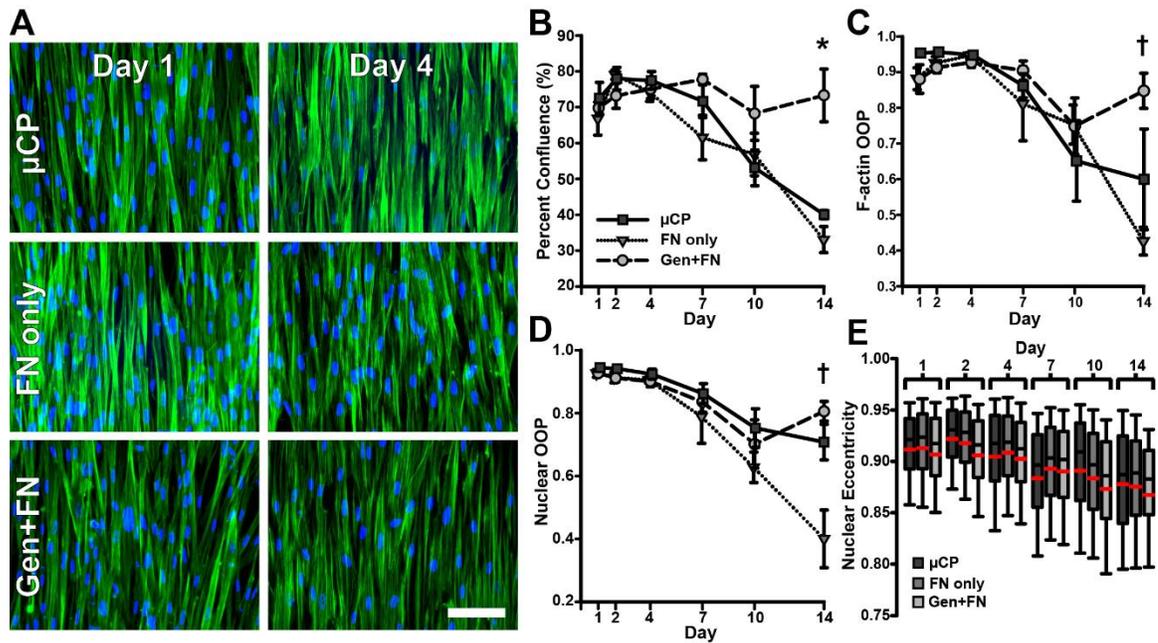
Figure 3.3. Tissues constructed on genipin-modified substrates maintain confluence and subcellular organization longer than those constructed using traditional methods.

(A) Immunofluorescent images of tissues (green: f-actin, blue: nuclei, μCP: microcontact printing of fibronectin, FN only: microfluidic delivery of fibronectin only, Gen+FN: microfluidic delivery of genipin followed by fibronectin, Scale bar: 100 μm). (B) Percent tissue confluence as measured by actin coverage. (*: significantly different from FN only and μCP, $p < 0.05$, error bars: standard error, μCP: n=3-6, FN only: n=4-8, Gen+FN: n=3-7). (C) Orientation order parameter (OOP) of f-actin filaments (†: significantly different from FN only, $p < 0.05$, Error bars: standard error, μCP: n=3-6, FN only: n=4-8, Gen+FN: n=3-7). (D) OOP for nuclei (†: significantly different from FN only, $p < 0.05$, Error bars: standard error, μCP: n=3-6, FN only: n=4-8, Gen+FN: n=2-7). (E) Nuclear eccentricities (box: 25%-75%, bars: 10%-90%, Black thin line: median, Red thick line: mean, μCP: n=3-6, FN only: n=4-8, Gen+FN: n=2-7).
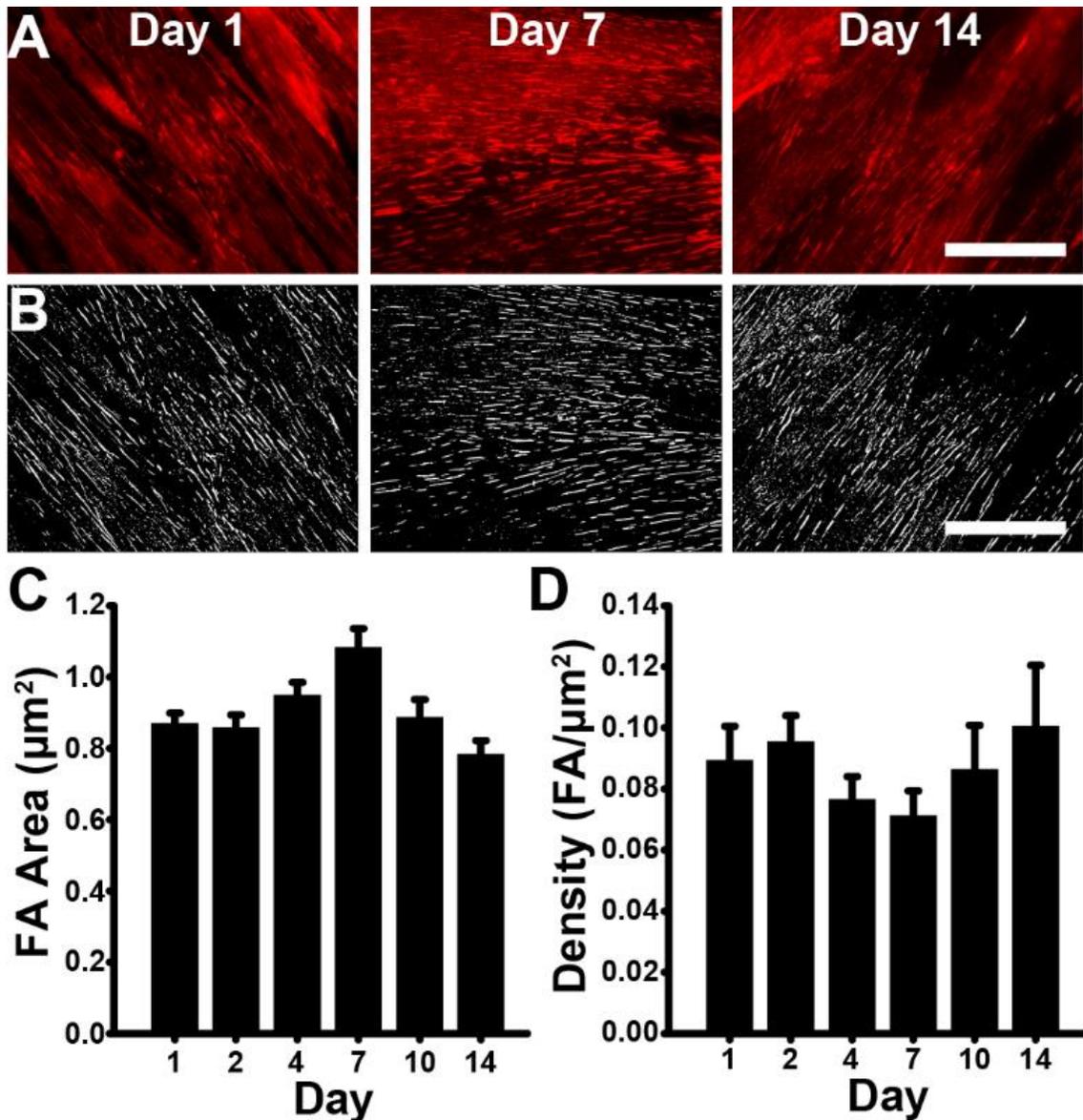
Figure 3.4. Focal adhesion size and density are consistent with time in Gen+FN tissues.
(A) Representative immunofluorescent images of tissues immunostained for the focal adhesion protein paxillin (red, Scale bar: 50 µm). (B) Representative binary masks of confocal images for determining FA area and density (White: FA, Scale bar: 50 µm) (C) FA area. (D) FA density. All graphs: mean ± standard error, n=3-4.
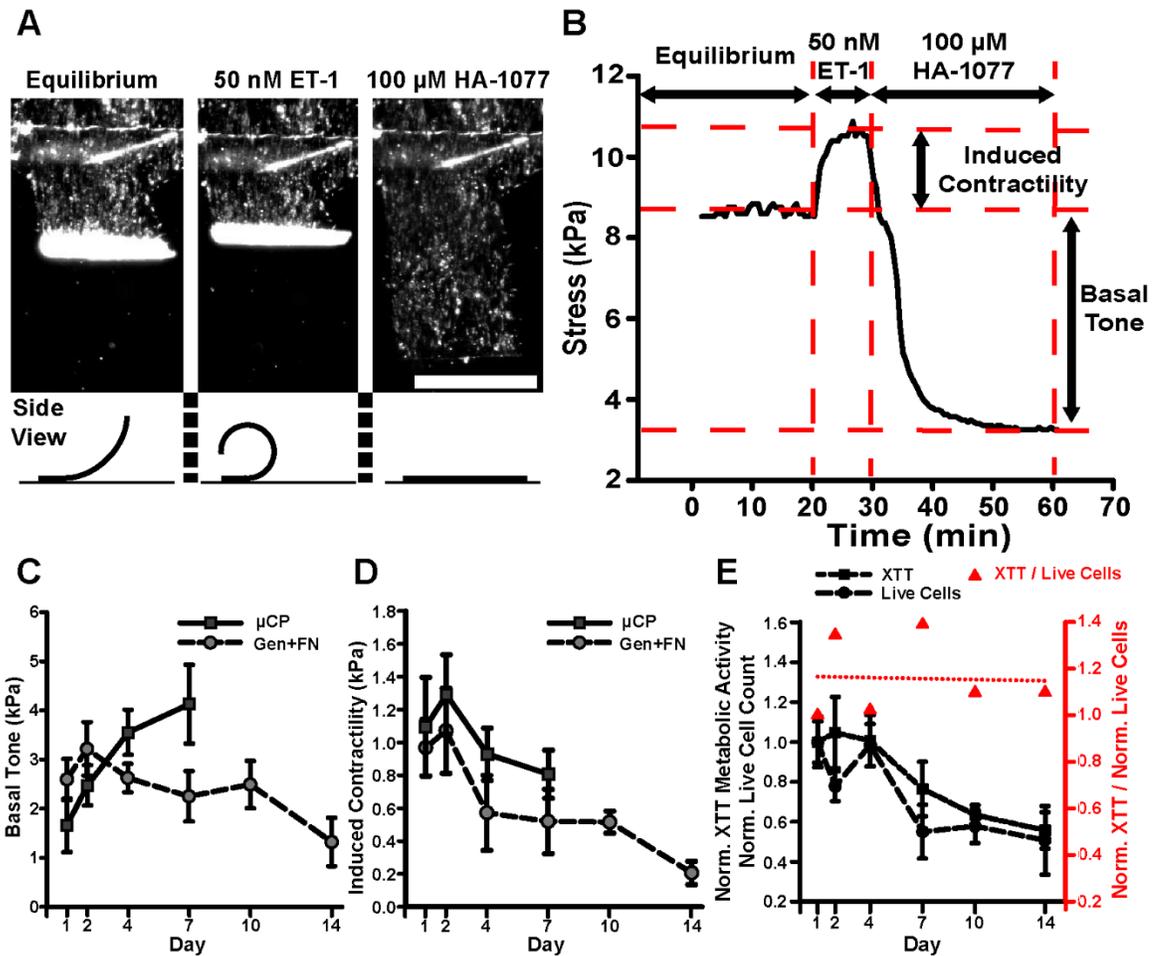
Figure 3.5. VSMC contractility is maintained throughout the course of two weeks and comparable to our traditional MTF technique.
(A) Top: Representative transmitted light images of MTFs at critical points of contractility assay (scale bar: 1 mm). Bottom: Side view schematics of relative MTF curvature. (B) Characteristic stress curve for quantitative analysis of contractility. Induced contraction by ET-1 and basal tone are normalized to the initial equilibrium stress in the tissue. (C) Basal tone (error bars: standard error, µCP, squares: n=8-18, G+FN, circles: n=5-12). (D) Induced contractility (error bars: standard error, µCP, squares: n=8-18, G+FN, circles: n=5-12). (E) XTT metabolic activity (squares, short dashed line) and live VSMC cell count (circles, long dashed line) normalized to Day 1 values. Red linear best fit (dotted line) of the ratio of normalized XTT activity to live VSMC cell count over 14 days (error bars: normalized standard error, XTT metabolic activity: n=4-9, Live VSMC count: n=2-4).

Chapter 4. Subarachnoid Hemorrhage-Associated Factors Influence on Vascular Smooth Muscle Contractility

This chapter contains material adapted from an invited original research article at *JBME* and is reproduced with permission. **Hald ES**, Timm CD, and Alford PW. In Press. Amyloid Beta Influences Vascular Smooth Muscle Contractility and Mechano-Adaptation. It is also based on previously submitted research abstracts for the *2015 and 2016 Summer Biomechanics, Bioengineering, and Biotransport Conferences*.

4.1 Summary

Subarachnoid hemorrhage can lead to abnormal and elevated exposure of the cerebral vasculature to a variety of blood and clotting factors. It is also a common precursor to the development of cerebral vasospasm, a mechanically-defined vascular disease that can lead to severe ischemia and even death of patients. The direct effects of the factors released during hemorrhage on vascular functional contractility are largely unknown. Here, we measured the individual effects of treatment with three common factors released and/or elevated during hemorrhage: transforming growth factor-beta **(TGF-β1)**, platelet-derived growth factor **(PDGF)**, and thrombin. We found that TGF-β1 and PDGF treatment yields minimal effect on VSMC functional contractility. Thrombin treatment results in decreased VSMC basal tone after 24h. We also assessed the functional phenotypic consequences of all three factors, finding factor-dependent shifts in VSMC synthetic and contractile phenotypes. These findings suggest further study is needed to fully elucidate the importance of specific SAH-related factors in the progression of cerebral vasospasm.

4.2 Introduction

Subarachnoid hemorrhage **(SAH)** is bleeding in the subarachnoid space of the brain, often a result of traumatic brain injury or intracranial aneurysm [132]. When SAH occurs, growth and clotting factors, such as TGF-β, PDGF, and thrombin, are released (see Fig. 2.1) [18]. Surrounding tissues exposed to elevated levels of these factors in the blood, cerebrospinal fluid, and brain interstitial fluid [184-186] can undergo a variety of mechanical and biochemical perturbations affecting both vascular and neural function. Cerebral vasospasm **(CVS)** is a potentially lethal vascular disease that often occurs after SAH and is characterized by acute hypercontractile arterial behavior followed by extended remodeling, lumen occlusion, and ischemia over the course of 3-7 days after a bleed occurs [132]. It is unclear what initiates this characteristic functional behavior in CVS progression, resulting in limited therapeutic options to reduce negative patient outcomes associated with CVS.

Vascular smooth muscle cells **(VSMCs)** typically exist in a distribution between two functional phenotypes: contractile or synthetic (proliferative) [74]. During CVS, the distribution of VSMC phenotypes is thought to relate to tissue-level mechanics in the cerebral vasculature [187]. A growth and remodeling response to the acute hypercontractility is an observed hallmark of the disease. This growth and remodeling typically begins a few days after hemorrhage, resulting in a significant shift of VSMC population toward a proliferative synthetic phenotype [61]. Hypertrophy and proliferation of VSMCs results in thickening of cerebral arterial walls, which, in turn, can further exacerbate the effects of CVS, leading to severe ischemia due to luminal narrowing [30]. Factors released after hemorrhage have been implicated in VSMC phenotypic switching (see Fig. 2.2) and could contribute to progression of CVS. However, these effects have not been studied at the single VSMC scale.

Here, we utilize a traction force microscopy method to determine changes in VSMC mechanics resulting from differential treatment with SAH factors. We find

41

minimal differences in single VSMC mechanical output when treated with TGF-β1 and PDGF. Decreased VSMC function occurs acutely with thrombin treatment, but also leads to VSMC death or detachment over time. We also consider a distribution of VSMCs between synthetic and contractile functional phenotypes, how treatment with individual SAH-borne factors affects shifts in these distributions, and to what extent these factors may be critical in the pathologic mechanical progression of CVS.

4.3 Methods

4.3.1 Polyacrylamide Gel Fabrication and VSMC Culture

Polyacrylamide (PA) gels were fabricated as described by Tse and Engler [188] and tuned to a Young's modulus of 13.5 kPa. Gels were doped with 2% v/v 200-nm diameter red fluorescent microspheres to allow substrate displacement tracking. A 6.5-µL drop of PA gel solution was placed on 3% bind silane-functionalized cover slips. A clean 12-mm glass cover slip was placed on top of the gel drop to yield a uniform PA gel of thickness ~50 µm upon gel curing (Fig. 4.1). Cured PA gels were coated with 0.2 mg/ml sulfosuccinimidyl-6-(4'-azido-2'-nitrophenylamino)-hexanoate (Sulfo-SANPAH, Thermo Scientific, Rockford, IL) to covalently bond 50 ug/ml human fibronectin (Corning, Bedford, MA) to PA gel surfaces (Fig. 4.1) [189]. PDMS rings (18-mm diameter) were attached to reduce cell seeding area and required medium volume.

Human umbilical cord artery VSMCs (Lonza, Walkersvile, MD) were cultured in growth medium composed of M199 medium with 10% FBS, 10 mM HEPES, 1X Non-Essential Amino Acids, 3.5 g/L glucose, 2mM L-glutamine, 1% penicillin/streptomycin, and 2 mg/L Vitamin B_{12} supplement. For all cell structure and function assays, passages 5-7 were used to sparsely seed polyacrylamide constructs (~5000 cells per construct) (Fig. 4.1).

4.3.2 SAH-factor Treatment Assays

After attachment, each sample containing sparsely-seeded VSMCs on PA gels were serum-starved for 24h to induce a contractile functional phenotype characteristic of normal arterial wall conditions [167]. Stock solutions of transforming growth factor-1 (TGF-β1, 10 ug/mL in 4 mM HCl with 1% bovine serum albumin, R&D Systems), platelet-derived growth factor (PDGF, 10 ug/mL in 4 mM HCl, R&D Systems), and thrombin (100 units/mL in 0.1% bovine serum albumin, Sigma-Aldrich) were prepared. Experimental solutions were made by dilution of stock solutions in serum-free growth medium. After 24h in serum-free medium, VSMCs were then treated with prescribed treatment solutions at one of five physiologic or pathologic concentrations (including control). For multi-day assays, treatment solutions were refreshed every 24h.

4.3.3 VSMC Functional Measurement

Mechanical function of VSMCs was measured by calculating the total strain energy of the substrate due to cell traction. This total strain energy, U, was calculated for two stress states: (1) basal tone via tissue relaxation with HA-1077, a rho-kinase inhibitor, and (2) ET-1-induced contraction (Fig. 4.2 A). Basal tone strain energy was calculated using the bead displacement field resulting from the difference between images captured at equilibrium and 30 min post HA-1077 treatment (Fig. 4.2 B, right). Similarly, ET-1-induced contraction strain energy was calculated using the bead displacement field resulting from the difference between images captured 10 min post ET-1 treatment and at equilibrium (Fig. 4.2 B, left). Experiments were conducted for sparsely-seeded single VSMCs attached to 13.5 kPa PA gels. Control and treatment samples were run concurrently. Cells were maintained in a physiologic Tyrode's solution (7.889 g NaCl, 1.192 g HEPES, 0.901 g glucose, 0.403 g KCl, 0.265 g $CaCl_2$, 0.203 g $MgCl_2$, and 0.040 g NaH_2PO_4

per liter of ddH$_2$O). Physiological temperature was maintained within a heating chamber attached to an Olympus IX81ZDC microscope. Brightfield images of single VSMCs and z-stacks of their underlying bead-doped substrates were captured at four time points: equilibrium, 10 min post 50nM endothelin-1 treatment, 30 minutes post 100mM HA-1077 treatment, and post cell lysis with 5% sodium dodecyl sulfate.

Traction force microscopy techniques were used to determine a single quantitative measurement of single VSMC mechanical output [190]. Template matching between fluorescent bead images from two different time points was completed using an ImageJ template matching algorithm [190]. Particle image velocimetry using iterative interrogation windows of 128-64-32 pixel width was completed between the matched bead images from the same cell location at different time points [190]. Noise filtering of the resulting displacement field was conducted by manually sampling an area outside of the cell tractions (field area) and subtracting the mean displacement ("field displacement") from all displacements. Displacements with value less than the mean of the modified displacements within the field area plus five standard deviations were considered noise and removed prior to further analysis. The noise-filtered displacement field was used to calculate traction stresses with a Fourier transform traction cytometry (FTTC) ImageJ plugin [190]. A Poisson's ratio of 0.48, a Young's modulus of 13.5 kPa, and a regularization factor of 1e-9 were used for all FTTC calculations. Total strain energy of the substrate, U, was calculated for each individual VSMC using

$$U = \frac{1}{2} \int \boldsymbol{T} \cdot \boldsymbol{u} \, dxdy \qquad \text{(Eq. 4.1)}$$

where $\boldsymbol{T}$ is the traction stress and $\boldsymbol{u}$ is the displacement.

Total strain energies were normalized to Day 1 control. Outlier analysis was conducted to remove all values above or below means by more than 1.5 times the interquartile range. Statistical comparisons for all experimental results were determined using Kruskal-Willis One Way ANOVA on Ranks and a Dunn's Method for pairwise multiple comparisons and a significance level of p<0.05.

4.3.4 VSMC Functional Phenotype Population Assessment

VSMC functional phenotype was quantitatively assessed using total strain energy for each cell normalized by Day 1 control means for each set of experiments. A threshold of 1.0 (i.e. Day 1 control mean) was used to determine percentage of cells above functional phenotype threshold (contractile) and below functional phenotype threshold (synthetic) for all experimental groups. Differences between treatment conditions and same day controls were calculated as percent difference in fraction of contractile cells.

4.4 Results

4.4.1 TGF-β1 and PDGF Do Not Influence VSMC Functional Contractility

We sought to determine the functional effects of exposure to a variety of single SAH-borne factors on VSMCs. We applied natural human TGF-β1 and PDGF to VSMCs seeded on polyacrylamide (PA) gels (Fig. 4.1). We used traction force microscopy to quantify total strain energy in the gels due to VSMC traction forces (Fig. 4.2). Chronic treatment with TGF-β1 largely yielded no changes in VSMC functional contractility, with the exception of an acute decrease in induced contraction observed for 100 pM treatment on Day 1 (Fig. 4.3). Similarly, PDGF chronic treatment also yielded minimal effects on VSMC contractility (Fig. 4.4). Taken together, these data suggest that TGF-β1 and PDGF do not significantly affect VSMC function.

4.4.2 Thrombin Reduces VSMC Functional Contractility and Viability

Thrombin is a considered to be a significant vasoconstrictor in the complex milieu of blood-borne biochemical factors [48]. Acute increases in contraction caused by thrombin exposure could result in a cascade leading to downstream proliferation in the growth and remodeling response to heightened vessel wall

45

stress. We sought to recapitulate this temporal cascade in single VSMCs treated with thrombin. Interestingly, we found significant decreases in acute basal function (Fig. 4.5). This effect was maintained through 48h of treatment for the highest concentration of thrombin treatment. Further, we observed drastic detachment and apoptosis of VSMCs treated with any concentration of thrombin for four days. These results suggest our assay is ill-equipped to capture thrombin effects on VSMC function.

4.4.3 Evaluation of Functional Phenotypic Populations

Given the apparent inability of our traction force microscopy assay to capture changes in VSMC function as a function of total strain energy, we took a closer look at the distribution of single VSMC total strain energy values. In many cases, cell populations appeared to be bimodal in nature. This led us to consider VSMC functional phenotype as an alternative metric for analysis. In doing so, we found that TGF-β1 treatment initially resulted in fewer contractile cells, as measured in basal tone and induced contraction stress states and represented as negative percent differences (Fig. 4.6, Row 1). The percentage of contractile cells increased for both states by Day 4 (Fig. 4.6, Row 1). PDGF treatment resulted in increased contractile functional phenotype for basal tone, but decreased contractile phenotype for induced contraction across all time points (Fig. 4.6, Row 2). Thrombin yielded dose-dependent responses in functional phenotypes related to induced contraction (Fig 4.6, Row 3). These results suggest a more comprehensive study of VSMC phenotypic changes in response to factor treatment may provide key information implicating or exonerating factor roles in CVS progression.

4.5 Discussion

Basal tone and induced contraction are important stress states due to the mechanical responses they elicit. It has been hypothesized that tissues have a preferred local stress and that they grow to maintain this stress [68]. Changes in this target stress, as measured by changes in basal tone here, result in growth rate changes. The initial decrease in functional basal tone induced by TGF-β (and thrombin), followed by increased functional basal tone over time (Fig. 4.6) may mirror the acute hypercontractile behavior in CVS and the increased growth and remodeling experienced in prolonged CVS, despite being counterintuitive (i.e. fewer contractile cells should result in decreased contraction). Similarly, by this consideration, PDGF appears to promote growth and remodeling at all times, possibly being critical in later stages of CVS.

In developing the traction force microscopy assay presented here, we consulted previously reported literature values to determine proper SAH-factor levels for treatment. A closer comparison of these values to those logarithmic concentrations used experimentally may explain the apparent limits of our assay in discerning changes in VSMC functional mechanics. Douglas et al. found an increase in TGF-β1 concentration from normal levels of 4 pM to 57 pM 1-5 days post hemorrhage [184]. If the effects of TGF-β1 are finely-tuned as a function of concentration, our treatment concentrations may not capture the *in vivo* behavior. Further, Kitazawa and Tada reported that changes in TGF-β concentration at later time points in CVS progression are minimal, yet heightened relative to normal levels [191]. This suggests that TGF-β may play a more critical role in chronic CVS progression compared to acute, which is supported by our counterintuitive interpretation of the functional phenotypic effects observed in response to TGF-β treatment (Fig. 4.6). Thrombin is reported to drastically decrease in concentration from 120 ng/ml at 2h post hemorrhage to 4.7 ng/ml at 48h post hemorrhage [192]. This timeframe suggests thrombin could be an ideal candidate for driving CVS mechanical progression, specifically due to its function as a vasoconstrictor. Our

experimental time points could miss the hyper-acute effects of thrombin and should be investigated in the future.

Endothelin-1-induced contraction is representative of VSMCs' ability to actively contract in maintenance of endothelial shear stress. In CVS, shear stress increases due to luminal narrowing [30]. This should result in decreased endothelin response, suggesting the shift toward synthetic phenotype observed in PDGF induced contraction (Fig. 4.6) could be important in CVS progression. Further work to rigorously predict the effects of pathologic changes in functional phenotype distributions on tissue response and the downstream consequences for arterial blood flow in the brain can be accomplished via computational modeling. These results represent behavior of sparse single VSMCs exposed to three factors known to increase in abundance as a result of SAH. VSMCs in native arteries experience much different architecture and surroundings, including cell-cell contacts and signaling. We can extend this work to investigate differences between "injured" solitary VSMCs and intact vascular architecture using a vascular muscular thin film technique as detailed in Chapter 3 and Appendix A, yielding a more complete understanding of the influence of SAH factors on cerebral vascular mechanics.

PA gel formed between glass coverslips

Global fibronectin attachment with sulfo-SANPAH

Sparse seeding w/ VSMCs
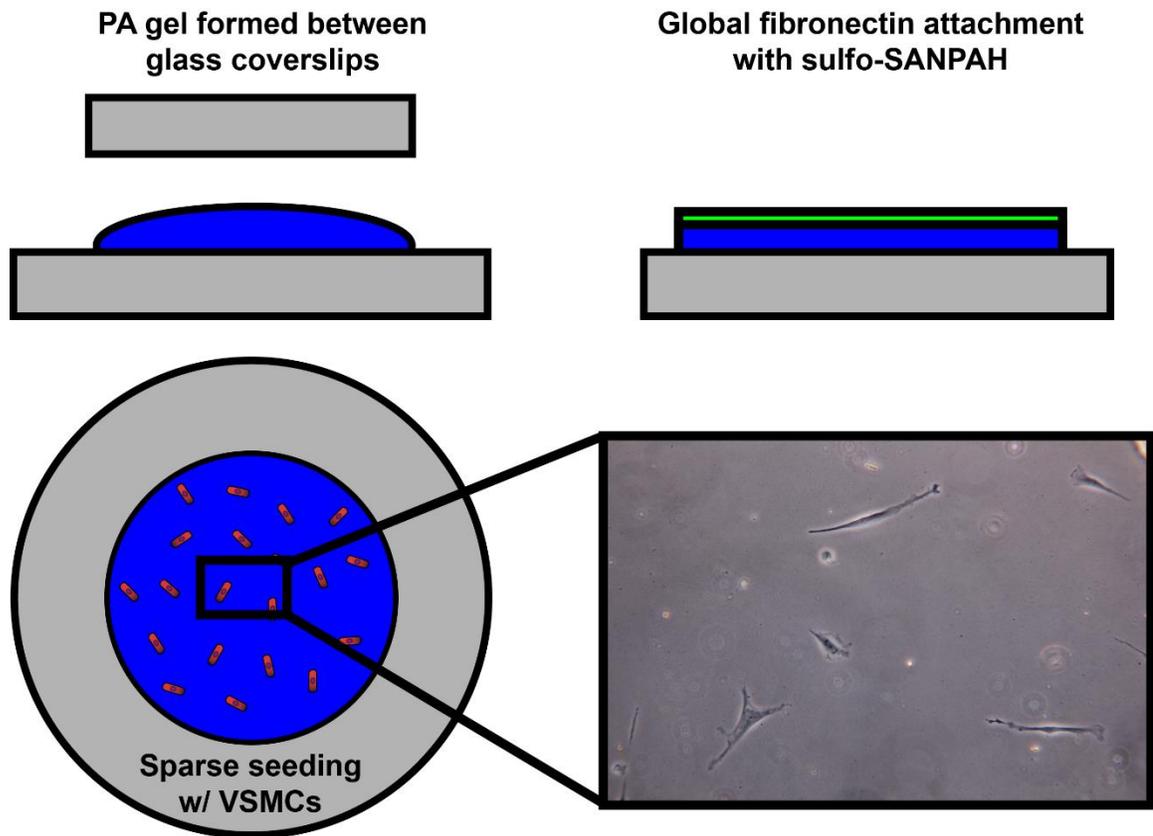
Figure 4.1. Polyacrylamide gel fabrication and sparse VSMC seeding.
Top left: A drop of polyacrylamide (PA, blue) is sandwiched between a bind-silane-functionalized cover slip (bottom, gray) and a 12-mm diameter glass cover slip (top, gray), forming a uniform gel of ~50 μm thickness. Top right: Fibronectin (green) is uniformly bonded to the PA gel surface via sulfo-SANPAH covalent bonding. Bottom left: VSMCs (red) are sparsely seeded on fibronectin-coated surface at a seeding density of ~5000 cells per sample. Inset: 10x phase contrast image of sparsely-seeded VSMCs attached to substrate.
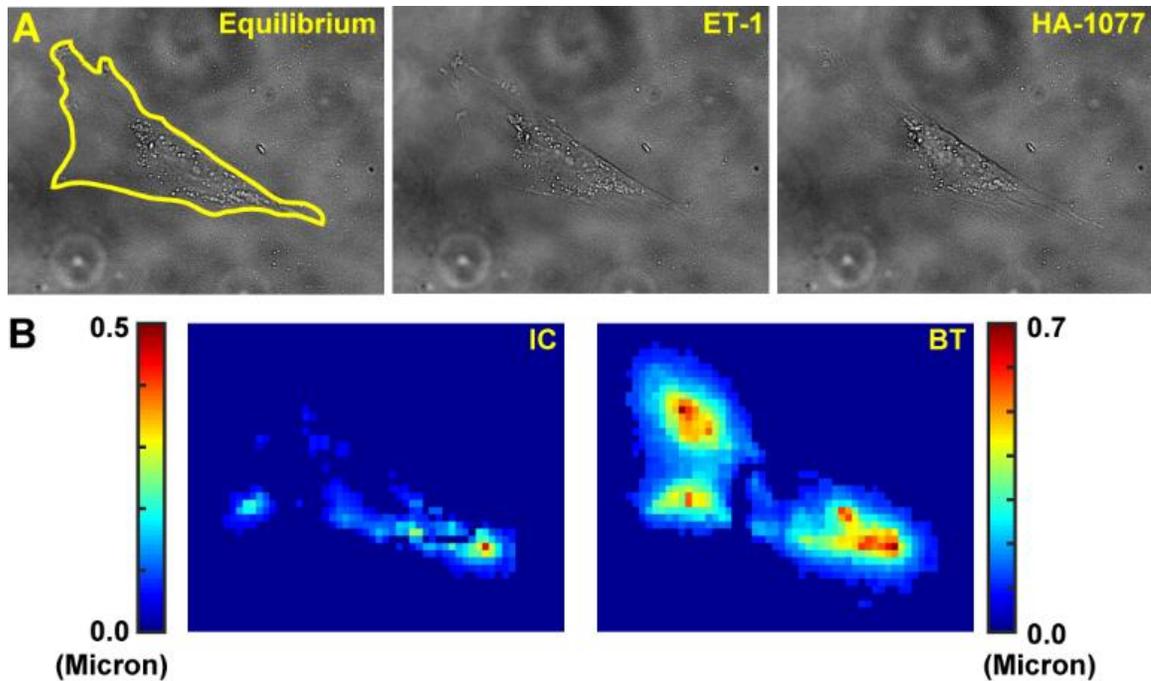
Figure 4.2. Traction force microscopy to determine functional mechanical output of single VSMCs.
(A) 40x brightfield images of a single VSMC cultured on polyacrylamide gel at three critical time points during a functional contractility assay: 1) Equilibrium; 2) Induced contraction via endothelin-1 treatment; 3) Relaxation via rho kinase inhibition with HA-1077. (B) Heat maps of corresponding displacement fields [190] in the polyacrylamide gels due to cell tractions for two important stress states: 1) Induced Contraction (IC, ET-1 – Equilibrium); 2) Basal Tone (BT, Equilibrium – HA-1077).
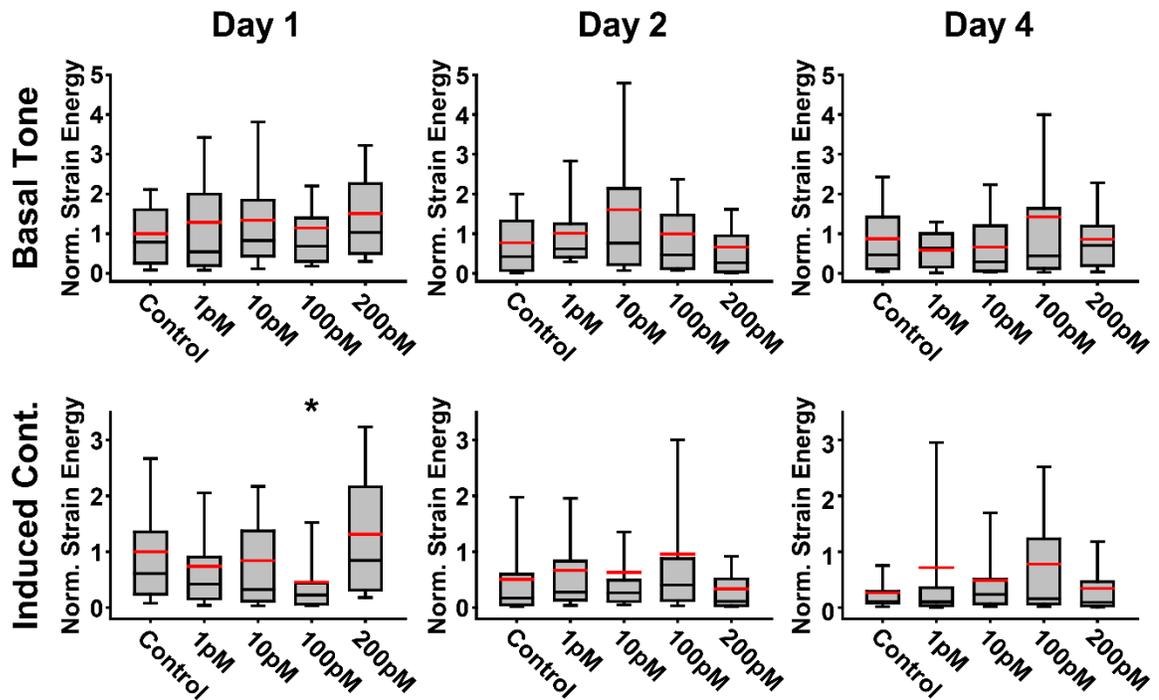
Figure 4.3. Effects of chronic transforming growth factor beta 1 (TGF-β1) treatment on VSMC functional contractility.

Chronic TGF-β1 treatment with four different treatment concentrations (pico-molar) for 1, 2, and 4 days has limited effect on basal tone and induced contraction of VSMCs as a function of total strain energy in PA gel substrates due to cell tractions (normalized to Day 1 controls). Box: 25-75%, Whiskers: 10-90%, Red Line: Mean, Black Line: Median, *: $p < 0.05$.
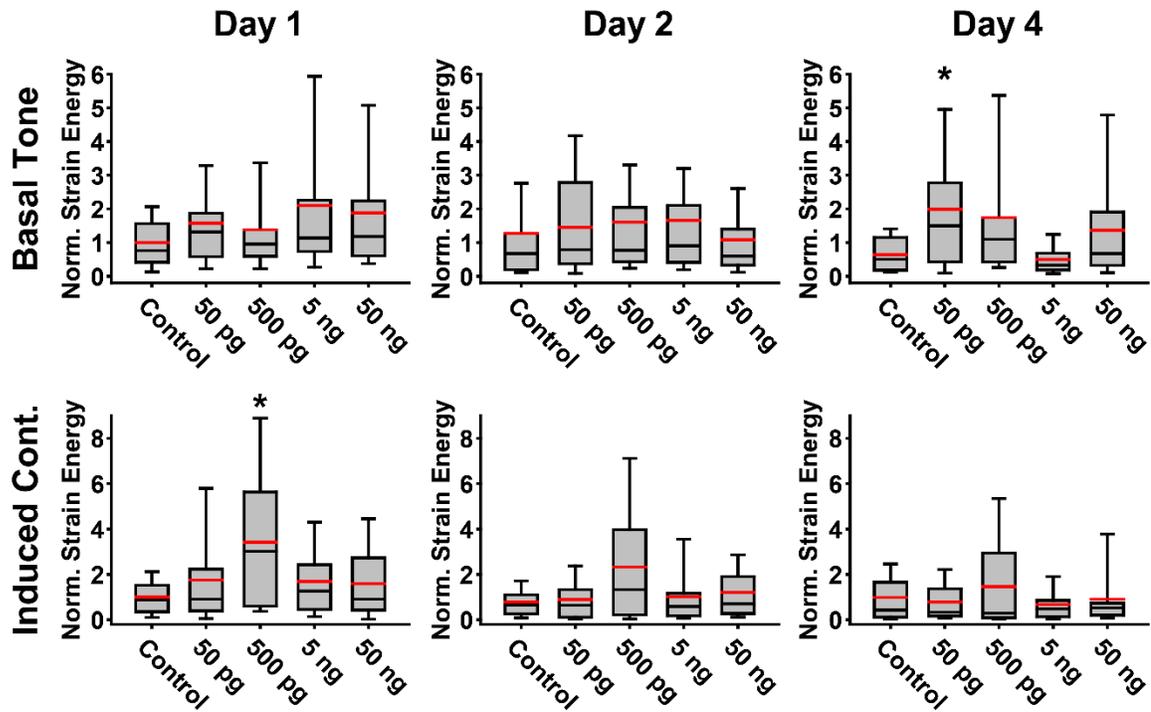
Figure 4.4. Effects of chronic platelet-derived growth factor (PDGF) treatment on VSMC functional contractility.
Chronic PDGF treatment with four different treatment concentrations (pg/mL or ng/mL) for 1, 2, and 4 days has limited effect on basal tone and induced contraction of VSMCs as a function of total strain energy in PA gel substrates due to cell tractions (normalized to Day 1 controls). Box: 25-75%, Whiskers: 10-90%, Red Line: Mean, Black Line: Median, *: $p < 0.05$.
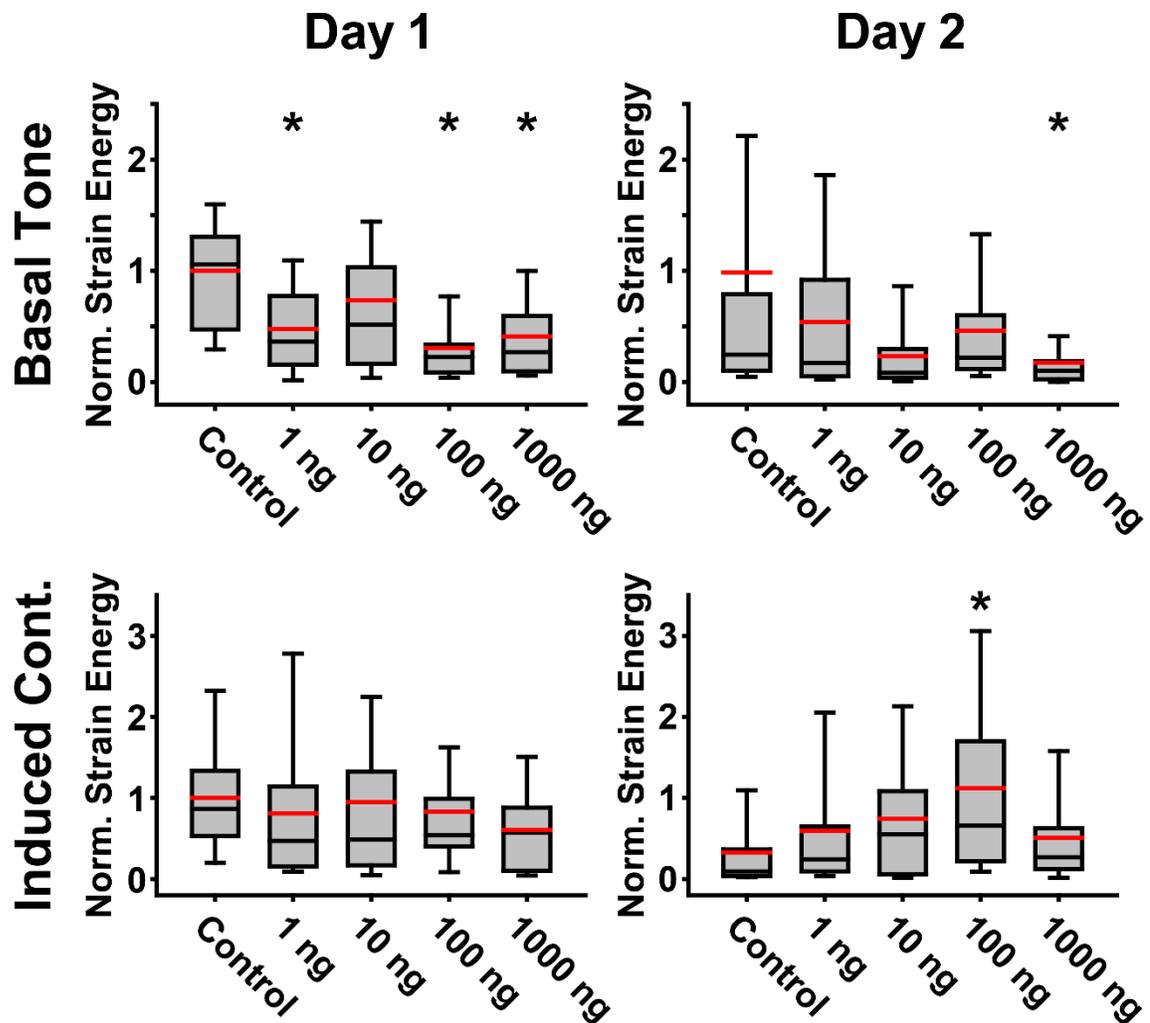
Figure 4.5. Effects of chronic thrombin treatment on VSMC functional contractility.
Chronic thrombin treatment with four different treatment concentrations (ng/mL) for one and two days (high rate of cell detachment/apoptosis by Day 4) significantly decreases basal tone on Day 1. On Day 2, basal function is significantly decreased for high concentration of thrombin (1000 ng/mL), and ET-1-induced contraction shows steady increase with increasing concentration. Total strain energy in the PA gel due to cell tractions are all normalized to Day 1 controls. Box: 25-75%, Whiskers: 10-90%, Red Line: Mean, Black Line: Median, *: p<0.05.
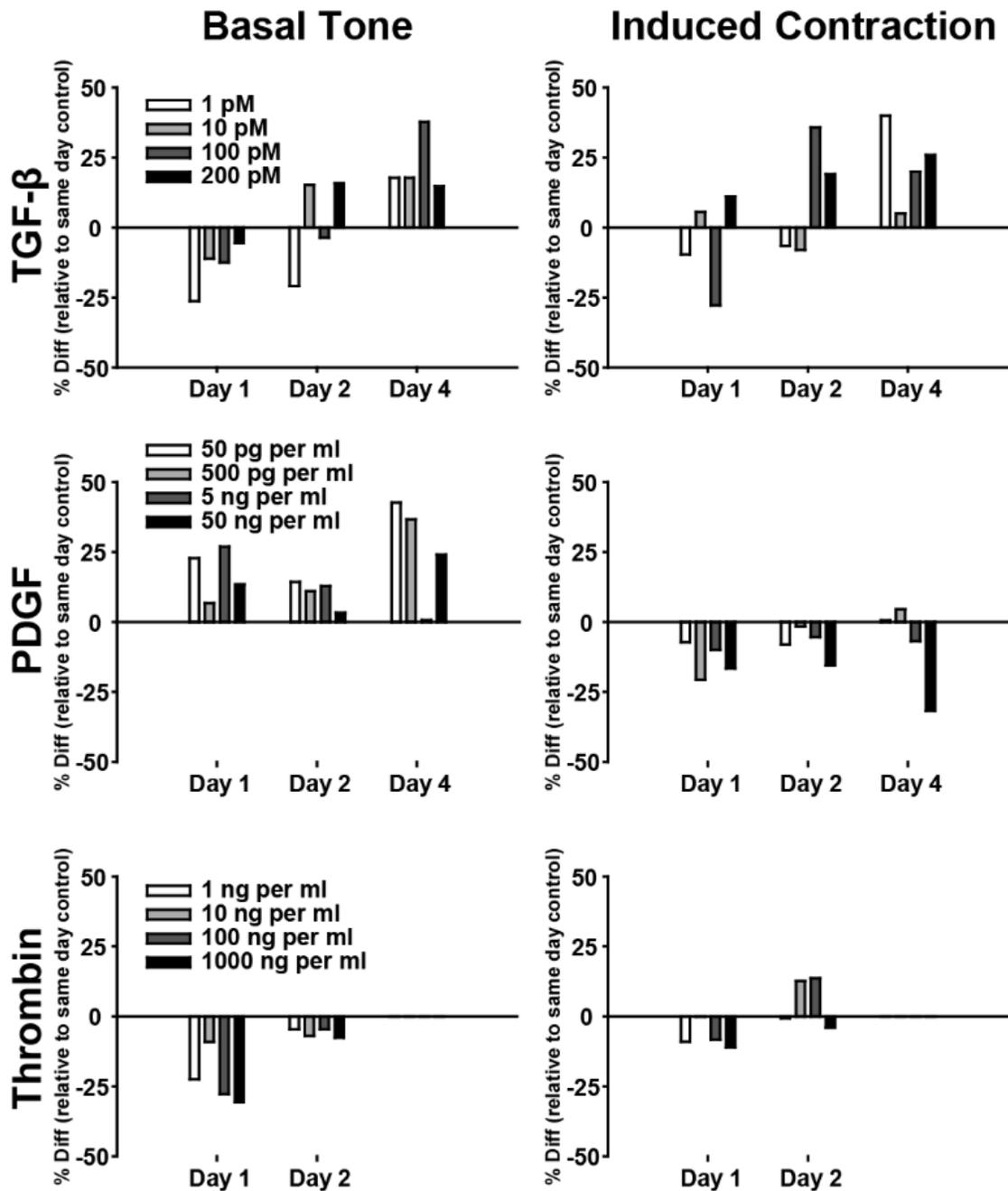
Figure 4.6. SAH factor-induced temporal functional phenotype distribution differences.
Treatment of VSMCs with three individual SAH factors (TGF-β1, PDGF, and Thrombin) induces different distributions of contractile and synthetic functional phenotypes. % Diff is relative to same day control contractile population (>1.0 threshold normalized to Day 1 control mean). Negative % Diff: more synthetic, % Diff: more contractile, 1: TGF-β1, Row 2: PDGF, Row 3: Thrombin.

Chapter 5. Amyloid Beta Influences Vascular Smooth Muscle Contractility and Mechano-Adaptation

5.1 Summary

Amyloid beta accumulation in neuronal and cerebrovascular tissue is a key precursor to development of Alzheimer's disease and can result in neurodegeneration. While its persistence in Alzheimer's cases is well-studied, amyloid beta's direct effect on vascular function is unclear. Here, we measured the effect of amyloid beta treatment on vascular smooth muscle cell functional contractility and modeled the mechano-adaptive growth and remodeling response to these functional perturbations. We found that the amyloid beta 1-42 isoform induced a reduction in vascular smooth muscle cell mechanical output and reduced response to vasocontractile cues. These data were used to develop a thin-walled constrained mixture arterial model that suggests vessel growth and remodeling in response to amyloid beta-mediated alteration of smooth muscle function leads to decreased ability of cerebrovascular vessels to vasodilate. These findings provide a possible explanation for the vascular injury and malfunction often associated with the development of neurodegeneration in Alzheimer's disease.

5.2 Introduction

Alzheimer's disease is a neurodegenerative disease diagnosed by dementia and the presence of amyloid beta (Aβ) plaques in the brain, most often in the elderly [193]. Aβ is a peptide formed by proteolytic cleavage of the amyloid precursor protein that can exist in both soluble monomeric and insoluble dimeric forms [194]. Typically, soluble Aβ is cleared from the neurovascular space via transport across the blood brain barrier (BBB) facilitated by low-density lipoprotein receptor-related protein 1 (LRP1) [195]. Disruptions in this clearance may lead to the formation of the insoluble plaques pervasive in Alzheimer's disease. These plaques, along with neurofibrillary tangles, are posited to result in direct insult to neurons in the cerebral cortex, providing the framework for the amyloid hypothesis in Alzheimer's disease development.

Aβ deposition is also a hallmark of cerebral amyloid angiopathy (CAA), which is present in over 80% of Alzheimer's patients and is a common precursor to Alzheimer's disease [16]. Aβ plaques can form in and around the cerebrovasculature with pathological effects on the function of cerebral arteries, disruption of the BBB, and changes in cerebral blood flow [2]. Two abundant isoforms of the Aβ peptide, 1-40 and 1-42, have been implicated in the development of CAA. Aβ 1-42 is the initial [196, 197] and more persistent [198] component of Aβ plaques that form in the media of arteries or wrap around the exterior arterial wall in CAA. The exact mechanisms by which Aβ induces arterial dysfunction in CAA are unclear, but it has been shown that cerebrovascular dysfunction can directly result in neuronal loss, a possible link to Alzheimer's disease progression [2]. Using transgenic Alzheimer's disease mouse models, Han et al. [17] found that CAA impacts vascular smooth muscle cell (VSMC)-mediated vasodilatory response. CAA also results in altered arterial wall structure [17, 199], and increased collagen deposition has been observed in cerebral arteries of Alzheimer's patients [200]. However, it is unclear how arterial structural adaptation in Alzheimer's disease affects vascular function.

56

Experimental evidence suggests three possible causes of vascular dysfunction in CAA: 1) physical inhibition of vasodilation by Aβ plaques, 2) limitation of VSMC dynamics due to physical alteration of the arterial wall, 3) alteration of VSMC contractile dynamics. Here, we focus on the role of VSMC contractile dynamics and consider the effects of changes in vessel wall composition on vasodilatory behavior during arterial growth and remodeling. Using traction force microscopy, we find that direct exposure to Aβ 1-42 induces significant decreases in basal stress and active contraction of VSMCs. To relate this finding to the adaptive response of cerebral arteries, we develop a constrained mixture model relating the change in VSMC basal stress to alteration of vessel function. We find that decreased VSMC function combined with a compensatory increase in collagen production can explain the decreased dynamic range and lost vasodilatory function of cerebral arteries in CAA patients. This work suggests the effects of Aβ on VSMC function and arterial structure may lead to the pathological cerebrovascular behavior that contributes to the progression of Alzheimer's disease as a result of CAA.

5.3 Methods: Experiment

5.3.1 Polyacrylamide Gel Fabrication and VSMC Culture

Polyacrylamide (PA) gels were fabricated as described by Tse and Engler [188]. Uniaxial stretch experiments were used to calculate a Young's modulus of 13.5±2.2 kPa for PA gels composed of: 10/0.13% w/v acrylamide/bis-acrylamide with 0.002/0.05% w/v initiators tetramethylethylenediamine/ammonium persulfate in 1X phosphate buffered saline solution. For traction force microscopy assays, gels were doped with 2% v/v 0.2-µm diameter red fluorescent microspheres. A 6.5-µL drop of PA gel solution was placed on 3% bind silane-functionalized cover slips. A clean 12-mm glass cover slip was placed on top of the gel drop to yield a uniform

PA gel of thickness ~50 μm upon gel curing. Cured PA gels were coated with 0.2 mg/ml sulfosuccinimidyl-6-(4'-azido-2'-nitrophenylamino)-hexanoate (Sulfo-SANPAH, Thermo Scientific, Rockford, IL) to covalently bond 50 ug/ml human fibronectin (Corning, Bedford, MA) to PA gel surfaces.

Human umbilical cord artery VSMCs (Lonza, Walkersvile, MD) were cultured in growth medium composed of M199 medium with 10% FBS, 10 mM HEPES, 1X Non-Essential Amino Acids, 3.5 g/L glucose, 2mM L-glutamine, 1% penicillin/streptomycin, and 2 mg/L Vitamin B_{12} supplement. For all cell structure and function assays, passages 5-7 were used to sparsely seed polyacrylamide constructs (~5000 cells per construct).

5.3.2 Amyloid Beta Treatment Assays

Sparsely-seeded VSMCs on PA gels were serum-starved after attachment for 24h to induce a physiologic contractile phenotype [167]. Stock solutions of amyloid beta peptides 1-40 (1 mg/ml in ddH_2O, APExBIO, Houston, TX) and 1-42 (1 mg/ml in 50 mM Tris buffer, Tocris Bioscience, Bristol, UK) were prepared. Experimental solutions were made by dilution of stock solutions in serum-free growth medium. Cells were then treated with prescribed treatment concentrations. For Day 2 and Day 4 assays, treatment solutions were changed every 24h.

5.3.2.1 VSMC Structure and Amyloid Beta Plaque Analysis

Treated VSMCs on PA gels were fixed in 4% paraformaldehyde and stained using immunofluorescence techniques. Briefly, cells were permeabilized with 0.05% Triton X-100, then blocked with 10% bovine serum albumin. Amyloid beta was stained using 1:200 rabbit polyclonal anti-amyloid fibril primary antibody (EMD Millipore, Temecula, CA) labeled with 1:200 Alexa Fluor 546 (Life Technologies, Eugene, OR) secondary antibody. F-actin and nuclei were stained with 1:200 Alexa Fluor 488 phalloidin (Life Technologies) and DAPI (Life Technologies),

respectively. Fluorescent images were acquired at 40x magnification with an Olympus IX81ZDC microscope.

Immuno-labeled amyloid beta fibrils were quantitatively analyzed using techniques similar to focal adhesion analysis of Xing et al. [162]. Single VSMCs were manually traced using ImageJ to determine cell areas. Pixel values outside the cell area were set to zero. An ImageJ rolling ball background subtraction plugin was used to autothreshold images. Images were then made binary, followed by sequential dilation and erosion steps. The ImageJ particle analysis function was used to quantify pixels with signal representing presence of amyloid beta fibrils/plaques. Total amyloid beta coverage was normalized by cell area for each individual cell, yielding percent coverage of amyloid beta.

Nuclei morphology was analyzed by thresholding DAPI images and fitting an ellipse to each single nucleus [161]. Nuclear eccentricity, ε, was calculated from the major and minor axis measurements according to

$$\varepsilon = \sqrt{1 - \left(\frac{minor\ axis\ length}{major\ axis\ length}\right)^2}.$$
(Eq. 5.1)

5.3.2.2 VSMC Functional Measurement

Mechanical function of VSMCs was measured by calculating the total strain energy of the substrate due to cell traction. To do so, traction force microscopy techniques were used [190]. Template matching between fluorescent bead images from two different time points was completed using Matlab's image registration function. Particle image velocimetry using iterative interrogation windows of 128-64-32 pixel width was completed between the matched bead images from the same cell location at different time points [190]. Noise filtering of the resulting displacement field was conducted by manually sampling an area outside of the cell tractions (field area) and removing all displacements less than the mean displacement of the field area plus five standard deviations. The noise-filtered displacement field was used to calculate traction stresses with a Fourier transform

traction cytometry (FTTC) ImageJ plugin [190]. A Poisson's ratio of 0.48, a Young's modulus of 13.5 kPa, and a regularization factor of 1e-9 were used for all FTTC calculations. Total strain energy of the substrate, U, was calculated for each individual VSMC using

$$U = \frac{1}{2}\int \boldsymbol{T} \cdot \boldsymbol{u} \, dxdy \qquad \text{(Eq. 5.2)}$$

where $\boldsymbol{T}$ is the traction stress and $\boldsymbol{u}$ is the displacement.

Traction force microscopy experiments were conducted for sparsely-seeded single VSMCs attached to 13.5 kPa PA gels. Control and treatment samples were run concurrently. Cells were maintained in a physiologic Tyrode's solution (7.889 g NaCl, 1.192 g HEPES, 0.901 g glucose, 0.403 g KCl, 0.265 g CaCl$_2$, 0.203 g MgCl$_2$, and 0.040 g NaH$_2$PO$_4$ per liter of ddH$_2$O). Physiological temperature was maintained within a heating chamber attached to an Olympus IX81ZDC microscope. Brightfield images of single VSMCs and z-stacks of their underlying bead-doped substrates were captured at four time points: equilibrium, 10 min post 50nM endothelin-1 treatment, 30 minutes post 100mM HA-1077 treatment, and post cell lysis with 5% sodium dodecyl sulfate.

Total strain energy, U, was calculated for two stress states: (1) basal tone and (2) ET-1-induced contraction. Basal tone strain energy was calculated using the bead displacement field resulting from the difference between images captured at equilibrium and 30 min post HA-1077 treatment. Similarly, ET-1-induced contraction strain energy was calculated using the bead displacement field resulting from the difference between images captured 10 min post ET-1 treatment and at equilibrium. Total strain energies were normalized to Day 1 control. Outlier analysis was conducted to remove all values above or below means by more than 1.5 times the interquartile range. Statistical comparisons for all experimental results were determined using Kruskal-Willis One Way ANOVA on Ranks and a Dunn's Method for pairwise multiple comparisons and a significance level of p<0.05.

5.4 Methods: Model

The model is a thin-walled, pseudo-elastic, incompressible pressurized cylinder composed of a constrained mixture of VSMCs, collagen, and elastin. The ECM components are treated as one-dimensional fibers within a VSMC scaffold. VSMCs are treated as transversely isotropic and contractile. ECM turnover is treated as previously described [180], wherein old fibers decay and are replaced by new fibers at a specified initial stretch ratio. Smooth muscle grows both radially and circumferentially. All growth and remodeling acts to maintain the muscle at a specified "target" stress and maintain luminal blood shear stress.

The model was used to test how a change in the VSMC target stress or contractile tone caused by Aβ accumulation might affect the global mechanics and function of the vessel. Two growth and remodeling modes were considered:

1) Total growth: Adaptation occurs through increased vessel volume, with volume fractions of each constituent conserved.
2) Collagen deposition: Adaptation occurs through altered collagen content with the volume of the other constituents remaining constant, altering the volume fractions of collagen, smooth muscle, and elastin.

In all models, the temporal dynamics of growth and remodeling were not considered; only the final homeostatic equilibrium state was examined.

5.4.1 Analysis

The model combines volumetric growth theory [8], pseudo-contraction [170], and collagen remodeling [201] to study how alteration of smooth muscle stress and contractility affects vessel mechanics. The fundamental assumption is that all of the components in the vessel wall move and deform together, but that each constituent has an evolving natural, zero-stress configuration.

5.4.2 Growth and Remodeling Theory

The loaded homeostatic state at time $t = 0$ is taken as the reference configuration denoted as $b(0)$ (Fig. 5.1). The constituents are constrained to move together, so that each constituent undergoes deformation, denoted by deformation gradient tensor $\boldsymbol{F}$, resulting in the current configuration $b(t)$. However, the constituents are treated separately because the zero-stress configuration of each can evolve independent of the other constituents. The deformation from the zero-stress configuration of constituent i (B^i) to $b(t)$ is given by its elastic deformation gradient tensor $\boldsymbol{F}^{*i}$. The method by which a constituent's zero-stress configuration evolves varies by constituent.

In the case of smooth muscle cells, suppose each cell is separated from every other cell and the ECM, giving configuration B^m. Because the cells are unconstrained, they are stress-free. In this unconstrained configuration, the cells can grow via either hypertrophy or hyperplasia. The deformation due to growth is described by the growth tensor $\boldsymbol{G}$. Following growth, the cells' new stress-free configuration is given by B^m_g. VSMCs can also contract, further altering their zero-stress configuration to B^m_a via the activation tensor $\boldsymbol{A}$. When the cells are reassembled and the vessel is loaded, the elastic deformation from B^m_a to $b(t)$ is given by $\boldsymbol{F}^{*m}$ (Fig. 5.1).

Collagen is treated as fibers that are produced and degraded with time. Between $t = 0$ and some time $t = \tau$, the vessel can undergo a deformation $\boldsymbol{F}_{0/\tau}$. When a collagen fiber is produced at time τ, its stress-free configuration is given by B^c. The fiber is then inserted into the matrix by the cell at an initial stretch ratio, λ^c_o. Further deformation from time τ to the current time t is given by deformation gradient tensor $\boldsymbol{F}_{\tau/t}$, and the elastic deformation from the zero-stress configuration B^c to the current configuration $b(t)$ is given by $\boldsymbol{F}^{*c}$ (Fig. 5.1). Elastin is assumed to undergo a similar remodeling protocol, though it is known that elastin remodeling

is temporally limited [202, 203]. The elastic deformation from the elastin zero-stress configuration B^e to the current configuration $b(t)$ is given by $\boldsymbol{F^{*e}}$ (Fig. 5.1).

5.4.3 Deformation and Mechanical Equilibrium

The deformation of the loaded artery $b(t)$ relative to reference state $b(0)$ is described by the mapping

$$r = r(R), \quad \theta = \Theta, \quad z = \Lambda Z \tag{Eq. 5.3}$$

for uniform inflation of a cylinder, where (R, Θ, Z) and (r, θ, z) are the cylindrical polar coordinates of a point in $b(0)$ and $b(t)$, respectively. The deformation gradient tensor $\boldsymbol{F} = diag[\lambda_r, \lambda_\theta, \lambda_z]$ is given by

$$\lambda_r = \frac{R}{r\Lambda} = \frac{h}{H}, \qquad \lambda_\theta = \frac{r}{R}, \qquad \lambda_z = \Lambda \tag{Eq. 5.4}$$

where h and H are the wall thicknesses in $b(0)$ and $b(t)$, respectively, and Λ is the axial stretch ratio.

The equation for radial equilibrium is given by

$$\frac{\partial \sigma_r}{\partial r} + \frac{\sigma_r + \sigma_\theta}{r} = 0 \tag{Eq. 5.5}$$

where σ_i are the Cauchy stresses. For a thin-walled cylinder with an internal pressure of P and wall thickness h, this simplifies to an equation for circumferential wall stress given by

$$\sigma_\theta = \frac{Pr}{h}. \tag{Eq. 5.6}$$

The fluid shear stress (τ_w) on the endothelium is approximated by Poiseuille flow, given by

$$\tau_w = \frac{4\mu Q}{\pi r^3} \tag{Eq. 5.7}$$

where Q is the volumetric blood flow rate, and μ is the viscosity of the blood (3 cp). We used pial artery pressure and flow rates given by $P = 30\ mmHg\ (4\ kPa)$ and $Q = 0.242\ \mu L/s$ [204].

5.4.4 Material Constitutive Laws

We let $\mathbf{F}^{*j} = diag[\lambda_r^{*j}, \lambda_\theta^{*j}, \lambda_z^{*j}]$ be the deformation gradient tensor of constituent j relative to its zero-stress configuration. For an incompressible pseudo-elastic material, the Cauchy stress is given by

$$\sigma_i^j = \lambda_i^{*j} \frac{\partial W^j}{\partial \lambda_i^{*j}} - p \tag{Eq. 5.8}$$

where j represents the constituent (elastin, collagen, smooth muscle), i is the coordinate axis (r, θ, or z), W^j is the constituent strain-energy density function, and p is a Lagrange multiplier.

We let V^j be the volume of the tissue composed of constituent j. The volume fraction of constituent j is given by

$$\phi^j = \frac{V^j}{\sum_j V^j} \tag{Eq. 5.9}$$

and $\sum_j \phi^j = 1$. The total Cauchy stress of the mixture is given by

$$\sigma_i = \sum_j \phi^j \sigma_i^j. \tag{Eq. 5.10}$$

5.4.4.1 Elastin

The strain-energy density for elastin is taken as

$$W^e = \frac{C^e}{2}(\lambda_\theta^{*e2} + \lambda_z^{*e2} + \lambda_\theta^{*e-2}\lambda_z^{*e-2} - 3) \tag{Eq. 5.11}$$

where C^e is a material parameter taken to be 24.91 kPa based on Cheng et al. [174]. Elastin does not significantly remodel post-birth [203]. We assumed that the elastin in the model was at a mature homeostatic stretch λ_o^e in the loaded configuration so that $\lambda_\theta^{*e} = \lambda_z^{*e} = \lambda_o^e$. In all models, we let $\lambda_o^e = 1.1$.

5.4.4.2 Collagen

The strain-energy density for collagen is taken as

$$W^c = \sum_{k=1}^{2} \frac{C^c}{\beta}\left(e^{\beta(I_4^{*k}-1)^2} - 1\right) \tag{Eq. 5.12}$$

64

where C^c and β are material parameters taken to be 42.32 kPa and 0.08, respectively, based on Cheng et al. [174]. I_4 is the 4th strain invariant given by $I_4^* = C_{\theta\theta}^* \cos^2(\alpha^k) + 2C_{\theta z}^* \sin(\alpha^k)\cos(\alpha^k) + C_{zz}^* \sin^2(\alpha^k)$, where C_{ij}^* is the i,j component of the elastic right Cauchy-Green tensor, defined as $\boldsymbol{C}^* = \boldsymbol{F}^{*T} \cdot \boldsymbol{F}^*$, and α is the angle of the collagen fibers with respect to the undeformed circumferential orientation. Humphrey and Rajagopal proposed that when collagen turns over, old fibers are replaced by new fibers at a preferred stretch ratio λ_o^c [201]. Here, we assume that the vessel is at homeostasis and has been for some time, so that $\lambda_i^{*c} = \lambda_o^c$ for all fibers in the loaded configuration, and we assume $\lambda_o^c = 1.2$.

5.4.4.3 Vascular Smooth Muscle

Smooth muscle strain energy is taken as

$$W^m = \frac{C^m}{2}(I_1^* - 3) + \frac{A^m}{2}(\lambda_\theta^{*m} - 1)^2 \qquad \text{(Eq. 5.13)}$$

where C^m and A^m are material parameters taken to be 10 kPa and 100 kPa, respectively. I_1^* is the first strain invariant with respect to the zero-stress configuration, given by $I_1^* = \lambda_r^{*m\,2} + \lambda_\theta^{*m\,2} + \lambda_z^{*m\,2}$. Muscle acts to adapt the vessel quickly to changes in its mechanics via contraction, but to do so, it must maintain a homeostatic partially-contracted state described by the stress-free cell shortening λ_{ao} [9]. In all models, we assumed that the loaded active artery is at this homeostasis, and VSMC contractile cytoskeletons are primarily oriented circumferentially, so that $\boldsymbol{A} = diag[1, \lambda_{ao}, 1]$. VSMCs can also grow via hypertrophy or proliferation to alter their stress. Though axial growth and remodeling plays an important role in vessel mechanics [73, 205, 206], here, we ignored its effect and only included radial growth (thickening) λ_{gr} and circumferential growth $\lambda_{g\theta}$. Thus, the growth tensor is given by $\boldsymbol{G} = diag[\lambda_{gr}, \lambda_{g\theta}, 1]$.

5.4.5 Mechano-adaptation Models

Three mechano-adaptation models were considered: total growth, collagen deposition, and altered contraction/collagen deposition.

5.4.5.1 Total Growth

The central assumption of the total growth model is that all constituents increase or decrease in volume equally to maintain homeostasis. The arterial wall acutely contracts and chronically grows via cytoskeletal remodeling to maintain endothelial shear stress [9]. Here, we ignore acute contraction and assume that, at homeostasis, actin stress-free shortening is equal to λ_{ao}, which we set to 0.8. Thus, long-term maintenance of shear is achieved through the growth tensor $\boldsymbol{G}$. We assume that circumferential growth is governed by fluid shear stress via the relation

$$\frac{\dot{\lambda}_{g\theta}}{\lambda_{g\theta}} = A(\tau_w - \tau_o) \tag{Eq. 5.14}$$

where $\dot{\lambda}_{g\theta}$ is the derivative with respect to time of $\lambda_{g\theta}$, A is a constant, τ_w is the luminal blood shear stress (Eq. 5.7), and τ_o is the optimal shear stress, assumed to be 15 dyne/cm^2 [207]. In addition, the wall grows thicker or thinner to maintain VSMC target stress. Radial growth is given by

$$\frac{\dot{\lambda}_{gr}}{\lambda_{gr}} = B(\sigma_\theta^m - \sigma_o) \tag{Eq. 5.15}$$

where B is a constant, and σ_o is the target stress, assumed to be 75 kPa. In the total growth model, the relative volume of constituents remains constant, i.e. ϕ^i is constant for all i, so the change in volume due to VSMC growth is equally reflected in the collagen and elastin. Similar to Intengan et al. [208], we use $\phi^c = 0.23, \phi^e = 0.17, \phi^m = 0.60$ in this model for small arteries.

5.4.5.2 Collagen Deposition

In the collagen deposition model, we assumed that increased thickening of the vessel is due to additional deposition of collagen, not VSMC growth or elastin deposition. This model uses the growth formulation of the total growth model, but adds the relation

$$\dot{V}^c = \frac{\dot{\lambda}_{gr}}{\lambda_{gr}} \sum_j V^j \qquad\qquad \text{(Eq. 5.16)}$$

where V^c is the volume of collagen, and j is collagen, elastin, and smooth muscle. The VSMC and elastin volumes remain constant, resulting in altered volume fractions of each constituent (Eq. 5.9).

5.4.5.3 Altered Contraction/Collagen Deposition

The altered contraction model uses the growth and collagen deposition formulation of the collagen deposition model. In addition, the homeostatic stress-free shortening (λ_{ao}) is prescribed over the range 0.55-0.95 to test how contractile tone affects remodeling.

5.4.6 Numerical Implementation

The governing equations were solved using a Nelder-Mead minimization. Initially, λ_{gr} and $\lambda_{g\theta}$ were iterated, while all other parameters were held constant until $\sigma_\theta^m = \sigma_o$ and $\tau_w = \tau_o$. Target stress, σ_o, was then incremented and, depending on the mechano-adaptation method, λ_{gr}, $\lambda_{g\theta}$, and/or ϕ^c were solved using finite differences until $\sigma_\theta^m = \sigma_o$ and $\tau_w = \tau_o$ with error criterion of $1 \times 10^{-12}\ Pa$. Pressure-radius curves were calculated by holding all parameters constant except P ($\lambda_a = \lambda_{ao}$ for active curves, $\lambda_a = 1$ for passive curves) and calculating the resulting radius. Vasodilation data were calculated as the ratio of

the vessel radius of the passive vessel at physiologic pressure to the radius of the active vessel at physiologic pressure.

5.4.7 Parameter Determination

When possible, parameters were determined from the literature. The parameters $\sigma_o, \lambda_o^e, \lambda_o^c, C^m, A^m$, and λ_{ao} were set to yield a pressure-radius behavior that matches those experimentally measured by Steelmann et al. [204]. We conducted parameter studies to determine the influence of certain parameters on the vessel growth and remodeling mechanical response in the collagen deposition case (see Appendix B). Here, we only studied the homeostatic implications of remodeling, not the temporal course, so we used unitless time in Eqs. 5.14-5.16. For all models, the growth parameters A and B were $3 \times 10^{-4} \ Pa^{-1}timestep^{-1}$ and $1 \times 10^{-7} \ Pa^{-1}timestep^{-1}$, respectively.

5.5 Results

5.5.1 Amyloid Beta Does Not Influence Intracellular Morphology

We sought to determine the effects of exposure to Aβ on VSMCs. We applied natural human Aβ 1-42 to VSMCs seeded on polyacrylamide (PA) gels and found plaque aggregation of Aβ within 24 hours after initial treatment. Aggregation increased with increasing treatment concentration (Fig. 5.2 A). This was consistent with previous studies showing synthetic human Aβ 1-42 fibril plaque formation occurs *in vitro* [209]. Quantitative assessment of Aβ plaque coverage showed increasing plaque coverage with increasing Aβ concentration. In the highest concentration group (10 μM Aβ), 40% of the cell area was plaque covered (Fig. 5.2 B,C).

Cell spread area is known to affect cell traction stress [210], so we measured the effect of Aβ treatment on VSMC spread area and found that it was

consistent across all treatment groups (Fig. 5.2 D). Nuclear morphology has been previously shown to correlate to changes in VSMC function [84, 211], so we measured the eccentricity of the nuclei in Aβ-treated VSMCs. We found a non-significant increasing trend in nuclear eccentricity as Aβ treatment concentration increased (Fig. 5.2 E). Taken together, these data demonstrate that Aβ treatment does not significantly affect VSMC architecture.

5.5.2 Amyloid Beta Influences VSMC Functional Contractility

Changes in VSMC functional contractility could mediate cerebrovascular dysfunction associated with Alzheimer's disease [2]. We sought to determine the influence of Aβ accumulation on VSMC function. We used traction force microscopy to calculate total strain energy in polyacrylamide (PA) gels due to VSMC traction forces (Fig. 5.3 A,B). Generally, exposure to Aβ caused a decrease in the basal strain energy. Treatment with 100 nM and 10 µM Aβ 1-42 yielded significant decreases in normalized total strain energy relative to control after 24h, though surprisingly, 1 µM Aβ 1-42 did not (Fig. 5.3 C). We found similar trends in decreased VSMC basal contractility after 48h and 96h of treatment (Fig. 5.3 D,E). Treatment with Aβ 1-40 did not show any effect on basal strain energy (data not shown).

Cerebral blood flow is tightly regulated by neural activation [3], requiring a highly-dynamic cerebral vasculature. To determine the effect of Aβ on VSMC active contraction, we measured the strain energy generated by VSMCs exposed to the vasoconstrictor endothelin-1 (ET-1). Similar to our basal tone data (Fig. 5.3 C), we found decreased ET-1-induced contractility after 24h of treatment with Aβ 1-42 (Fig. 5.3 F), suggesting that decreasing tone corresponds with a more general loss of contractile dynamics. See Appendix C for additional functional contractility investigation.

5.5.3 Growth and Remodeling Affects Vessel Properties and Vasodilation

We sought to investigate the impact Aβ-mediated loss of VSMC functional contractility has on arterial function at the tissue scale. To do so, we developed a thin-walled, constrained mixture model (see Fig. 5.1) for the cerebral vasculature in which the artery can undergo remodeling through growth and remodeling. We assumed that the VSMCs have a preferred target stress, which correlates with the basal strain energy measured in PA gels due to individual cell traction (Fig. 5.3 C). We asked how alteration of the target stress due to Aβ exposure might affect vessel growth and remodeling. We considered two growth and remodeling cases: total growth and collagen deposition.

In the total growth case, as the target stress was decreased, the vessel wall thickened and the volume fractions of cells and collagen remained constant (Fig. 5.4 A). In addition, the circumferential growth ($\lambda_{g\theta}$) needed to maintain endothelial shear increased as target stress decreased (Fig. 5.4 B). Pressure-radius curves for varying target stresses shifted, showing increasing apparent stiffness in the modeled vessel with decreasing target stress (Fig. 5.4 C). Han et al. found that cerebral arteries in a transgenic mouse model expressing mutant amyloid precursor protein displayed a decreased ability to vasodilate [17]. We tested the effect of total growth on vasodilation by simulating the change in radius when VSMC tone is relaxed. As the ratio of the radius of the passive artery to the radius of the actively-contracted artery approaches one, vasodilation becomes fully-attenuated. We found that the ability of the vessel to relax decreases with decreasing target stress (Fig. 5.4 D).

In the collagen deposition case, the vessel wall thickened, the amount of collagen increased, and the volume fraction of smooth muscle cells decreased with decreasing target stress (Fig. 5.5 A). Similar to total growth, circumferential growth ($\lambda_{g\theta}$) increased as target stress decreased (Fig. 5.5 B), and pressure-radius curves showed increasing apparent stiffness with decreasing target stress (Fig. 5.5 C). This stiffening was more severe than was observed in the total growth model. When we tested the ability of the vessel to vasodilate, we again saw decreased

dilation with decreasing target stress (Fig. 5.5 D). This decrease was markedly sharper than the one seen in the total growth model.

Next, we asked how the observed loss of the ability of VSMCs to actively contract (see Fig. 5.3 F) could affect vessel growth and remodeling. This decreased contractility can be represented as an increase in the homeostatic active stretch ratio (λ_{ao}) in our model. We considered the effect of altered contractility within the collagen deposition model. We found that as λ_{ao} increases, the pressure-radius curve of the activated vessel becomes less stiff and the passive vessel becomes stiffer (Fig. 5.6 A). In addition, the ability of the vessel to dilate severely decreases for all target stresses as active contractility is decreased (Fig. 5.6 B). Combined decrease in target stress and ability of VSMCs to actively contract resulted in greater attenuation of vasodilation. These data suggest that growth and remodeling due to changes in both VSMC target stress and ability of VSMCs to contract resulting from exposure to Aβ could contribute to the observed attenuation of vasodilatory response in CAA and Alzheimer's disease.

5.6 Discussion

Arterial dysfunction can play an important role in Alzheimer's disease development. To date, the effect of Aβ exposure on VSMC force generation and functional contractility, and the downstream implications these effects have on arterial growth and remodeling, are not known.

Here, we directly measured the contractility of VSMCs to determine the influence of Aβ exposure on their function. We found significant decreases in basal tone and induced contraction when treated with Aβ 1-42 (Fig. 5.3 C-F). Previous work has shown induction of apoptosis in VSMCs cultured *in vitro* or on Aβ-coated substrates [212, 213]. We did not observe this in our assays utilizing media-contained Aβ treatment of VSMCs attached to PA gels and do not believe apoptosis contributed to our findings. Interestingly, Aβ concentrations that yielded

71

both minimal and significant plaque formation (Fig. 5.2 A,C) resulted in the measured functional decreases (Fig. 5.3 C). While we cannot rule out the formation of insoluble dimers in the lower concentration, it is possible that this result suggests both soluble and insoluble Aβ have a functional effect on VSMCs. Previously, synthetic Aβ 1-42 was shown to induce more production of its own soluble form and amyloid precursor protein in cultured degenerating VSMCs, but shorter Aβ isoforms do not [214], suggesting that the longer 1-42 isoform is primarily responsible for amyloidosis. This could explain the temporal drop in functional contractility in the intermediate concentration of 1 µM Aβ 1-42 treatment (Fig. 5.3 C-E). These data are also consistent with Han et al., who found decreased vessel function even at low levels of CAA plaque formation [17]. Our observed reduction in Aβ-treated VSMC response to vasoactive ET-1 stimulation (Fig. 5.3 F) suggests a possible mechanism by which arteries are limited in their ability to dynamically modulate cerebral blood flow.

Domnitz et al. found that Aβ plaques wrap around the cerebral vessels of transgenic mouse models, suggesting that a physical constraint limited their ability to vasodilate [215]. Here, we propose an alternative hypothesis: Exposure to Aβ decreases the stress borne by VSMCs. As a result, the vessel remodels, primarily via collagen deposition. This increased collagen content stiffens the vessel, which decreases its mechanical dynamics, inhibiting vasodilation. We tested this possibility using an *in vitro/in silico* approach. We employed a computational model for cerebrovascular growth and remodeling that assumes that each VSMC has an ideal target stress, and growth and remodeling acts to restore this stress [9]. We measured decreased basal force generation in VSMCs exposed to Aβ (Fig. 5.3 C). Since the cell's stress is not constrained by external loads, we took this result to represent a decrease in target stress. The computational model suggests that this decrease in target stress, coupled with compensatory collagen production, yields increased collagen content consistent with observations in Alzheimer's disease patients [200], and can result in increased stiffness (Fig. 5.5 C) and decreased

vasodilation (Fig. 5.5 D), even in the absence of a loss of contractile dynamics. However, we also measured an Aβ-mediated decrease in ET-1-induced contractility (Fig. 5.3 F), suggesting that the ability of VSMCs to contract is also affected by Aβ. When decreased ability to contract was added to the model, we found an even greater decrease in vasodilation (Fig. 5.6 B). Taken together, these data suggest that mechano-adaptation could drive the observed change in vasodilation in the absence of physical restriction by plaques.

The inability of VSMCs to respond normatively to changes in vessel mechanics or vasoactivation via endothelin-1-induced contraction (Fig. 5.3 F) could contribute to breakdown of the BBB in the intact neurovasculature [2]. Such a breakdown has shown to downregulate LRP-1, which is responsible for the physiological clearance of Aβ across the BBB [216]. Aβ decreases contractility in VSMCs (Fig. 5.3), which, in addition to reported VSMC atrophy in the vessel media in CAA [217], could increase the likelihood of vessel rupture [218], releasing neurotoxic factors into the brain parenchyma. Atrophy and loss of vasomotor response can both contribute to hypoperfusion, which has been shown to exacerbate Aβ aggregation in synapses [219] and lead to hypoxia. Recent findings have suggested that oxidative stress is critical in the ultimate downstream consequences of Alzheimer's disease precursors: neuronal death [220, 221].

There are some important limitations to consider in this study. Experimental studies were all conducted on single VSMCs, which are not perfect mimics of *in vivo* vascular tissues. The importance of cell-cell signaling, interactions with surrounding composite ECM, and the propagation of mechanical force throughout the tissue as a continuum are not captured in this work. Also, the choice of extracellular matrix adhesion proteins used in *in vitro* studies of VSMC function can influence VSMC phenotype [222], as well as amyloidosis [223]. Here, we used fibronectin as the only adhesion ECM protein, which limits the robustness of our study. While this is a limitation, all VSMCs were cultured in serum-free medium, which has been shown to promote a contractile VSMC phenotype [167],

superseding the reported shift in VSMCs cultured on fibronectin toward a synthetic phenotype [224]. Finally, the model we developed to assess the effects of VSMC loss of function on arterial mechanics during growth and remodeling is necessarily simplified compared to *in vivo* vessels. For example, by assuming a uniform thin-walled vessel, we ignore the contributions of the adventitia to vessel mechanics. Additionally, in the total growth case, elastin increases with collagen and smooth muscle, though it is well-established that elastin does not functionally remodel in mature arteries [203]. Finally, our model only examines the endpoints of remodeling and does not describe the temporal evolution of vessel mechanics during disease progression.

5.7 Conclusion

In this study, we show that culture with Aβ induces changes in VSMC mechanical behavior that may be critical in the maladaptive response of cerebral arteries during the development of Alzheimer's disease and other neurological disorders. The significance of VSMC function at the single cell level has been elusive amid the vast work completed in developing the amyloid hypothesis. Our results suggest that vascular injury mechanisms and downstream degeneration of neurons could be the consequence of loss of function due to biochemical attenuation of VSMC contractility by soluble and insoluble forms of Aβ and vessel remodeling to compensate for this functional loss. Further work to show the impact of Aβ on VSMCs in their native configuration is needed to fully understand the influence of Aβ in the pathology of cerebrovascular tissue.
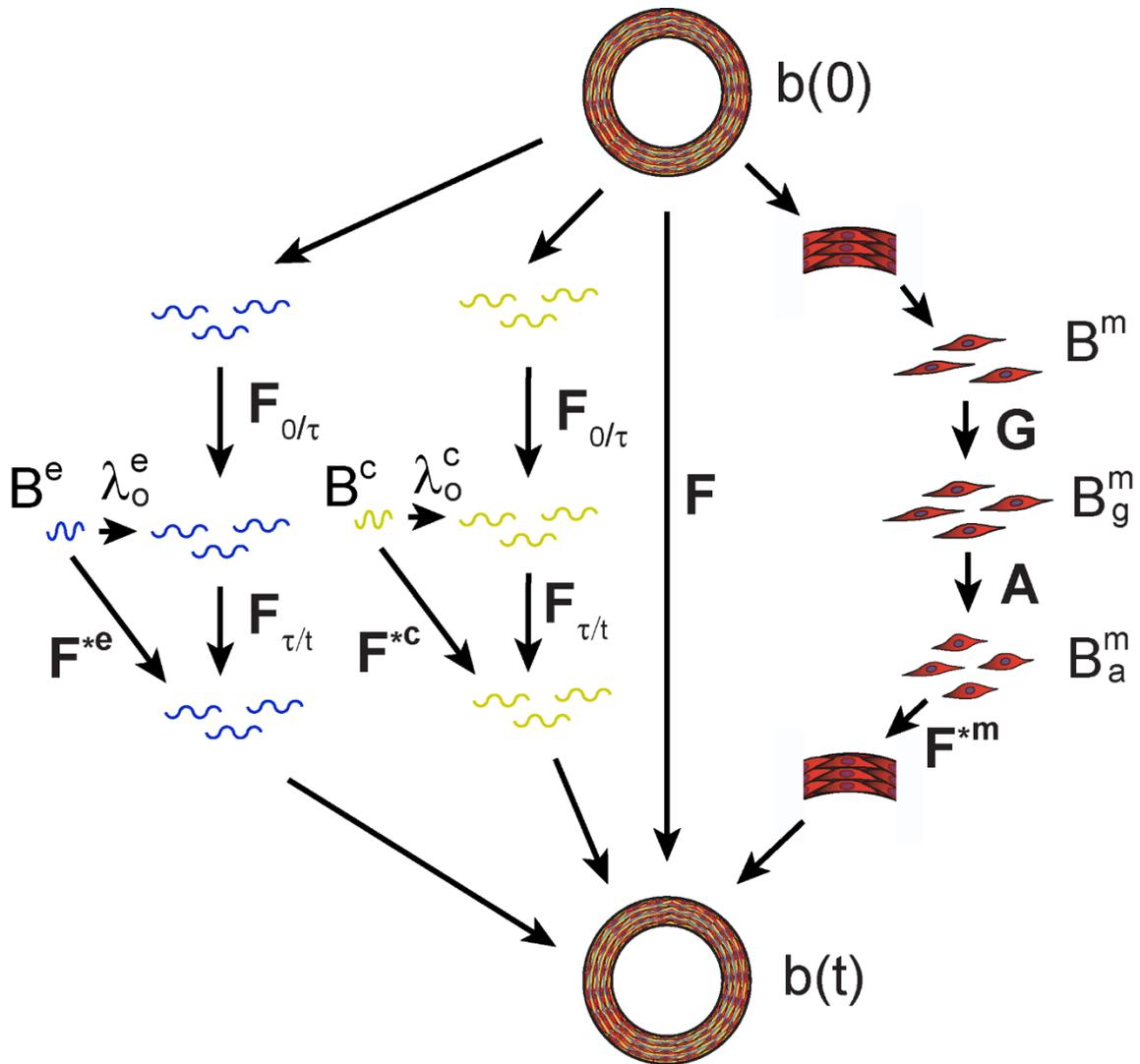
Figure 5.1. Schematic of growth and remodeling in thin-walled, constrained mixture arterial model.
All constituents (elastin: left, blue; collagen: middle, yellow; muscle cells: right, red) undergo deformation F, transitioning the artery from a reference configuration, $b(0)$, to a current configuration, $b(t)$. But, their zero-stress configurations evolve separately, yielding different elastic deformations. Zero-stress configurations are denoted by capital letters. Elastin and collagen are produced and degraded with time, with insertion at a prescribed initial stretch ratio, λ_o^e or λ_o^c. Deformation from the zero-stress configuration, B^e or B^c, to the current configuration is denoted by the elastic deformation gradient tensor, F^{*e} or F^{*c}. Muscle cells undergo stress-free deformation due to growth, G, and active contraction, A. Upon reassembly and vessel loading, there is an elastic deformation, F^{*m}, from the zero-stress actively contracted state, B_a^m, to the current configuration, $b(t)$.

75
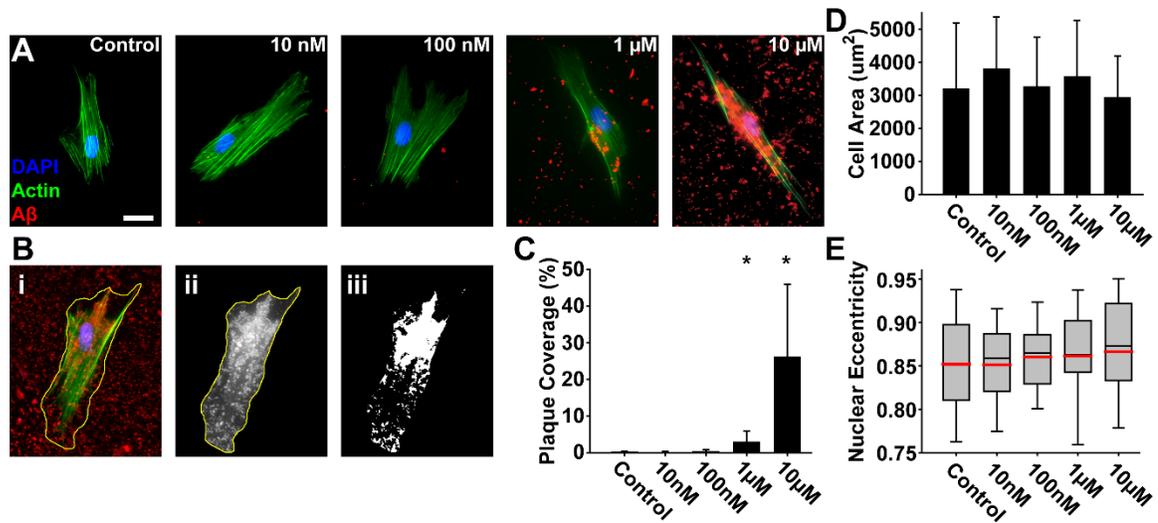
Figure 5.2. Treatment of VSMCs with Aβ yields differences in Aβ plaque formation and nuclear morphology.
(A) Representative immunofluorescent images of single VSMCs for different treatment conditions; blue: DAPI-stained nuclei, green: f-actin, red: Aβ fibrils, scale bar: 25 μm (B) (i) Traced VSMC for Aβ plaque coverage quantification (ii) Isolation of VSMC area in Aβ-stained image (iii) Thresholded Aβ signal for particle analysis (C) Aβ plaque coverage after 24 hr of treatment; Error bars: standard deviation, *: significant difference, p<0.05 (D) Cell spread area after 24 hrs of Aβ treatment; Error bars: standard deviation (E) VSMC nuclear eccentricity after 24 hrs of Aβ treatment; Boxes: 25-75%, Whiskers: 10-90%, Red (thick) line: Mean, Black (thin) line: Median.
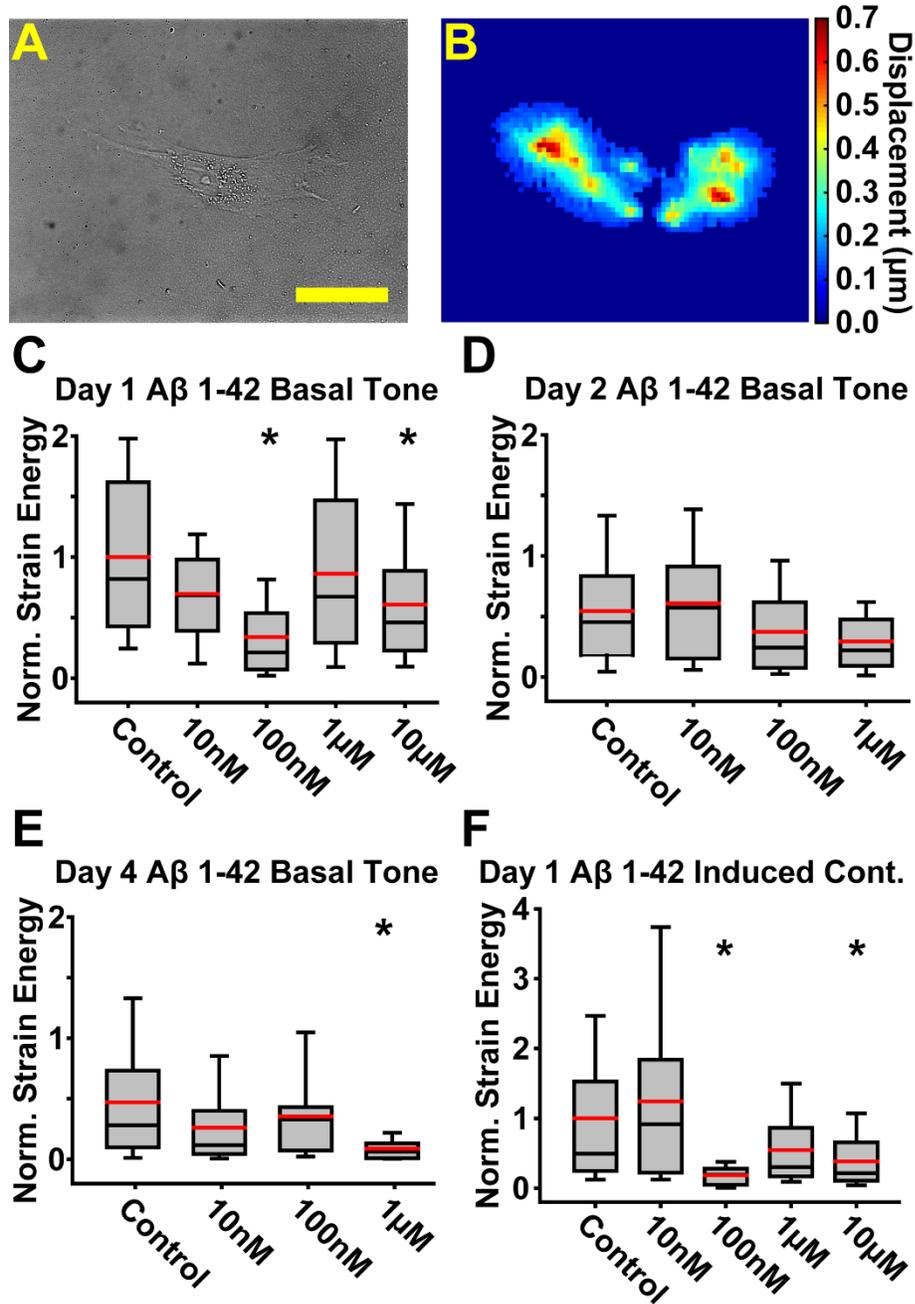
Figure 5.3. Amyloid beta influences VSMC basal functional contractility.
(A) Representative brightfield image of VSMC on PA gel, scale bar: 100 μm (B) Heat map of measured substrate displacement resulting from VSMC traction (C-E) Basal strain energy exerted by cells treated for 24 hr (C), 48 hr (D), and 96 hr (E) with Aβ 1-42 (F) ET-1-induced contraction strain energy following 24 hr treatment with Aβ; *: significant difference, $p < 0.05$; Boxes: 25-75%, Whiskers: 10-90%, Red (thick) line: Mean, Black (thin) line: Median.
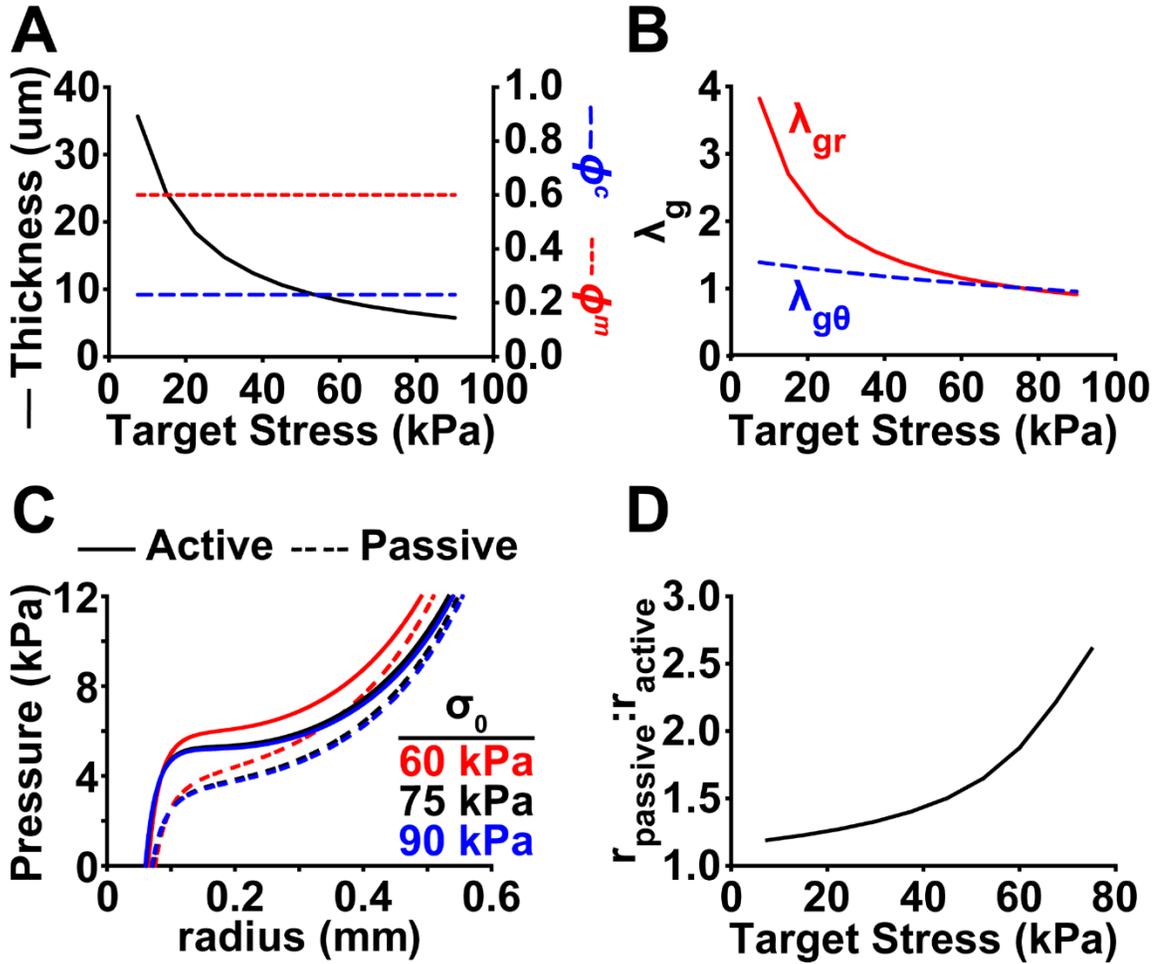
Figure 5.4. Thin-walled constrained mixture total growth model of cerebrovascular response to altered target stress.
(A) Vessel wall thickness (solid line) and volume fractions of collagen (ϕ^c, long dashed line) and VSMCs (ϕ^m, short dashed line) (B) Circumferential growth stretch ratio, $\lambda_{g\theta}$ (dashed line), and radial growth stretch ratio, λ_{gr} (solid line), relative to baseline homeostatic conditions ($\sigma_o = 75kPa$) (C) Pressure-radius curves for active (solid lines) and passive (dashed lines) mechanical responses for specified target stress (Red: 60 kPa, Black: 75 kPa, Blue: 90 kPa; increasing target stress from top left to bottom right for both active and passive curves) (D) Vasodilation, represented as the ratio between the passive vessel radius, $r_{passive}$, and the active vessel radius, r_{active}, as a function of target stress.

Figure 5.5. Thin-walled constrained mixture collagen deposition model of cerebrovascular response to altered target stress.
(A) Vessel wall thickness (solid line) and volume fractions of collagen (ϕ^c, long dashed line) and VSMCs (ϕ^m, short dashed line) (B) Circumferential growth stretch ratio, $\lambda_{g\theta}$ (dashed line), and radial growth stretch ratio, λ_{gr} (solid line), relative to baseline homeostatic conditions ($\sigma_o = 75kPa$) (C) Pressure-radius curves for active (solid lines) and passive (dashed lines) mechanical responses for specified target stress (Red: 60 kPa, Black: 75 kPa, Blue: 90 kPa; increasing target stress from top left to bottom right for both active and passive curves) (D) Vasodilation, represented as the ratio between the passive vessel radius, $r_{passive}$, and the active vessel radius, r_{active}, as a function of target stress.

Figure 5.6. Loss of VSMC ability to actively contract attenuates vasodilation in model vessels.

(A) Pressure-radius curves for active (solid lines) and passive (dashed lines) mechanical responses for specified homeostatic active stretch ratio, λ_{ao} (Red: 0.60, Black: 0.80, Blue: 0.95; increasing λ_{ao} from top left to bottom right for active curves, decreasing λ_{ao} from top left to bottom right for passive curves), and target stress $\sigma_o = 75\ kPa$ (B) Vasodilation, represented as the ratio between the passive vessel radius, r_passive, and the active vessel radius, r_active, as a function of changes in the active stretch ratio, λ_{ao}, for specified target stress (Red, short dashed line: 45 kPa, Blue, long dashed line: 60 kPa, Black, solid line: 75 kPa).

Chapter 6. Conclusions and Future Directions

This work builds upon previously developed microfabrication techniques for measuring vascular mechanics in two ways: 1) validated improvement of an established technique to expand application and improve upon disease-relevance of temporal experiments (Chapter 3, Appendix A) and 2) use of established techniques to elucidate novel functional mechanics resulting from disease-associated biochemical treatments at the single cell level (Chapters 4 and 5, Appendices B and C). The development and validation of genipin-modified PDMS substrates provides both extended culture of VSMCs on easily-characterized PDMS, as well as a method for maintaining patterned cell architecture. PDMS is also a useful substrate due to its hydrophobicity, allowing for isolation of water-soluble biochemical factors. Our use of traction force microscopy to capture the loss of VSMC function in the presence of Aβ provides further support for the amyloid hypothesis in Alzheimer's disease. In modeling the consequence of such loss of function in a thin-walled cerebral arterial model, we are able to posit that mechanical effects at the cellular level can yield the lost vasodilatory behavior observed in cerebral amyloid angiopathy [17]. These techniques and findings can be employed in a variety of future applications that both improve upon the current findings presented here and utilize the technologies developed for a variety of broader applications.

The key technique developed in this work, extended culture of patterned VSMCs on genipin-modified PDMS substrates, is admittedly narrow in scope at this point. An obvious future step in broadening the impact of this technique is to validate or extend it to other cell types and tissue models. Our work involved applying a technique proposed by Genchi et al. for culturing skeletal muscle cells on PDMS for up to one month [153]. Thus, skeletal muscle diseases may be a simple extension of the technique. Investigating mechano-adaptation in other chronic vascular diseases, such as hypertension, could be accomplished by

81

leveraging the elastic properties of PDMS to apply prescribed stretch to tissue mimics. Another intriguing application could involve probing the mechanics of tumor cells and metastasis over time on variable substrate stiffness or alternative extracellular matrix protein adsorption [225]. Modification of the microfluidic delivery device itself to apply a gradient of extracellular matrix could also expand the usefulness of genipin modification of PDMS.

During the course of the work described here, time limitations resulted in an abandonment of the initial motivation, namely, the synergy between mechanics and biochemical perturbations in the development of CVS after bTBI. Extending culture on PDMS substrates now allows for a comprehensive study of combinatorial effects of direct mechanical insult on genipin-modified MTFs and subsequent exposure to heighten levels of SAH-borne factors (similar to Chapter 4). Implementation of microfluidic patterning with the blast technique developed by Alford et al. [187] would allow extended observation of the phenotypic switching observed over the course of two days. Tissues may not maintain CVS mechanics over the typical disease progression of 3-7 days, which would suggest the importance of both blast forces and SAH factors in the severity of prolonged CVS. Further work to improve upon the cell viability of MTFs cultured within some form of isolation chamber, similar to that discussed in Appendix A, is necessary to properly investigate these likely synergistic effects. While our results were inconclusive at the single cell level regarding single SAH factor impacts on VSMC mechanics, the effects may prove dependent on cell-cell contacts that exist in the *in vivo* structure and that we successfully recapitulate in our MTF experimental model. Also, the key underlying mechanism by which SAH factors induce CVS mechanics may require combinatorial effects. A continued push toward high-throughput methods, such as microfluidic delivery of small volumes of factors is necessary to make such experiments feasible.

A key limitation of the TFM experiments discussed in Chapters 4 and 5 is that VSMCs do not exist as a sparse population in the arterial wall. While this model

could be considered a mimic for an injured vessel, most progressive vascular diseases involve maladaptation of an intact artery. Our muscular thin film technology [130, 226, 227] serves as a suitable model of the highly-aligned, confluent VSMC structure in the arterial media. Our findings of lost VSMC function when treated with Aβ would be well-served by analogous experimentation with the MTF construct. Assessment of differences in Aβ plaque formation and size may prove informative regarding the mechanism in which CAA develops within the vessel wall. Further, utilizing our genipin-modified MTFs, we can culture arterial lamellae mimics and determine the longer-term effects of Aβ on the structure of the monolayer of cells, in addition to the functional contractility. Han et al. found significant disruption of VSMC alignment and confluence in CAA-model arteries in mice [17]. If we can recapitulate this with our experimental system, we can draw yet another connection between VSMC structure and/or function and the accumulation of Aβ, providing a more complete picture of how Aβ contributes to Alzheimer's disease progression as a result of altered vascular tissue.

While our findings in Chapter 5 are significant, they would be greatly improved with a few more comprehensive studies moving forward. As referenced in the discussion of Chapter 5, our exclusive use of fibronectin as our cell adhesion extracellular matrix protein could bias VSMCs toward a synthetic phenotype [222]. This could also greatly influence the results discussed in Chapter 4 in our SAH-factor assay. Future work to probe the significance of our use of fibronectin is desirable and could greatly improve upon current findings. One simple, yet tedious, step would be to repeat the TFM experiments with alternative proteins, such as laminin, perlecan, or collagen, and determine any differences in results. Additionally, Western blotting for contractile phenotypic markers such as smooth muscle myosin heavy chain and smoothelin in conjunction with different concentrations of fibronectin could further elucidate the specific phenotypic effects inherent in our system. However, the sparse seeding may preclude this from being as viable. Another key limitation of our Aβ study involves the simplicity of the thin-

walled arterial model we developed. Given that temporal disease progression is the driving force for all the work contained in this dissertation, addition of temporal dynamics in the growth and remodeling response to lost VSMC function is of the utmost importance. One important consideration in this future implementation is how to account for and, perhaps more importantly, how to measure changes in the localized concentration of Aβ. Aβ aggregates are not consistent in size, so this is not a simple question to answer, as cells may sense higher concentrations of Aβ than those we prescribe experimentally.

References

[1] Y. Bhattacharjee, Shell shock revisited: solving the puzzle of blast trauma, Science (January) (2008) 406-408.

[2] B.V. Zlokovic, Neurovascular pathways to neurodegeneration in Alzheimer's disease and other disorders, Nat Rev Neurosci 12(12) (2011) 723-38.

[3] C. Iadecola, Neurovascular regulation in the normal brain and in Alzheimer's disease, Nat Rev Neurosci 5(5) (2004) 347-60.

[4] J. Holtz, U. Forstermann, U. Pohl, M. Giesler, E. Bassenge, Flow-dependent, endothelium-mediated dilation of epicardial coronary arteries in conscious dogs: effects of cyclooxygenase inhibition, J Cardiovasc Pharmacol 6(6) (1984) 1161-9.

[5] J.A.G. Rhodin, Architecture of the vessel wall, in: R. Berne (Ed.), Physiological reviews, American Physiology Society1979.

[6] Y.C. Fung, S.Q. Liu, Changes of zero-stress state of rat pulmonary arteries in hypoxic hypertension, J Appl Physiol 70(6) (1991) 2455-70.

[7] T. Matsumoto, K. Hayashi, Stress and strain distribution in hypertensive and normotensive rat aorta considering residual strain, J Biomech Eng 118(1) (1996) 62-73.

[8] E.K. Rodriguez, A. Hoger, A.D. McCulloch, Stress-dependent finite growth in soft elastic tissues, J Biomech 27(4) (1994) 455-67.

[9] P.W. Alford, J.D. Humphrey, L.A. Taber, Growth and remodeling in a thick-walled artery model: effects of spatial variations in wall constituents, Biomech Model Mechanobiol 7(4) (2008) 245-62.

[10] J.P. Stegemann, R.M. Nerem, Phenotype modulation in vascular tissue engineering using biochemical and mechanical stimulation, Ann Biomed Eng 31(4) (2003) 391-402.

[11] J.M. Mann, R.H. Lam, S. Weng, Y. Sun, J. Fu, A silicone-based stretchable micropost array membrane for monitoring live-cell subcellular cytoskeletal response, Lab Chip 12(4) (2012) 731-40.

[12] T.R. Polte, G.S. Eichler, N. Wang, D.E. Ingber, Extracellular matrix controls myosin light chain phosphorylation and cell contractility through modulation of cell shape and cytoskeletal prestress, Am J Physiol Cell Physiol 286(3) (2004) C518-28.

[13] T.M. Koch, S. Munster, N. Bonakdar, J.P. Butler, B. Fabry, 3D Traction forces in cancer cell invasion, PloS one 7(3) (2012) e33476.

[14] I.M. Tolić-Nørrelykke, J.P. Butler, J. Chen, N. Wang, Spatial and temporal traction response in human airway smooth muscle cells, Am J Physiol Cell Physiol 283(4) (2002) C1254-66.

[15] P.W. Alford, A.W. Feinberg, S.P. Sheehy, K.K. Parker, Biohybrid thin films for measuring contractility in engineered cardiovascular muscle, Biomaterials 31(13) (2010) 3613-21.

[16] K.A. Jellinger, Prevalence and impact of cerebrovascular lesions in Alzheimer and lewy body diseases, Neurodegener Dis 7(1-3) (2010) 112-5.

[17] B.H. Han, M.L. Zhou, F. Abousaleh, R.P. Brendza, H.H. Dietrich, J. Koenigsknecht-Talboo, J.R. Cirrito, E. Milner, D.M. Holtzman, G.J. Zipfel, Cerebrovascular dysfunction in amyloid precursor protein transgenic mice: contribution of soluble and insoluble

amyloid-beta peptide, partial restoration via gamma-secretase inhibition, J Neurosci 28(50) (2008) 13542-50.

[18] E.S. Hald, P.W. Alford, Smooth muscle phenotype switching in blast traumatic brain injury-induced cerebral vasospasm, Transl Stroke Res 5(3) (2014) 385-93.

[19] M.D. Faul, Wald M.M., Xu, L., and Coronado, V.G., Traumatic brain injury in the United States: emergency department visits, hospitalizations, and deaths, 2002-2006, Centers for Disease Control and Prevention, National Center for Injury Prevention and Control, Atlanta, GA, 2010.

[20] R.A. Armonda, R.S. Bell, A.H. Vo, G. Ling, T.J. DeGraba, B. Crandall, J. Ecklund, W.W. Campbell, Wartime traumatic cerebral vasospasm: recent review of combat casualties, Neurosurgery 59(6) (2006) 1215-25; discussion 1225.

[21] L.E. Goldstein, a.M. Fisher, C.a. Tagge, X.L. Zhang, L. Velisek, J.a. Sullivan, C. Upreti, J.M. Kracht, M. Ericsson, M.W. Wojnarowicz, C.J. Goletiani, G.M. Maglakelidze, N. Casey, J.a. Moncaster, O. Minaeva, R.D. Moir, C.J. Nowinski, R.a. Stern, R.C. Cantu, J. Geiling, J.K. Blusztajn, B.L. Wolozin, T. Ikezu, T.D. Stein, a.E. Budson, N.W. Kowall, D. Chargin, a. Sharon, S. Saman, G.F. Hall, W.C. Moss, R.O. Cleveland, R.E. Tanzi, P.K. Stanton, a.C. McKee, Chronic Traumatic Encephalopathy in Blast-Exposed Military Veterans and a Blast Neurotrauma Mouse Model, Science Translational Medicine 4(134) (2012) 134ra60-134ra60.

[22] R.a. Armonda, R.S. Bell, A.H. Vo, G. Ling, T.J. DeGraba, B. Crandall, J. Ecklund, W.W. Campbell, Wartime traumatic cerebral vasospasm: recent review of combat casualties, Neurosurgery 59(6) (2006) 1215-25; discussion 1225.

[23] G. Ling, F. Bandak, R. Armonda, G. Grant, J. Ecklund, Explosive blast neurotrauma, Journal of neurotrauma 26(6) (2009) 815-25.

[24] C.O. Borel, Possible Role for Vascular Cell Proliferation in Cerebral Vasospasm After Subarachnoid Hemorrhage * Editorial Comment, Stroke 34(2) (2003) 427-433.

[25] Z.D. Zhang, R.L. Macdonald, Contribution of the remodeling response to cerebral vasospasm, Neurological research 28(7) (2006) 713-20.

[26] J.D. Humphrey, S. Baek, Biochemomechanics of cerebral vasospasm and its resolution: I. A new hypothesis and theoretical framework, Annals of biomedical engineering 35(9) (2007) 1485-1497.

[27] P.W. Alford, B.E. Dabiri, J.a. Goss, M.a. Hemphill, M.D. Brigham, K.K. Parker, Blast-induced phenotypic switching in cerebral vasospasm, Proceedings of the National Academy of Sciences of the United States of America 108(31) (2011) 12705-10.

[28] A.C. Courtney, M.W. Courtney, A thoracic mechanism of mild traumatic brain injury due to blast pressure waves, Medical hypotheses 72(1) (2009) 76-83.

[29] J.B. Long, T.L. Bentley, K.A. Wessner, C. Cerone, S. Sweeney, R.A. Bauman, Blast overpressure in rats: recreating a battlefield injury in the laboratory, Journal of neurotrauma 26(6) (2009) 827-40.

[30] R.A. Bauman, G. Ling, L. Tong, A. Januszkiewicz, D. Agoston, N. Delanerolle, Y. Kim, D. Ritzel, R. Bell, J. Ecklund, R. Armonda, F. Bandak, S. Parks, An introductory characterization of a combat-casualty-care relevant swine model of closed head injury resulting from exposure to explosive blast, Journal of neurotrauma 26(6) (2009) 841-60.

[31] B.V. Zlokovic, Neurovascular pathways to neurodegeneration in Alzheimer's disease and other disorders, Nature reviews. Neuroscience 12(12) (2011) 723-38.

[32] D.M. Geddes, R.S. Cargill, 2nd, M.C. LaPlaca, Mechanical stretch to neurons results in a strain rate and magnitude-dependent increase in plasma membrane permeability, Journal of neurotrauma 20(10) (2003) 1039-49.

[33] D. Kilinc, G. Gallo, K.A. Barbee, Mechanically-induced membrane poration causes axonal beading and localized cytoskeletal damage, Experimental neurology 212(2) (2008) 422-30.

[34] E.H. Pettus, C.W. Christman, M.L. Giebel, J.T. Povlishock, Traumatically induced altered membrane permeability: its relationship to traumatically induced reactive axonal change, Journal of neurotrauma 11(5) (1994) 507-22.

[35] M.A. Hemphill, B.E. Dabiri, S. Gabriele, L. Kerscher, C. Franck, J.A. Goss, P.W. Alford, K.K. Parker, A possible role for integrin signaling in diffuse axonal injury, PloS one 6(7) (2011) e22899.

[36] S. Yeoh, E.D. Bell, K.L. Monson, Distribution of Blood-Brain Barrier Disruption in Primary Blast Injury, Ann Biomed Eng (2013).

[37] Y. Chen, W. Huang, S. Constantini, Blast shock wave mitigation using the hydraulic energy redirection and release technology, PloS one 7(6) (2012) e39353.

[38] R. Kuehn, P.F. Simard, I. Driscoll, K. Keledjian, S. Ivanova, C. Tosun, A. Williams, G. Bochicchio, V. Gerzanich, J.M. Simard, Rodent model of direct cranial blast injury, Journal of neurotrauma 28(10) (2011) 2155-69.

[39] R.H. Garman, L.W. Jenkins, R.C. Switzer, 3rd, R.A. Bauman, L.C. Tong, P.V. Swauger, S.A. Parks, D.V. Ritzel, C.E. Dixon, R.S. Clark, H. Bayir, V. Kagan, E.K. Jackson, P.M. Kochanek, Blast exposure in rats with body shielding is characterized primarily by diffuse axonal injury, Journal of neurotrauma 28(6) (2011) 947-59.

[40] R.D. Readnower, M. Chavko, S. Adeeb, M.D. Conroy, J.R. Pauly, R.M. McCarron, P.G. Sullivan, Increase in blood-brain barrier permeability, oxidative stress, and activated microglia in a rat model of blast-induced traumatic brain injury, Journal of neuroscience research 88(16) (2010) 3530-9.

[41] C.D. Hue, S. Cao, S.F. Haider, K.V. Vo, G.B. Effgen, E. Vogel, 3rd, M.B. Panzer, C.R. Bass, D.F. Meaney, B. Morrison, 3rd, Blood-Brain Barrier Dysfunction after Primary Blast Injury in vitro, Journal of neurotrauma 30(19) (2013) 1652-1663.

[42] K. Murakami, M. Koide, T.M. Dumont, S.R. Russell, B.I. Tranmer, G.C. Wellman, Subarachnoid Hemorrhage Induces Gliosis and Increased Expression of the Pro-inflammatory Cytokine High Mobility Group Box 1 Protein, Transl Stroke Res 2(1) (2011) 72-79.

[43] P. Harrison, E.M. Cramer, Platelet alpha-granules, Blood reviews 7(1) (1993) 52-62.

[44] D. Keilin, Hartree, E.F., Reaction of nitric oxide with haemoglobin and methaemoglobin, Nature 139 (1937) 548.

[45] J. Gow, Stamler, J., Reactions between nitric oxide and haemoglobin under physiological conditions, Nature 391 (1998) 169-173.

[46] M.T. Gladwin, J.R. Lancaster, Jr., B.A. Freeman, A.N. Schechter, Nitric oxide's reactions with hemoglobin: a view through the SNO-storm, Nat Med 9(5) (2003) 496-500.

[47] H. Shimokawa, A. Ito, Y. Fukumoto, T. Kadokami, R. Nakaike, M. Sakata, T. Takayanagi, K. Egashira, A. Takeshita, Chronic treatment with interleukin-1 beta induces coronary intimal lesions and vasospastic responses in pigs in vivo. The role of platelet-derived growth factor, The Journal of clinical investigation 97(3) (1996) 769-76.

[48] H.H. Dietrich, R.G. Dacey, Jr., Molecular keys to the problems of cerebral vasospasm, Neurosurgery 46(3) (2000) 517-30.

[49] A.S. Dumont, R.J. Dumont, M.M. Chow, C.L. Lin, T. Calisaneller, K.F. Ley, N.F. Kassell, K.S. Lee, Cerebral vasospasm after subarachnoid hemorrhage: putative role of inflammation, Neurosurgery 53(1) (2003) 123-33; discussion 133-5.

[50] G. Grasso, An overview of new pharmacological treatments for cerebrovascular dysfunction after experimental subarachnoid hemorrhage, Brain research. Brain research reviews 44(1) (2004) 49-63.

[51] W.F. Boron, Boulpaep E.L., Medical Physiology: A Cellular and Molecular Approach, 1st ed., W.B. Saunders, USA, 2003.

[52] R. Balabanov, H. Goldman, S. Murphy, G. Pellizon, C. Owen, J. Rafols, P. Dore-Duffy, Endothelial cell activation following moderate traumatic brain injury, Neurological research 23(2-3) (2001) 175-82.

[53] B.R. Clower, Y. Yamamoto, L. Cain, D.E. Haines, R.R. Smith, Endothelial injury following experimental subarachnoid hemorrhage in rats: effects on brain blood flow, The Anatomical record 240(1) (1994) 104-14.

[54] F. Bohm, J. Pernow, The importance of endothelin-1 for vascular dysfunction in cardiovascular disease, Cardiovascular research 76(1) (2007) 8-18.

[55] M. Zimmermann, V. Seifert, Endothelin and subarachnoid hemorrhage: an overview, Neurosurgery 43(4) (1998) 863-75; discussion 875-6.

[56] H. Vatter, J. Konczalla, V. Seifert, Endothelin related pathophysiology in cerebral vasospasm: what happens to the cerebral vessels?, Acta neurochirurgica. Supplement 110(Pt 1) (2011) 177-80.

[57] G.K. Owens, Regulation of differentiation of vascular smooth muscle cells, Physiological reviews 75(3) (1995) 487-517.

[58] V.P. Iyemere, D. Proudfoot, P.L. Weissberg, C.M. Shanahan, Vascular smooth muscle cell phenotypic plasticity and the regulation of vascular calcification, Journal of internal medicine 260(3) (2006) 192-210.

[59] M.R. Alexander, G.K. Owens, Epigenetic control of smooth muscle cell differentiation and phenotypic switching in vascular development and disease, Annual review of physiology 74 (2012) 13-40.

[60] J.P. Stegemann, H. Hong, R.M. Nerem, Mechanical, biochemical, and extracellular matrix effects on vascular smooth muscle cell phenotype, J Appl Physiol 98(6) (2005) 2321-7.

[61] N.C. Chesler, D.N. Ku, Z.S. Galis, Transmural pressure induces matrix-degrading activity in porcine arteries ex vivo, The American journal of physiology 277(5 Pt 2) (1999) H2002-9.

[62] J.M. Zabramski, Vasospasm after Subarachnoid Hemorrhage, in: J.B. Bederson (Ed.), Subarachnoid Hemorrhage: Pathophysiology and Management, The American Association of Neurological Surgeons1997, pp. 127-156.

[63] R.L. Macdonald, Pathophysiology and molecular genetics of vasospasm, Acta neurochirurgica. Supplement 77 (2001) 7-11.

[64] M.R. Mayberg, T. Okada, D.H. Bark, The significance of morphological changes in cerebral arteries after subarachnoid hemorrhage, Journal of neurosurgery 72(4) (1990) 626-33.

[65] M.J. McGirt, J.R. Lynch, R. Blessing, D.S. Warner, A.H. Friedman, D.T. Laskowitz, Serum von Willebrand factor, matrix metalloproteinase-9, and vascular endothelial growth factor levels predict the onset of cerebral vasospasm after aneurysmal subarachnoid hemorrhage, Neurosurgery 51(5) (2002) 1128-34; discussion 1134-5.

[66] R.M. Pluta, Delayed cerebral vasospasm and nitric oxide: review, new hypothesis, and proposed treatment, Pharmacology & therapeutics 105(1) (2005) 23-56.

[67] B. Zhang, K. Fugleholm, L.B. Day, S. Ye, R.O. Weller, I.N. Day, Molecular pathogenesis of subarachnoid haemorrhage, The international journal of biochemistry & cell biology 35(9) (2003) 1341-60.

[68] S.Q. Liu, Y.C. Fung, Zero-stress states of arteries, J Biomech Eng 110(1) (1988) 82-4.

[69] R. Armentano, A. Simon, J. Levenson, N.P. Chau, J.L. Megnien, R. Pichel, Mechanical pressure versus intrinsic effects of hypertension on large arteries in humans, Hypertension 18(5) (1991) 657-64.

[70] H.D. Intengan, E.L. Schiffrin, Vascular remodeling in hypertension: roles of apoptosis, inflammation, and fibrosis, Hypertension 38(3 Pt 2) (2001) 581-7.

[71] Y.C. Fung, S.Q. Liu, Change of residual strains in arteries due to hypertrophy caused by aortic constriction, Circ Res 65(5) (1989) 1340-9.

[72] P.W. Alford, J.D. Humphrey, L.a. Taber, Growth and remodeling in a thick-walled artery model: effects of spatial variations in wall constituents, Biomechanics and modeling in mechanobiology 7(4) (2008) 245-62.

[73] P.W. Alford, L.A. Taber, Computational study of growth and remodelling in the aortic arch, Comput Methods Biomech Biomed Engin 11(5) (2008) 525-38.

[74] G.K. Owens, M.S. Kumar, B.R. Wamhoff, Molecular regulation of vascular smooth muscle cell differentiation in development and disease, Physiol Rev 84(3) (2004) 767-801.

[75] K. Kawai-Kowase, G.K. Owens, Multiple repressor pathways contribute to phenotypic switching of vascular smooth muscle cells, American journal of physiology. Cell physiology 292(1) (2007) C59-69.

[76] N. Chow, R.D. Bell, R. Deane, J.W. Streb, J. Chen, A. Brooks, W. Van Nostrand, J.M. Miano, B.V. Zlokovic, Serum response factor and myocardin mediate arterial

hypercontractility and cerebral blood flow dysregulation in Alzheimer's phenotype, Proc Natl Acad Sci U S A 104(3) (2007) 823-8.

[77] S. Li, J. Lao, B.P. Chen, Y.S. Li, Y. Zhao, J. Chu, K.D. Chen, T.C. Tsou, K. Peck, S. Chien, Genomic analysis of smooth muscle cells in 3-dimensional collagen matrix, FASEB journal : official publication of the Federation of American Societies for Experimental Biology 17(1) (2003) 97-9.

[78] P.C. Schulze, G.W. de Keulenaer, K.A. Kassik, T. Takahashi, Z. Chen, D.I. Simon, R.T. Lee, Biomechanically induced gene iex-1 inhibits vascular smooth muscle cell proliferation and neointima formation, Circ Res 93(12) (2003) 1210-7.

[79] G.B. Chapman, W. Durante, J.D. Hellums, A.I. Schafer, Physiological cyclic stretch causes cell cycle arrest in cultured vascular smooth muscle cells, American journal of physiology. Heart and circulatory physiology 278(3) (2000) H748-54.

[80] B.S. Kim, J. Nikolovski, J. Bonadio, D.J. Mooney, Cyclic mechanical strain regulates the development of engineered smooth muscle tissue, Nature biotechnology 17(10) (1999) 979-83.

[81] B. Williams, Mechanical influences on vascular smooth muscle cell function, Journal of hypertension 16(12 Pt 2) (1998) 1921-9.

[82] D.P. McDaniel, G.A. Shaw, J.T. Elliott, K. Bhadriraju, C. Meuse, K.H. Chung, A.L. Plant, The stiffness of collagen fibrils influences vascular smooth muscle cell phenotype, Biophysical journal 92(5) (2007) 1759-69.

[83] O.V. Sazonova, K.L. Lee, B.C. Isenberg, C.B. Rich, M.A. Nugent, J.Y. Wong, Cell-cell interactions mediate the response of vascular smooth muscle cells to substrate stiffness, Biophysical journal 101(3) (2011) 622-30.

[84] P.W. Alford, A.P. Nesmith, J.N. Seywerd, A. Grosberg, K.K. Parker, Vascular smooth muscle contractility depends on cell shape, Integr Biol (Camb) 3(11) (2011) 1063-70.

[85] S.R. Peyton, A.J. Putnam, Extracellular matrix rigidity governs smooth muscle cell motility in a biphasic fashion, Journal of cellular physiology 204(1) (2005) 198-209.

[86] B.E. Masel, R.S. Bell, S. Brossart, R.J. Grill, R.L. Hayes, H.S. Levin, M.N. Rasband, D.V. Ritzel, C.E. Wade, D.S. DeWitt, Galveston Brain Injury Conference 2010: clinical and experimental aspects of blast injury, Journal of neurotrauma 29(12) (2012) 2143-71.

[87] D.S. DeWitt, D.S. Prough, Blast-induced brain injury and posttraumatic hypotension and hypoxemia, Journal of neurotrauma 26(6) (2009) 877-87.

[88] G. Liu, H. Wang, D. Ou, H. Huang, D. Liao, Endothelin-1, an important mitogen of smooth muscle cells of spontaneously hypertensive rats, Chinese medical journal 115(5) (2002) 750-2.

[89] R.C. Chambers, P. Leoni, N. Kaminski, G.J. Laurent, R.A. Heller, Global expression profiling of fibroblast responses to transforming growth factor-beta1 reveals the induction of inhibitor of differentiation-1 and provides evidence of smooth muscle cell phenotypic switching, Am J Pathol 162(2) (2003) 533-46.

[90] M.K. Jain, K.P. Fujita, C.M. Hsieh, W.O. Endege, N.E. Sibinga, S.F. Yet, S. Kashiki, W.S. Lee, M.A. Perrella, E. Haber, M.E. Lee, Molecular cloning and

characterization of SmLIM, a developmentally regulated LIM protein preferentially expressed in aortic smooth muscle cells, The Journal of biological chemistry 271(17) (1996) 10194-9.

[91] D.W. Lin, I.C. Chang, A. Tseng, M.L. Wu, C.H. Chen, C.A. Patenaude, M.D. Layne, S.F. Yet, Transforming growth factor beta up-regulates cysteine-rich protein 2 in vascular smooth muscle cells via activating transcription factor 2, The Journal of biological chemistry 283(22) (2008) 15003-14.

[92] Y.C. Wu, L. Cui, G. Li, S. Yin, Y.J. Gao, Y.L. Cao, [PDGF-BB initiates vascular smooth muscle-like phenotype differentiation of human bone marrow mesenchymal stem cells in vitro], Zhonghua zheng xing wai ke za zhi = Zhonghua zhengxing waike zazhi = Chinese journal of plastic surgery 23(4) (2007) 335-9.

[93] B.J. Holycross, R.S. Blank, M.M. Thompson, M.J. Peach, G.K. Owens, Platelet-derived growth factor-BB-induced suppression of smooth muscle cell differentiation, Circ Res 71(6) (1992) 1525-32.

[94] X. Li, V. Van Putten, F. Zarinetchi, M.E. Nicks, S. Thaler, L.E. Heasley, R.A. Nemenoff, Suppression of smooth-muscle alpha-actin expression by platelet-derived growth factor in vascular smooth-muscle cells involves Ras and cytosolic phospholipase A2, The Biochemical journal 327 (Pt 3) (1997) 709-16.

[95] K. Lehti, N.F. Rose, S. Valavaara, S.J. Weiss, J. Keski-Oja, MT1-MMP promotes vascular smooth muscle dedifferentiation through LRP1 processing, Journal of cell science 122(Pt 1) (2009) 126-35.

[96] J.N. Song, W.T. Yan, J.Y. An, G.S. Hao, X.Y. Guo, M. Zhang, Y. Li, D.D. Li, P. Sun, Potential contribution of SOCC to cerebral vasospasm after experimental subarachnoid hemorrhage in rats, Brain research 1517 (2013) 93-103.

[97] R. Berra-Romani, A. Mazzocco-Spezzia, M.V. Pulina, V.A. Golovina, Ca2+ handling is altered when arterial myocytes progress from a contractile to a proliferative phenotype in culture, American journal of physiology. Cell physiology 295(3) (2008) C779-90.

[98] S.J. House, M. Potier, J. Bisaillon, H.A. Singer, M. Trebak, The non-excitable smooth muscle: calcium signaling and phenotypic switching during vascular disease, Pflugers Archiv : European journal of physiology 456(5) (2008) 769-85.

[99] M.C. Hubbell, A.J. Semotiuk, R.B. Thorpe, O.O. Adeoye, S.M. Butler, J.M. Williams, O. Khorram, W.J. Pearce, Chronic hypoxia and VEGF differentially modulate abundance and organization of myosin heavy chain isoforms in fetal and adult ovine arteries, American journal of physiology. Cell physiology 303(10) (2012) C1090-103.

[100] O.O. Adeoye, S.M. Butler, M.C. Hubbell, A. Semotiuk, J.M. Williams, W.J. Pearce, Contribution of increased VEGF receptors to hypoxic changes in fetal ovine carotid artery contractile proteins, American journal of physiology. Cell physiology 304(7) (2013) C656-65.

[101] R.L. MacDonald, Weir, B., Cerebral Vasospasm, Academic Press2001.

[102] T. Sugawara, R. Ayer, V. Jadhav, W. Chen, T. Tsubokawa, J.H. Zhang, Mechanisms of statin treatment in cerebral vasospasm, Acta neurochirurgica. Supplement 110(Pt 2) (2011) 9-11.

[103] S. Satoh, M. Takayasu, K. Kawasaki, I. Ikegaki, A. Hitomi, K. Yano, M. Shibuya, T. Asano, Antivasospastic effects of hydroxyfasudil, a Rho-kinase inhibitor, after subarachnoid hemorrhage, Journal of pharmacological sciences 118(1) (2012) 92-8.
[104] M. Naraoka, A. Munakata, N. Matsuda, N. Shimamura, H. Ohkuma, Suppression of the Rho/Rho-Kinase Pathway and Prevention of Cerebral Vasospasm by Combination Treatment with Statin and Fasudil After Subarachnoid Hemorrhage in Rabbit, Transl Stroke Res 4(3) (2013) 368-374.
[105] F. Amenta, A. Lanari, F. Mignini, G. Silvestrelli, E. Traini, D. Tomassoni, Nicardipine use in cerebrovascular disease: a review of controlled clinical studies, Journal of the neurological sciences 283(1-2) (2009) 219-23.
[106] D. Inzitari, A. Poggesi, Calcium channel blockers and stroke, Aging clinical and experimental research 17(4 Suppl) (2005) 16-30.
[107] R.G. Mesis, H. Wang, F.W. Lombard, R. Yates, M.P. Vitek, C.O. Borel, D.S. Warner, D.T. Laskowitz, Dissociation between vasospasm and functional improvement in a murine model of subarachnoid hemorrhage, Neurosurgical focus 21(3) (2006) E4.
[108] Z. Zhang, Mondello, S., Kobeissy, F., Rubenstein, R., Streeter, J., Hayes, R. L., & Wang, K. K., Protein Biomarkers for Traumatic and Ischemic Brain Injury: From Bench to Bedside, Translational Stroke Research 2 (2011) 455-462.
[109] S.H. North, L.C. Shriver-Lake, C.R. Taitt, F.S. Ligler, Rapid analytical methods for on-site triage for traumatic brain injury, Annu Rev Anal Chem (Palo Alto Calif) 5 (2012) 35-56.
[110] T. Ogawa, D. Hanggi, Y. Wu, H. Michiue, K. Tomizawa, S. Ono, H. Matsui, I. Date, H.J. Steiger, Protein therapy using heme-oxygenase-1 fused to a polyarginine transduction domain attenuates cerebral vasospasm after experimental subarachnoid hemorrhage, Journal of cerebral blood flow and metabolism : official journal of the International Society of Cerebral Blood Flow and Metabolism 31(11) (2011) 2231-42.
[111] Z. Ram, M. Sadeh, I. Shacked, A. Sahar, M. Hadani, Magnesium sulfate reverses experimental delayed cerebral vasospasm after subarachnoid hemorrhage in rats, Stroke 22(7) (1991) 922-7.
[112] B. Huang, N.H. Khatibi, L. Tong, P. Yan, P. Xie, J.H. Zhang, Magnesium Sulfate Treatment Improves Outcome in Patients with Subarachnoid Hemorrhage: A Meta-Analysis Study, Transl Stroke Res 1(2) (2010) 108-112.
[113] R.L. MacDonald, Kakarieka, A., Mayer, S.A., Pasqualin, A., Ruefenacht, D., Schmiedek, P., Kassell, N.F., Prevention of Cerebral Vasospasm after Aneurysmal Subarachnoid Hemorrhage with Clazosentan, an Endothelin Receptor Antagonist, Neurosurgery 59(2) (2006) 453.
[114] R.L. Macdonald, Clazosentan: an endothelin receptor antagonist for treatment of vasospasm after subarachnoid hemorrhage, Expert opinion on investigational drugs 17(11) (2008) 1761-7.
[115] R.L. Macdonald, R.T. Higashida, E. Keller, S.A. Mayer, A. Molyneux, A. Raabe, P. Vajkoczy, I. Wanke, D. Bach, A. Frey, A. Marr, S. Roux, N. Kassell, Clazosentan, an endothelin receptor antagonist, in patients with aneurysmal subarachnoid haemorrhage

undergoing surgical clipping: a randomised, double-blind, placebo-controlled phase 3 trial (CONSCIOUS-2), Lancet neurology 10(7) (2011) 618-25.

[116] R.L. Macdonald, R.T. Higashida, E. Keller, S.A. Mayer, A. Molyneux, A. Raabe, P. Vajkoczy, I. Wanke, D. Bach, A. Frey, P. Nowbakht, S. Roux, N. Kassell, Randomized trial of clazosentan in patients with aneurysmal subarachnoid hemorrhage undergoing endovascular coiling, Stroke 43(6) (2012) 1463-9.

[117] M. Yamaguchi-Okada, S. Nishizawa, A. Mizutani, H. Namba, Multifaceted effects of selective inhibitor of phosphodiesterase III, cilostazol, for cerebral vasospasm after subarachnoid hemorrhage in a dog model, Cerebrovasc Dis 28(2) (2009) 135-42.

[118] R.P. Ostrowski, J.H. Zhang, Hyperbaric Oxygen for Cerebral Vasospasm and Brain Injury Following Subarachnoid Hemorrhage, Transl Stroke Res 2(3) (2011) 316-327.

[119] Y. Soejima, Q. Hu, P.R. Krafft, M. Fujii, J. Tang, J.H. Zhang, Hyperbaric oxygen preconditioning attenuates hyperglycemia-enhanced hemorrhagic transformation by inhibiting matrix metalloproteinases in focal cerebral ischemia in rats, Experimental neurology (2013).

[120] K.L. Monson, M.M. Matsumoto, W.L. Young, G.T. Manley, T. Hashimoto, Abrupt increase in rat carotid blood flow induces rapid alteration of artery mechanical properties, Journal of the mechanical behavior of biomedical materials 4(1) (2011) 9-15.

[121] Z.S. Jackson, A.I. Gotlieb, B.L. Langille, Wall tissue remodeling regulates longitudinal tension in arteries, Circ Res 90(8) (2002) 918-25.

[122] N. Etminan, M.D. Vergouwen, D. Ilodigwe, R.L. Macdonald, Effect of pharmaceutical treatment on vasospasm, delayed cerebral ischemia, and clinical outcome in patients with aneurysmal subarachnoid hemorrhage: a systematic review and meta-analysis, Journal of cerebral blood flow and metabolism : official journal of the International Society of Cerebral Blood Flow and Metabolism 31(6) (2011) 1443-51.

[123] J.P. Dreier, S. Major, A. Manning, J. Woitzik, C. Drenckhahn, J. Steinbrink, C. Tolias, A.I. Oliveira-Ferreira, M. Fabricius, J.A. Hartings, P. Vajkoczy, M. Lauritzen, U. Dirnagl, G. Bohner, A.J. Strong, Cortical spreading ischaemia is a novel process involved in ischaemic damage in patients with aneurysmal subarachnoid haemorrhage, Brain : a journal of neurology 132(Pt 7) (2009) 1866-81.

[124] M.D. Vergouwen, N. Etminan, D. Ilodigwe, R.L. Macdonald, Lower incidence of cerebral infarction correlates with improved functional outcome after aneurysmal subarachnoid hemorrhage, Journal of cerebral blood flow and metabolism : official journal of the International Society of Cerebral Blood Flow and Metabolism 31(7) (2011) 1545-53.

[125] M.D. Vergouwen, D. Ilodigwe, R.L. Macdonald, Cerebral infarction after subarachnoid hemorrhage contributes to poor outcome by vasospasm-dependent and -independent effects, Stroke 42(4) (2011) 924-9.

[126] I. Cernak, Savic, J., Malicevic, Z., Zunic, G., Djurdjevic, D., and Prokic, V. , The pathogenesis of pulmonary blast injury: our point of view, Chinese J Traumatol 12 (1996) 28-31.

[127] I. Cernak, Malicevik, Z., Prokic, V., Zunic, G., Djurdjevic, D., Ilic, S., and Savic, J., Indirect neurotrauma caused by pulmonary blast injury: Development and pronosis., Int Rev Armed Forces Med Services 52 (1997) 114-20.

[128] I. Cernak, Z. Wang, J. Jiang, X. Bian, J. Savic, Ultrastructural and functional characteristics of blast injury-induced neurotrauma, The Journal of trauma 50(4) (2001) 695-706.

[129] I. Cernak, D. Ignjatovic, G. Andelic, J. Savic, [Metabolic changes as part of the general response of the body to the effect of blast waves], Vojnosanitetski pregled. Military-medical and pharmaceutical review 48(6) (1991) 515-22.

[130] E.S. Hald, K.E. Steucke, J.A. Reeves, Z. Win, P.W. Alford, Long-term vascular contractility assay using genipin-modified muscular thin films, Biofabrication 6(4) (2014) 045005.

[131] Global Status Report on Noncommunicable Diseases 2010, World Health Organization, Geneva, Switzerland, 2011, pp. 1-162.

[132] J.D. Humphrey, S. Baek, L.E. Niklason, Biochemomechanics of cerebral vasospasm and its resolution: I. A new hypothesis and theoretical framework, Annals of biomedical engineering 35(9) (2007) 1485-1497.

[133] B. Weir, M. Grace, J. Hansen, C. Rothberg, Time course of vasospasm in man, Journal of neurosurgery 48(2) (1978) 173-8.

[134] A.J. Lusis, Atherosclerosis, Nature 407(6801) (2000) 233-41.

[135] K.N. Kayembe, M. Sasahara, F. Hazama, Cerebral aneurysms and variations in the circle of Willis, Stroke 15(5) (1984) 846-50.

[136] D. Huh, Y.S. Torisawa, G.A. Hamilton, H.J. Kim, D.E. Ingber, Microengineered physiological biomimicry: organs-on-chips, Lab on a chip 12(12) (2012) 2156-64.

[137] A.D. van der Meer, A. van den Berg, Organs-on-chips: breaking the in vitro impasse, Integr Biol (Camb) 4(5) (2012) 461-70.

[138] Y. Nakao, H. Kimura, Y. Sakai, T. Fujii, Bile canaliculi formation by aligning rat primary hepatocytes in a microfluidic device, Biomicrofluidics 5(2) (2011) 22212.

[139] K.J. Jang, K.Y. Suh, A multi-layer microfluidic device for efficient culture and analysis of renal tubular cells, Lab on a chip 10(1) (2010) 36-42.

[140] D. Huh, B.D. Matthews, A. Mammoto, M. Montoya-Zavala, H.Y. Hsin, D.E. Ingber, Reconstituting organ-level lung functions on a chip, Science (New York, N.Y.) 328(5986) (2010) 1662-8.

[141] A. Agarwal, J.A. Goss, A. Cho, M.L. McCain, K.K. Parker, Microfluidic heart on a chip for higher throughput pharmacological studies, Lab on a chip 13(18) (2013) 3599-608.

[142] A.D. van der Meer, A.A. Poot, J. Feijen, I. Vermes, Analyzing shear stress-induced alignment of actin filaments in endothelial cells with a microfluidic assay, Biomicrofluidics 4(1) (2010) 11103.

[143] A. Gunther, S. Yasotharan, A. Vagaon, C. Lochovsky, S. Pinto, J. Yang, C. Lau, J. Voigtlaender-Bolz, S.S. Bolz, A microfluidic platform for probing small artery structure and function, Lab on a chip 10(18) (2010) 2341-9.

[144] C.S. Chen, M. Mrksich, S. Huang, G.M. Whitesides, D.E. Ingber, Geometric control of cell life and death, Science 276(5317) (1997) 1425-8.

[145] P.W. Alford, B.E. Dabiri, J.A. Goss, M.A. Hemphill, M.D. Brigham, K.K. Parker, Blast-induced phenotypic switching in cerebral vasospasm, Proceedings of the National Academy of Sciences of the United States of America 108(31) (2011) 12705-10.

[146] K. Balachandran, P.W. Alford, J. Wylie-Sears, J.A. Goss, A. Grosberg, J. Bischoff, E. Aikawa, R.A. Levine, K.K. Parker, Cyclic strain induces dual-mode endothelial-mesenchymal transformation of the cardiac valve, Proc Natl Acad Sci U S A 108(50) (2011) 19943-8.

[147] A. Tóth, I. Bertóti, M. Blazsó, G. Bánhegyi, A. Bognar, P. Szaplonczay, Oxidative damage and recovery of silicone rubber surfaces. I. X-ray photoelectron spectroscopic study, Journal of applied polymer science 52(9) (1994) 1293-1307.

[148] A. Khademhosseini, Micro and Nanoengineering of the Cell Microenvironment: Technologies and Applications, Artech House2008.

[149] C.C. Wu, C.Y. Yuan, S.J. Ding, Effect of polydimethylsiloxane surfaces silanized with different nitrogen-containing groups on the adhesion progress of epithelial cells., Surface & coatings technology 205(10) (2011) 3182-3189.

[150] J.P. Dunkers, H.J. Lee, M.A. Matos, L.M. Pakstis, J.M. Taboas, S.D. Hudson, M.T. Cicerone, Effect of surface modification on protein retention and cell proliferation under strain, Acta Biomater 7(7) (2011) 2902-9.

[151] P.J. Wipff, H. Majd, C. Acharya, L. Buscemi, J.J. Meister, B. Hinz, The covalent attachment of adhesion molecules to silicone membranes for cell stretching applications, Biomaterials 30(9) (2009) 1781-9.

[152] J. Zhou, A.V. Ellis, N.H. Voelcker, Recent developments in PDMS surface modification for microfluidic devices, Electrophoresis 31(1) (2010) 2-16.

[153] G.G. Genchi, G. Ciofani, I. Liakos, L. Ricotti, L. Ceseracciu, A. Athanassiou, B. Mazzolai, A. Menciassi, V. Mattoli, Bio/non-bio interfaces: a straightforward method for obtaining long term PDMS/muscle cell biohybrid constructs, Colloids Surf B Biointerfaces 105 (2013) 144-51.

[154] G. Fessel, J. Cadby, S. Wunderli, R. van Weeren, J.G. Snedeker, Dose- and time-dependent effects of genipin crosslinking on cell viability and tissue mechanics - Toward clinical application for tendon repair, Acta Biomater (2013).

[155] H.W. Sung, R.N. Huang, L.L. Huang, C.C. Tsai, C.T. Chiu, Feasibility study of a natural crosslinking reagent for biological tissue fixation, Journal of biomedical materials research 42(4) (1998) 560-7.

[156] E.G. Lima, A.R. Tan, T. Tai, K.G. Marra, A. DeFail, G.A. Ateshian, C.T. Hung, Genipin enhances the mechanical properties of tissue-engineered cartilage and protects against inflammatory degradation when used as a medium supplement, Journal of biomedical materials research. Part A 91(3) (2009) 692-700.

[157] K. Madhavan, D. Belchenko, W. Tan, Roles of genipin crosslinking and biomolecule conditioning in collagen-based biopolymer: Potential for vascular media regeneration, Journal of biomedical materials research. Part A (2011).

[158] A. Satyam, G.S. Subramanian, M. Raghunath, A. Pandit, D.I. Zeugolis, In vitro evaluation of Ficoll-enriched and genipin-stabilised collagen scaffolds, Journal of tissue engineering and regenerative medicine (2012).

[159] A. Bigi, G. Cojazzi, S. Panzavolta, N. Roveri, K. Rubini, Stabilization of gelatin films by crosslinking with genipin, Biomaterials 23(24) (2002) 4827-32.

[160] A. Grosberg, P.W. Alford, M.L. McCain, K.K. Parker, Ensembles of engineered cardiac tissues for physiological and pharmacological study: heart on a chip, Lab on a chip 11(24) (2011) 4165-73.

[161] M.A. Bray, W.J. Adams, N.A. Geisse, A.W. Feinberg, S.P. Sheehy, K.K. Parker, Nuclear morphology and deformation in engineered cardiac myocytes and tissues, Biomaterials 31(19) (2010) 5143-50.

[162] L. Xing, X. Yao, K.R. Williams, G.J. Bassell, Negative regulation of RhoA translation and signaling by hnRNP-Q1 affects cellular morphogenesis, Mol Biol Cell 23(8) (2012) 1500-9.

[163] S.R. Coyer, A. Singh, D.W. Dumbauld, D.A. Calderwood, S.W. Craig, E. Delamarche, A.J. Garcia, Nanopatterning reveals an ECM area threshold for focal adhesion assembly and force transmission that is regulated by integrin activation and cytoskeleton tension, J Cell Sci 125(Pt 21) (2012) 5110-23.

[164] D.H. Kim, D. Wirtz, Focal adhesion size uniquely predicts cell migration, FASEB journal : official publication of the Federation of American Societies for Experimental Biology 27(4) (2013) 1351-61.

[165] N.W. Roehm, G.H. Rodgers, S.M. Hatfield, A.L. Glasebrook, An improved colorimetric assay for cell proliferation and viability utilizing the tetrazolium salt XTT, Journal of immunological methods 142(2) (1991) 257-65.

[166] J.W. Bjork, L.A. Meier, S.L. Johnson, Z.H. Syedain, R.T. Tranquillo, Hypoxic culture and insulin yield improvements to fibrin-based engineered tissue, Tissue engineering. Part A 18(7-8) (2012) 785-95.

[167] M. Han, J.K. Wen, B. Zheng, Y. Cheng, C. Zhang, Serum deprivation results in redifferentiation of human umbilical vascular smooth muscle cells, Am J Physiol Cell Physiol 291(1) (2006) C50-8.

[168] L.H. Romer, K.G. Birukov, J.G. Garcia, Focal adhesions: paradigm for a signaling nexus, Circ Res 98(5) (2006) 606-16.

[169] L.A. Taber, J.D. Humphrey, Stress-modulated growth, residual stress, and vascular heterogeneity, J Biomech Eng 123(6) (2001) 528-35.

[170] A. Ramasubramanian, L.A. Taber, Computational modeling of morphogenesis regulated by mechanical feedback, Biomech Model Mechanobiol 7(2) (2008) 77-91.

[171] P.W. Alford, J.D. Humphrey, L.A. Taber, Growth and remodeling in a thick-walled artery model: effects of spatial variations in wall constituents, Biomechanics and modeling in mechanobiology 7(4) (2008) 245-62.

[172] G. Sommer, G.A. Holzapfel, 3D constitutive modeling of the biaxial mechanical response of intact and layer-dissected human carotid arteries, Journal of the mechanical behavior of biomedical materials 5(1) (2012) 116-28.

[173] P.N. Watton, N.A. Hill, M. Heil, A mathematical model for the growth of the abdominal aortic aneurysm, Biomech Model Mechanobiol 3(2) (2004) 98-113.

[174] J.K. Cheng, I. Stoilov, R.P. Mecham, J.E. Wagenseil, A fiber-based constitutive model predicts changes in amount and organization of matrix proteins with development and disease in the mouse aorta, Biomech Model Mechanobiol 12(3) (2013) 497-510.

[175] B.J. Doyle, A.J. Cloonan, M.T. Walsh, D.A. Vorp, T.M. McGloughlin, Identification of rupture locations in patient-specific abdominal aortic aneurysms using experimental and computational techniques, J Biomech 43(7) (2010) 1408-16.

[176] G. Olivetti, P. Anversa, M. Melissari, A.V. Loud, Morphometry of medial hypertrophy in the rat thoracic aorta, Laboratory investigation; a journal of technical methods and pathology 42(5) (1980) 559-65.

[177] R. Nissen, G.J. Cardinale, S. Udenfriend, Increased turnover of arterial collagen in hypertensive rats, Proc Natl Acad Sci U S A 75(1) (1978) 451-3.

[178] P. Fridez, A. Makino, D. Kakoi, H. Miyazaki, J.J. Meister, K. Hayashi, N. Stergiopulos, Adaptation of conduit artery vascular smooth muscle tone to induced hypertension, Ann Biomed Eng 30(7) (2002) 905-16.

[179] R.L. Gleason, J.D. Humphrey, A mixture model of arterial growth and remodeling in hypertension: altered muscle tone and tissue turnover, Journal of vascular research 41(4) (2004) 352-63.

[180] R.L. Gleason, L.A. Taber, J.D. Humphrey, A 2-D model of flow-induced alterations in the geometry, structure, and properties of carotid arteries, J Biomech Eng 126(3) (2004) 371-81.

[181] A. Rachev, N. Stergiopulos, J.J. Meister, A model for geometric and mechanical adaptation of arteries to sustained hypertension, J Biomech Eng 120(1) (1998) 9-17.

[182] K.A. Beningo, M. Dembo, I. Kaverina, J.V. Small, Y.L. Wang, Nascent focal adhesions are responsible for the generation of strong propulsive forces in migrating fibroblasts, The Journal of cell biology 153(4) (2001) 881-8.

[183] J. Stricker, Y. Aratyn-Schaus, P.W. Oakes, M.L. Gardel, Spatiotemporal constraints on the force-dependent growth of focal adhesions, Biophysical journal 100(12) (2011) 2883-93.

[184] M.R. Douglas, M. Daniel, C. Lagord, J. Akinwunmi, A. Jackowski, C. Cooper, M. Berry, A. Logan, High CSF transforming growth factor beta levels after subarachnoid haemorrhage: association with chronic communicating hydrocephalus, J Neurol Neurosurg Psychiatry 80(5) (2009) 545-50.

[185] R.L. Macdonald, B. Weir, Cerebral Vasospasm, Academic Press, San Diego, 2001.

[186] P. Gaetani, F. Tancioni, G. Grignani, F. Tartara, E.M. Merlo, A. Brocchieri, R. Rodriguez y Baena, Platelet derived growth factor and subarachnoid haemorrhage: a study on cisternal cerebrospinal fluid, Acta Neurochir (Wien) 139(4) (1997) 319-24.

[187] P.W. Alford, B.E. Dabiri, J.A. Goss, M.A. Hemphill, M.D. Brigham, K.K. Parker, Blast-induced phenotypic switching in cerebral vasospasm, Proc Natl Acad Sci U S A 108(31) (2011) 12705-10.

[188] J.R. Tse, A.J. Engler, Preparation of hydrogel substrates with tunable mechanical properties, Curr Protoc Cell Biol Chapter 10 (2010) Unit 10.16.

[189] Y. Aratyn-Schaus, P.W. Oakes, J. Stricker, S.P. Winter, M.L. Gardel, Preparation of complaint matrices for quantifying cellular contraction, J Vis Exp (46) (2010).

[190] Q. Tseng, E. Duchemin-Pelletier, A. Deshiere, M. Balland, H. Guillou, O. Filhol, M. Théry, Spatial organization of the extracellular matrix regulates cell-cell junction positioning, Proc Natl Acad Sci U S A 109(5) (2012) 1506-11.

[191] K. Kitazawa, T. Tada, Elevation of transforming growth factor-beta 1 level in cerebrospinal fluid of patients with communicating hydrocephalus after subarachnoid hemorrhage, Stroke 25(7) (1994) 1400-4.

[192] Y. Fujii, Thrombin-antithrombin complex levels in subarachnoid hemorrhage, J Neurosurg 88(3) (1998) 614-5.

[193] D.A. Evans, H.H. Funkenstein, M.S. Albert, P.A. Scherr, N.R. Cook, M.J. Chown, L.E. Hebert, C.H. Hennekens, J.O. Taylor, Prevalence of Alzheimer's disease in a community population of older persons. Higher than previously reported, JAMA 262(18) (1989) 2551-6.

[194] T.E. Golde, C.B. Eckman, S.G. Younkin, Biochemical detection of Abeta isoforms: implications for pathogenesis, diagnosis, and treatment of Alzheimer's disease, Biochim Biophys Acta 1502(1) (2000) 172-87.

[195] B.V. Zlokovic, R. Deane, A.P. Sagare, R.D. Bell, E.A. Winkler, Low-density lipoprotein receptor-related protein-1: a serial clearance homeostatic mechanism controlling Alzheimer's amyloid beta-peptide elimination from the brain, J Neurochem 115(5) (2010) 1077-89.

[196] N.C. Alonzo, B.T. Hyman, G.W. Rebeck, S.M. Greenberg, Progression of cerebral amyloid angiopathy: accumulation of amyloid-beta40 in affected vessels, J Neuropathol Exp Neurol 57(4) (1998) 353-9.

[197] Y. Shinkai, M. Yoshimura, Y. Ito, A. Odaka, N. Suzuki, K. Yanagisawa, Y. Ihara, Amyloid beta-proteins 1-40 and 1-42(43) in the soluble fraction of extra- and intracranial blood vessels, Ann Neurol 38(3) (1995) 421-8.

[198] A.E. Roher, J.D. Lowenson, S. Clarke, A.S. Woods, R.J. Cotter, E. Gowing, M.J. Ball, beta-Amyloid-(1-42) is a major component of cerebrovascular amyloid deposits: implications for the pathology of Alzheimer disease, Proc Natl Acad Sci U S A 90(22) (1993) 10836-40.

[199] H.V. Vinters, D.L. Secor, S.L. Read, J.G. Frazee, U. Tomiyasu, T.M. Stanley, J.A. Ferreiro, M.A. Akers, Microvasculature in brain biopsy specimens from patients with Alzheimer's disease: an immunohistochemical and ultrastructural study, Ultrastruct Pathol 18(3) (1994) 333-48.

[200] A. Christov, J. Ottman, L. Hamdheydari, P. Grammas, Structural changes in Alzheimer's disease brain microvessels, Curr Alzheimer Res 5(4) (2008) 392-5.

[201] J.D. Humphrey, K.R. Rajagopal, A constrained mixture model for arterial adaptations to a sustained step change in blood flow, Biomech Model Mechanobiol 2(2) (2003) 109-26.

[202] M. Lefevre, R.B. Rucker, Aorta elastin turnover in normal and hypercholesterolemic Japanese quail, Biochim Biophys Acta 630(4) (1980) 519-29.

[203] E.C. Davis, Stability of elastin in the developing mouse aorta: a quantitative radioautographic study, Histochemistry 100(1) (1993) 17-26.

[204] S.M. Steelman, Q. Wu, H.P. Wagner, A.T. Yeh, J.D. Humphrey, Perivascular tethering modulates the geometry and biomechanics of cerebral arterioles, J Biomech 43(14) (2010) 2717-21.

[205] J.D. Humphrey, J.F. Eberth, W.W. Dye, R.L. Gleason, Fundamental role of axial stress in compensatory adaptations by arteries, J Biomech 42(1) (2009) 1-8.

[206] L. Cardamone, A. Valentín, J.F. Eberth, J.D. Humphrey, Origin of axial prestretch and residual stress in arteries, Biomech Model Mechanobiol 8(6) (2009) 431-46.

[207] A. Kamiya, R. Bukhari, T. Togawa, Adaptive regulation of wall shear stress optimizing vascular tree function, Bull Math Biol 46(1) (1984) 127-37.

[208] H.D. Intengan, L.Y. Deng, J.S. Li, E.L. Schiffrin, Mechanics and composition of human subcutaneous resistance arteries in essential hypertension, Hypertension 33(1 Pt 2) (1999) 569-74.

[209] T. Bachhuber, N. Katzmarski, J.F. McCarter, D. Loreth, S. Tahirovic, F. Kamp, C. Abou-Ajram, B. Nuscher, A. Serrano-Pozo, A. Müller, M. Prinz, H. Steiner, B.T. Hyman, C. Haass, M. Meyer-Luehmann, Inhibition of amyloid-β plaque formation by α-synuclein, Nat Med 21(7) (2015) 802-7.

[210] P.W. Oakes, S. Banerjee, M.C. Marchetti, M.L. Gardel, Geometry regulates traction stresses in adherent cells, Biophys J 107(4) (2014) 825-33.

[211] Z. Win, G.D. Vrla, K.E. Steucke, E.N. Sevcik, E.S. Hald, P.W. Alford, Smooth muscle architecture within cell-dense vascular tissues influences functional contractility, Integr Biol (Camb) 6(12) (2014) 1201-10.

[212] S.S. Mok, B.J. Turner, K. Beyreuther, C.L. Masters, C.J. Barrow, D.H. Small, Toxicity of substrate-bound amyloid peptides on vascular smooth muscle cells is enhanced by homocysteine, Eur J Biochem 269(12) (2002) 3014-22.

[213] J. Davis, D.H. Cribbs, C.W. Cotman, W.E. Van Nostrand, Pathogenic amyloid beta-protein induces apoptosis in cultured human cerebrovascular smooth muscle cells, Amyloid 6(3) (1999) 157-64.

[214] J. Davis-Salinas, S.M. Saporito-Irwin, C.W. Cotman, W.E. Van Nostrand, Amyloid beta-protein induces its own production in cultured degenerating cerebrovascular smooth muscle cells, J Neurochem 65(2) (1995) 931-4.

[215] S.B. Domnitz, E.M. Robbins, A.W. Hoang, M. Garcia-Alloza, B.T. Hyman, G.W. Rebeck, S.M. Greenberg, B.J. Bacskai, M.P. Frosch, Progression of cerebral amyloid angiopathy in transgenic mouse models of Alzheimer disease, J Neuropathol Exp Neurol 64(7) (2005) 588-94.

[216] R.D. Bell, R. Deane, N. Chow, X. Long, A. Sagare, I. Singh, J.W. Streb, H. Guo, A. Rubio, W. Van Nostrand, J.M. Miano, B.V. Zlokovic, SRF and myocardin regulate LRP-mediated amyloid-beta clearance in brain vascular cells, Nat Cell Biol 11(2) (2009) 143-53.

[217] G. Perry, M.A. Smith, C.E. McCann, S.L. Siedlak, P.K. Jones, R.P. Friedland, Cerebrovascular muscle atrophy is a feature of Alzheimer's disease, Brain Res 791(1-2) (1998) 63-6.

[218] A. Viswanathan, S.M. Greenberg, Cerebral amyloid angiopathy in the elderly, Ann Neurol 70(6) (2011) 871-80.

[219] X. Wang, A. Xing, C. Xu, Q. Cai, H. Liu, L. Li, Cerebrovascular hypoperfusion induces spatial memory impairment, synaptic changes, and amyloid-β oligomerization in rats, J Alzheimers Dis 21(3) (2010) 813-22.

[220] P.H. Axelsen, H. Komatsu, I.V. Murray, Oxidative stress and cell membranes in the pathogenesis of Alzheimer's disease, Physiology (Bethesda) 26(1) (2011) 54-69.

[221] Y. Zhao, B. Zhao, Oxidative stress and the pathogenesis of Alzheimer's disease, Oxid Med Cell Longev 2013 (2013) 316523.

[222] S.S. Rensen, P.A. Doevendans, G.J. van Eys, Regulation and characteristics of vascular smooth muscle cell phenotypic diversity, Neth Heart J 15(3) (2007) 100-8.

[223] F.C. Bronfman, C. Soto, L. Tapia, V. Tapia, N.C. Inestrosa, Extracellular matrix regulates the amount of the beta-amyloid precursor protein and its amyloidogenic fragments, J Cell Physiol 166(2) (1996) 360-9.

[224] U. Hedin, B.A. Bottger, E. Forsberg, S. Johansson, J. Thyberg, Diverse effects of fibronectin and laminin on phenotypic properties of cultured arterial smooth muscle cells, J Cell Biol 107(1) (1988) 307-19.

[225] S. Huang, D.E. Ingber, Cell tension, matrix mechanics, and cancer development, Cancer Cell 8(3) (2005) 175-6.

[226] A.W. Feinberg, A. Feigel, S.S. Shevkoplyas, S. Sheehy, G.M. Whitesides, K.K. Parker, Muscular thin films for building actuators and powering devices, Science 317(5843) (2007) 1366-70.

[227] E.S. Hald, K.E. Steucke, J.A. Reeves, Z. Win, P.W. Alford, Microfluidic Genipin Deposition Technique for Extended Culture of Micropatterned Vascular Muscular Thin Films, J Vis Exp (100) (2015) e52971.

[228] G.N. Mir, W.H. Lawrence, J. Autian, Toxicological and pharmacological actions of methacrylate monomers. I. Effects on isolated, perfused rabbit heart, J Pharm Sci 62(5) (1973) 778-82.

[229] A.R. Singh, W.H. Lawrence, J. Autian, Embryonic-fetal toxicity and teratogenic effects of a group of methacrylate esters in rats, J Dent Res 51(6) (1972) 1632-8.

[230] M. Butler, Processes with animal cell and tissue cultues, in: H.J. Rehm, G. Reed (Eds.), Biotechnology: A comprehensive treatise, VCH Verlag1988, pp. 249-316.

[231] R.L. Hamilton, Lewy bodies in Alzheimer's disease: a neuropathological review of 145 cases using alpha-synuclein immunohistochemistry, Brain Pathol 10(3) (2000) 378-84.

[232] E. Bertrand, E. Lewandowska, T. Stepień, G.M. Szpak, E. Pasennik, J. Modzelewska, Amyloid angiopathy in idiopathic Parkinson's disease. Immunohistochemical and ultrastructural study, Folia Neuropathol 46(4) (2008) 255-70.

Appendix A. Vasospasm-on-a-Chip: Isolation of Subarachnoid Hemorrhage-Associated Factors

This appendix contains material based on a previously submitted research abstract for the *2015 Summer Biomechanics, Bioengineering, and Biotransport Conferences*.

A.1 Introduction

Cerebral vasospasm **(CVS)** is a potentially lethal disease characterized by acute hypercontractility followed by prolonged remodeling, lumen occlusion, and ischemia, typically occurring 3-7 days post-injury [132]. One common precursor implicated in CVS development is subarachnoid hemorrhage **(SAH)**, which results in the release of growth and clotting factors (e.g. PDGF, TGF-β, thrombin) in the subarachnoid space. These factors are thought to act on vascular smooth muscle contractile tone via complex biochemical pathways [74]. However, it is not clear which, and to what extent, individual factors (or their combinatorial effects) induce CVS.

Due to the chronic nature of vascular disease, extension of culture times for *in vitro* models is desired. We developed a patterned protein deposition technique for extending culture of VSMCs on PDMS with genipin [130, 227]. We combined this microfluidic protein deposition technique for engineering vascular tissues with a previously developed muscular thin film **(MTF)** technique, allowing for chronic measurement of vascular contractility. Here, we add a novel isolation chamber device designed to allow isolated delivery of SAH-borne factors to engineered vascular tissues on a single chip. We employ a dose-response experimental strategy to investigate the critical SAH-borne factors responsible for pathological CVS vascular mechanics.

A.2 Methods

A.2.1 Tissue Fabrication and Isolation

Photolithographic techniques were used to fabricate microfluidic protein deposition devices with alternating lines of 10-µm width with 10-µm pitch in two rows of five blocks of 2-mm width and 4-mm length to yield a 2x5 array of engineered arterial lamella (Fig. A.1 A). Genipin (5 mg/ml) and fibronectin (50 µg/ml) were sequentially drawn through the devices applied to glass cover slips coated in Sylgard 184 PDMS as in Chapter 3. Microfluidic devices were removed and acrylic isolation chamber devices were placed on the patterned substrates. These devices were fabricated prior to experimentation using a laser cutter, yielding a single array of reservoirs of 2-mm width, 10-mm length, and 6-mm height (Fig. A.1 B). Human umbilical artery VSMCs were then seeded into each isolation chamber at a cell seeding density of 80,000 cells/cm^2. After 24h, confluent, aligned arterial lamellae mimics formed within each chamber (Fig. A.1 B) and were then treated with serum-free medium to induce a contractile phenotype [167]. After 24h in serum-free medium, each chamber was treated with one of five solutions: control (serum-free medium), 10^{-12} M, 10^{-11} M, 10^{-10} M, and 10^{-9} M TGF-β1 (or other SAH factor of interest) in serum-free medium (Fig. A.1 B, Factor Concentration). To simplify handling of samples and improve maintenance of isolation chamber seal, four chips were fabricated in a single acrylic clamping system (Fig. A.1 C). Dose-response treatment solutions were refreshed every 24h for up to seven days of treatment.

A.2.2 Stress Measurement

Contraction of independently-treated microtissues was measured using a previously developed MTF model [160]. At a treatment time point of interest, each of five tissues on a single chip was cut and released via the dissolution of poly(N-iso-propylacrylamide) below 32°C to form a single MTF (Fig. A.2 A). Stress

generation in the cell layer causes the released MTF to curl. The radius of curvature can be used to calculate contractile stress, as in [160]. We determine two important stresses: 1) induced contractility via stimulation with the vasoconstrictor endothelin-1 **(ET-1)** and 2) basal tone via tissue relaxation with HA-1077, a rho-kinase inhibitor.

A.3 Results

Functional output for all treatments were simultaneously measured (Fig. A.2) for up to seven days of treatment. At 24h treatment, we found increasing raw stress values with increasing TGF-β concentration (Fig. A.2 B). We found a 4-fold increase in both normalized basal tone and normalized ET-1-induced contractility in tissues treated with 10^{-11} and 10^{-10} M TGF-β (Fig. A.2 C, D). Tissues cultured in the acrylic isolation chambers started to deteriorate after 48h (Fig. A.3), eventually all leading to complete delamination by 120h. All treatment levels and controls resulted in a similar pattern of deterioration, starting in the middle of the isolation chamber. Small strips of tissue remained for longer periods along the wall edges, as well as the branched portion of the microfluidic patterning at either end of the chamber (not shown).

A.4 Discussion

Here, we present an *in vitro* assay for isolated treatment and measurement of microtissue stress generation over CVS-relevant time course. Our design allows dose-response experimentation with other water-soluble SAH-borne factors of interest. Investigation of the effects of PDGF and thrombin, in addition to results for TGF-β (Fig. A.2), provides a platform to investigate the direct effect of these factors on vascular mechanics. We can employ a factorial experimental design to determine factor-level combinations that induce acute hyper-contractility followed by a shift to a synthetic remodeling VSM phenotype experiment. We will use this

design to assess the relative importance of these SAH-borne factors, both individually and in combination, yielding further understanding of the underlying disease mechanisms and possibly illuminating desirable treatment strategies to combat the pathological vascular mechanical response in CVS. Further, the ability to recapitulate CVS progression in an on-a-chip system may allow future development of our technique as a pharmaceutical assay.

Another key feature of our design is our ability to conduct experiments over disease-relevant time courses. Previous microcontact printing methods for engineering arterial lamella showed loss of tissue integrity as early as four days in culture [130]. We can now perform these assays up to seven days by utilizing genipin to extend culture of VSMCs [130, 227]. However, our current isolation chamber design results in an attenuation of this improved temporal viability. There are two likely causes for this deleterious result: 1) leaching of cytotoxic material from acrylic isolation chamber devices or 2) diffusion-limited delivery of oxygen or convection-limited delivery of nutrients within the media. A variety of acrylic monomers have been implicated in reduced contraction of heart muscle in rabbits [228], as well as differential effects (strong vs. weak) on viability and malformation of rat fetuses [229]. The melting of our acrylic devices during laser cutting could result in the formation of cytotoxic residues that leach into the culture medium filling the device. Oxygen transfer may be affected with our device geometry. Previous work has shown the importance of oxygen transfer rate, which is dependent on gaseous diffusion from the head space of the culture medium [230]. While these possibilities seem most likely, both seem to be counterintuitive explanations for our observed maintenance of cell attachment at the edges of the device. Future work to investigate the diffusion limits of the device is necessary to determine necessary design modifications to allow for dose-response studies of vascular mechanics over disease-relevant time courses.
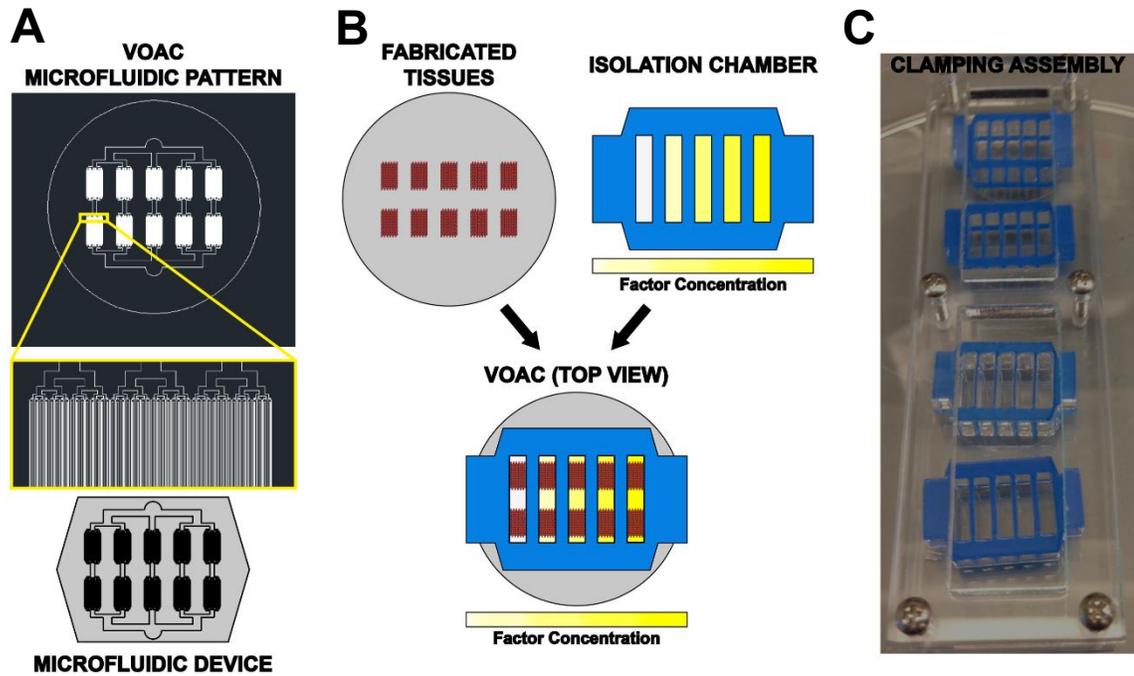
**Figure A.1. Schematic of vasospasm-on-a-chip (VOAC) model.**
(A) Photolithographic mask design for 10x10 μm channel tissue pattern and resulting microfluidic device. (B) Schematic representation of isolation chamber device application to patterned tissues yielding VOAC with increasing factor concentration applied from left to right. (C) Clamping assembly for concurrent culture of four VOAC systems.
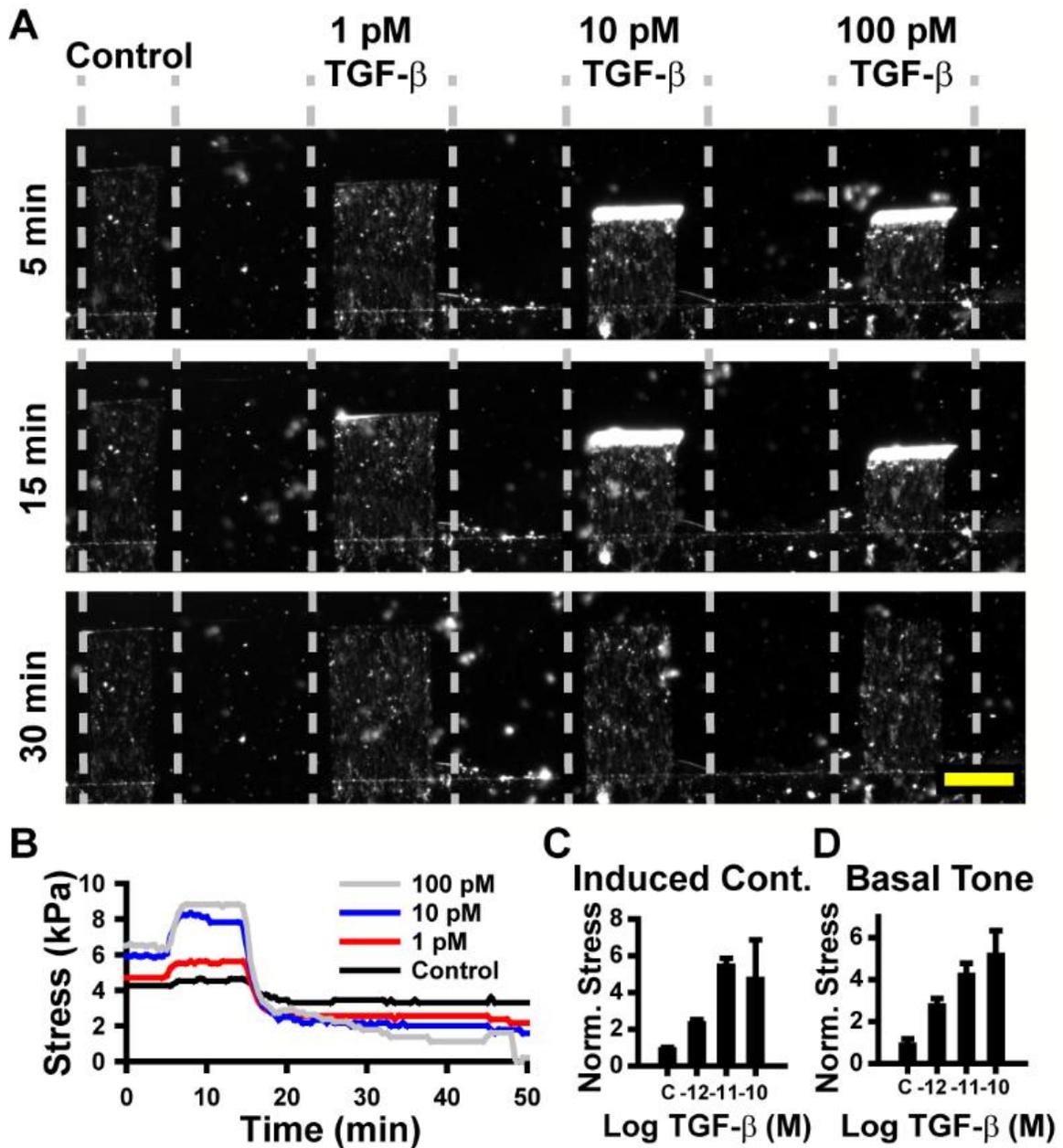
Figure A.2. SAH-associated TGF-beta increases vascular contractility.
(A) Brightfield images of released MTFs on a single, VOAC construct (increasing TGF-β concentration from left to right); Scale Bar: 1 mm. (B) Representative functional contractility assay and characteristic stress curve. (C) Endothelin-1-induced contraction increases with increased concentration of TGF-β (Mean ± Standard Error). (D) Basal tone increases with increased concentration of TGF-β (Mean ± Standard Error). Stress normalized to control values (fold increases).

24h Serum-starved Medium **48h Serum-starved Medium**
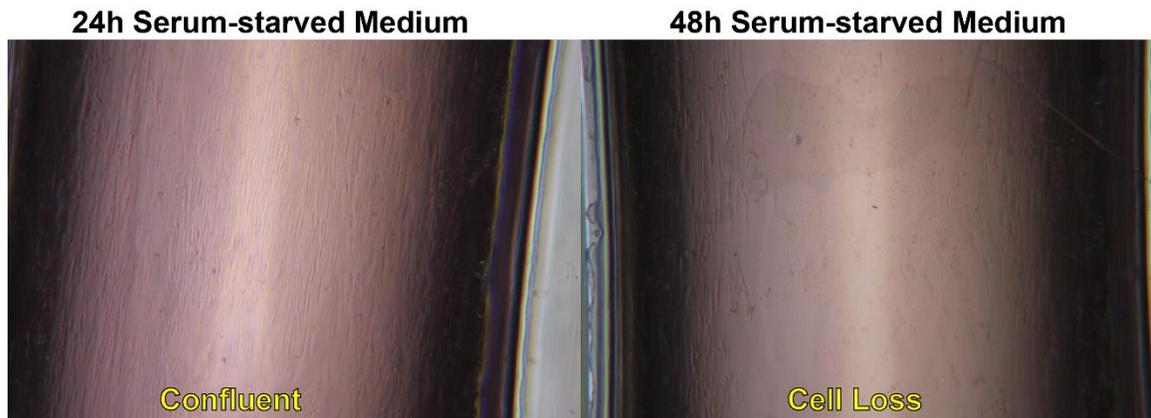
Figure A.3. Culture in isolation chamber device results in delamination between 24h and 48h in serum-starved medium.
Note: VSMCs are lost in the middle of the reservoir, but remain attached and viable at edges.

Appendix B. Parameter Study for Thin-Walled Cerebral Arterial Model

This appendix contains related material not included in an invited original research article in press at *JBME*. **Hald ES**, Timm CD, and Alford PW. In Press. Amyloid Beta Influences Vascular Smooth Muscle Contractility and Mechano-Adaptation. In Press.

B.1 Summary

In developing our thin-walled cerebral arterial model in Chapter 5, we assumed specific values for our material parameters. Some parameters were chosen to match literature values, while others were estimated. To investigate the effect each of these material parameters has on the mechanics of our model artery at homeostasis, we performed parameter studies at a homeostatic target stress of 75 kPa. We generated pressure-radius curves similar to those reported in Figs. 5.4C, 5.5C, and 5.6A. The material parameters directly influence the strain energy density equations for each of the arterial constituents (Eqs. 5.11-5.13 and rewritten here as Eqs. B.1-B.3).

For elastin, the strain energy density function is

$$W^e = \frac{C^e}{2}(\lambda_\theta^{*e2} + \lambda_z^{*e2} + \lambda_\theta^{*e-2}\lambda_z^{*e-2} - 3) \tag{Eq. B.1}$$

where C^e is the elastin material parameter, taken to be 24.91 kPa based on Cheng et al. [174] for all model outputs described in Chapter 5. Since elastin does not significantly remodel post-birth [203], we assumed that the elastin in the model was at a mature homeostatic stretch λ_o^e in the loaded configuration so that $\lambda_\theta^{*e} = \lambda_z^{*e} = \lambda_o^e$. In all model outputs described in Chapter 5, we let $\lambda_o^e = 1.1$.

For collagen, the strain energy density function is

$$W^c = \sum_{k=1}^{2} \frac{C^c}{\beta}\left(e^{\beta(I_4^{*k}-1)^2} - 1\right) \tag{Eq. B.2}$$

where C^c and β are collagen material parameters taken to be 42.32 kPa and 0.08, respectively, based on Cheng et al. [174] for all model outputs described in Chapter 5. I_4 is the 4th strain invariant given by $I_4^* = C_{\theta\theta}^* \cos^2(\alpha^k) + 2C_{\theta z}^* \sin(\alpha^k)\cos(\alpha^k) + C_{zz}^* \sin^2(\alpha^k)$, where C_{ij}^* is the i,j component of the elastic right Cauchy-Green tensor, defined as $\boldsymbol{C}^* = \boldsymbol{F}^{*T} \cdot \boldsymbol{F}^*$, and α is the angle of the collagen fibers with respect to the undeformed circumferential orientation. Humphrey and Rajagopal proposed that when collagen turns over, old fibers are replaced by new fibers at a preferred stretch ratio λ_o^c [201]. Here, we assume that the vessel is at homeostasis and has been for some time, so that $\lambda_i^{*c} = \lambda_o^c$ for all fibers in the loaded configuration, and we let $\lambda_o^c = 1.2$ for all model outputs described in Chapter 5.

For smooth muscle, the strain energy density is

$$W^m = \frac{C^m}{2}(I_1^* - 3) + \frac{A^m}{2}(\lambda_\theta^{*m} - 1)^2 \qquad \text{(Eq. B.3)}$$

where C^m and A^m are the passive and active material parameters taken to be 10 kPa and 100 kPa, respectively, for all model outputs described in Chapter 5. I_1^* is the first strain invariant with respect to the zero-stress configuration, given by $I_1^* = \lambda_r^{*m\,2} + \lambda_\theta^{*m\,2} + \lambda_z^{*m\,2}$. Muscle acts to adapt the vessel quickly to changes in its mechanics via contraction, but to do so, it must maintain a homeostatic partially-contracted state described by the stress-free cell shortening λ_{ao} [9]. In all models, we assumed that the loaded active artery is at this homeostasis, and VSMC contractile cytoskeletons are primarily oriented circumferentially, so that $\boldsymbol{A} = diag[1, \lambda_{ao}, 1]$, where $\lambda_{ao} = 0.8$. VSMCs can also grow via hypertrophy or proliferation to alter their stress. Though axial growth and remodeling plays an important role in vessel mechanics [73, 205, 206], here, we ignored its effect and only included radial growth (thickening) λ_{gr} and circumferential growth $\lambda_{g\theta}$. Thus, the growth tensor is given by $\boldsymbol{G} = diag[\lambda_{gr}, \lambda_{g\theta}, 1]$.

First, we considered the extracellular matrix material parameters used in the model, C^e, C^c, and β. These parameters influence Eqs. B.1 and B.2. Pressure-radius curves for the study of the elastin material parameter C^e show minimal effect on the mechanics of our model artery (Fig. B.1 A). In studying the two collagen material parameters C^c and β, we found increased stiffness in the modeled artery as we increased both parameters, with a more pronounced increase when we increased the exponential collagen material parameter β (Fig. B.1 B,C). These studies yielded expected outcomes, as the elastin plays a minimal role in the mechanical response of the artery to loading. The increase in the collagen material parameters corresponds with increased stiffness of the material, which manifests in the stiffer mechanical behavior observed at the tissue level in both the active and the passive responses to loading.

Next, we considered the effects of the homeostatic stretch ratios λ_o^e and λ_o^c for elastin and collagen fibers, respectively. While changing λ_o^e, we found minimal effect on vessel stiffness (Fig. B.2 A). For increasing λ_o^c, we observed corresponding increases in vessel stiffness (Fig. B.2 B), similar to those observed for increases in β (Fig. B.1 C). This is an expected outcome, as increases in λ_o^c also result in increased magnitude of the exponential term in Equation B.2, leading to stiffer behavior by the vessel for both active and passive contributions.

Finally, we considered the effects of the passive and active smooth muscle material parameters C^m and A^m, respectively. Significantly increasing the passive smooth muscle material parameter C^m results in pronounced increase in the stiffness of the model vessel (Fig. B.3 A). The separation in the active and passive mechanical response is also slightly decreased as C^m is increased, suggesting a larger contribution of the passive mechanics to the overall increased stiffness of the vessel. This is an expected result due to the increased dominance of the neo-Hookean passive term in Equation B.3 as C^m is increased. In the study of the active smooth muscle material parameter A^m, we found slightly increased stiffness in the

active behavior of the vessel with minimal response in the passive behavior (Fig. B.3 B).

Taken together, these parameter studies suggest that the passive behavior is critically affected by effective increases in constituent stiffness, specifically for collagen and smooth muscle, as modulated by changing material parameters. In these cases, the active response is also changed, resulting in a stiffer mechanical response to arterial loading. The active response of the smooth muscle shows less direct influence due to associated parameter manipulation. This suggests that our model is not as susceptible to altered mechanics due to changes in material parameters that directly affect the active contractile response of the vessel, similar to the limited effects of changes in elastin properties.
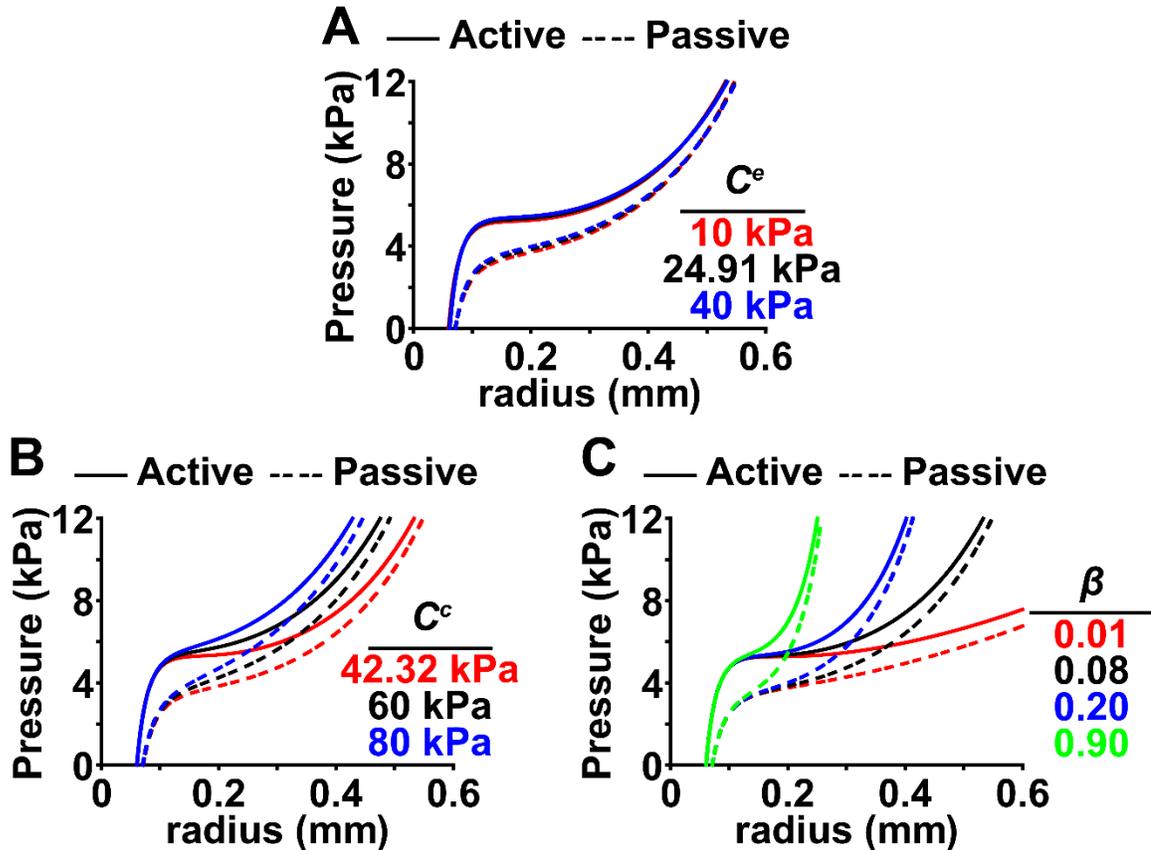
Figure B.1. Parameter studies of elastin and collagen material parameters
(A) Pressure-radius curves for active (solid lines) and passive (dashed lines) mechanical responses for modulated value of the elastin material parameter C^e in Eq. B.1 (Red: 10 kPa, Black: 24.91 kPa [value for Chapter 5 model outputs], Blue: 40 kPa; decreasing value for C^e from top left to bottom right for both active and passive curves). (B) Pressure-radius curves for active (solid lines) and passive (dashed lines) mechanical responses for modulated value of the linear collagen material parameter C^c in Eq. B.2 (Red: 42.32 kPa [value for Chapter 5 model outputs], Black: 60 kPa, Blue: 80 kPa; decreasing value for C^c from top left to bottom right for both active and passive curves). (C) Pressure-radius curves for active (solid lines) and passive (dashed lines) mechanical responses for modulated value of the exponential collagen material parameter β in Eq. B.2 (Red: 0.01, Black: 0.08 [value for Chapter 5 model outputs], Blue: 0.20, Green: 0.90; decreasing value for β from top left to bottom right for both active and passive curves).
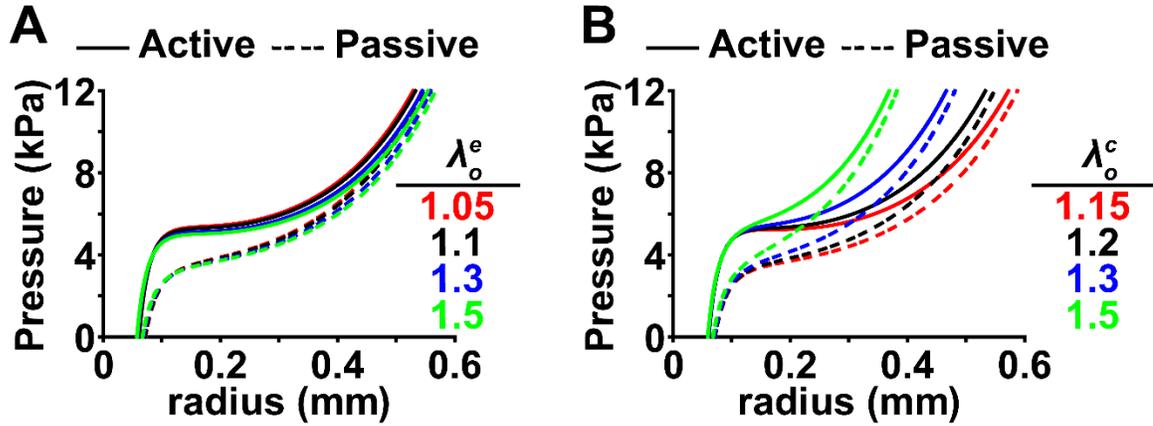
Figure B.2. Parameter studies of elastin and collagen homeostatic stretch ratios

(A) Pressure-radius curves for active (solid lines) and passive (dashed lines) mechanical responses for modulated value of the elastin homeostatic stretch ratio λ_o^e in Eq. B.1 according to the relation $\lambda_\theta^{*e} = \lambda_z^{*e} = \lambda_o^e$ (Red: 1.05, Black: 1.1 [value for Chapter 5 model outputs], Blue: 1.3, Green: 1.5; increasing value for λ_o^e from top left to bottom right for both active and passive curves). (B) Pressure-radius curves for active (solid lines) and passive (dashed lines) mechanical responses for modulated value of the collagen homeostatic stretch ratio λ_o^c, a component of the 4th strain invariant I_4 in Eq. B.2 (Red: 1.15, Black: 1.2 [value for Chapter 5 model outputs], Blue: 1.3, Green: 1.5; decreasing value for λ_o^c from top left to bottom right for both active and passive curves).
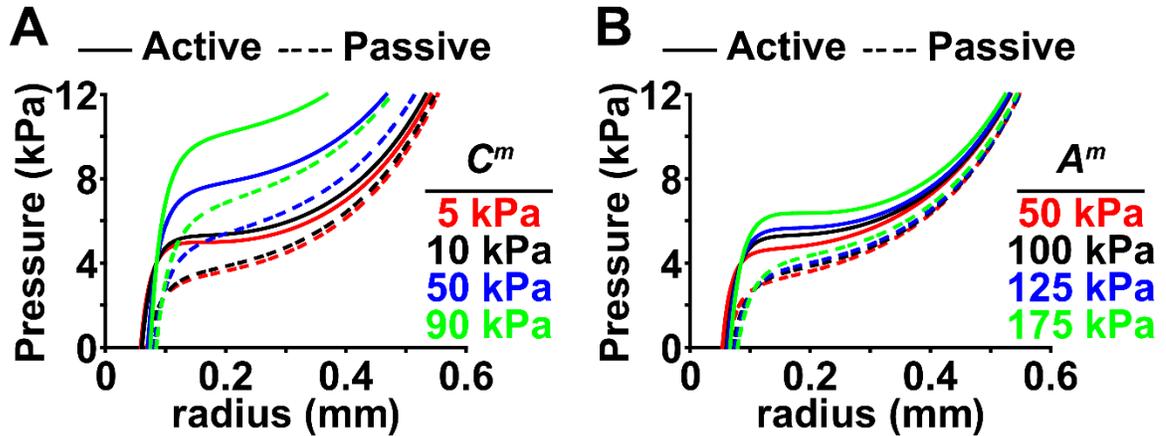
Figure B.3. Parameter studies of the passive and active smooth muscle material parameters
(A) Pressure-radius curves for active (solid lines) and passive (dashed lines) mechanical responses for modulated value of the passive neo-Hookean smooth muscle material parameter C^m in Eq. B.3 (Red: 5 kPa, Black: 10 kPa [value for Chapter 5 model outputs], Blue: 50 kPa, Green: 90 kPa; decreasing value for C^m from top left to bottom right for both active and passive curves). (B) Pressure-radius curves for active (solid lines) and passive (dashed lines) mechanical responses for modulated value of the active smooth muscle material parameter A^m in Eq. B.3 (Red: 50 kPa, Black: 100 kPa [value for Chapter 5 model outputs], Blue: 125 kPa, Green: 175 kPa; decreasing value for A^m from top left to bottom right for both active and passive curves).

Appendix C. Influence of Co-treatment with Alpha Synuclein and Amyloid Beta on Vascular Smooth Muscle Function

This appendix contains related material not included in an invited original research article at *JBME*. Some material included for comparative purposes is modified from the material under review and is reproduced with permission. **Hald ES**, Timm CD, and Alford PW. In Press. Amyloid Beta Influences Vascular Smooth Muscle Contractility and Mechano-Adaptation.

C.1 Summary

In addition to the amyloid hypothesis in Alzheimer's disease progression, studies of other neurodegenerative diseases, such as Parkinson's disease, have suggested there are overlapping effects of disease mechanisms and their impacts on Aβ accumulation. Alpha-synuclein, the hallmark protein implicated in Parkinson's disease, coincidentally accumulates with Aβ plaque formation in over 50% of Alzheimer's cases [231]. Bachhuber et al. found α-synuclein inhibits Aβ plaque formation both *in vivo* and *in vitro*, with ~30% inhibition *in vitro* [209]. We investigated the possible impact of α-synuclein/Aβ co-exposure in vascular tissue and on Aβ plaque formation by treating VSMCs with a combination of 10 μM Aβ (Tocris Bioscience) and 1 μM α-synuclein (rPeptide), but found no inhibition of Aβ plaque coverage of VSMCs (Fig. C.1 A,B). We found a non-significant increasing trend in nuclear eccentricity as Aβ treatment concentration increased, but a significant increase in VSMCs treated with a combination of Aβ and α-synuclein (Fig. C.1 C). Treatment with α-synuclein alone resulted in no change in basal strain energy (Fig. C.2 A). Co-treatment resulted in a significant decrease of basal vascular contractility, consistent with Aβ treatment alone (Fig. C.2 A). Interestingly, there appeared to be some recovery of vasoactive function in VSMCs co-treated with Aβ and α-synuclein (Fig. C.2 B).

Overlaps in neurodegenerative disease pathologies are common and can lead to exacerbated effects [231, 232]. Bertrand et al. showed increased severity of CAA in cases displaying a possible coexistence of Alzheimer's and Parkinson's disease (presence of both Aβ and α-synuclein) [232]. Bachhuber et al. showed that coaggregation of Aβ and α-synuclein resulted in reduced Aβ plaque formation *in vitro* and in the Lewy bodies of Parkinson's rat brain tissue [209]. We did not see this attenuation of plaque formation in our *in vitro* VSMC cultures (Fig. C.1 A,B). We also observed a decrease in VSMC basal tone in cells treated with a combination of Aβ and α-synuclein (Fig. C.2 A). These conflicting results suggest that the location of co-localization of α-synuclein and Aβ may have different outcomes. Specifically, co-localization in the arteries may have limited effect on Aβ plaque formation and influence on VSMC function, whereas coaggregation in neurons leads to reduced Aβ accumulation as observed in [209]. Our results may explain why an increase in CAA severity is observed in cases of overlapping Alzheimer's and Parkinson's pathologies.
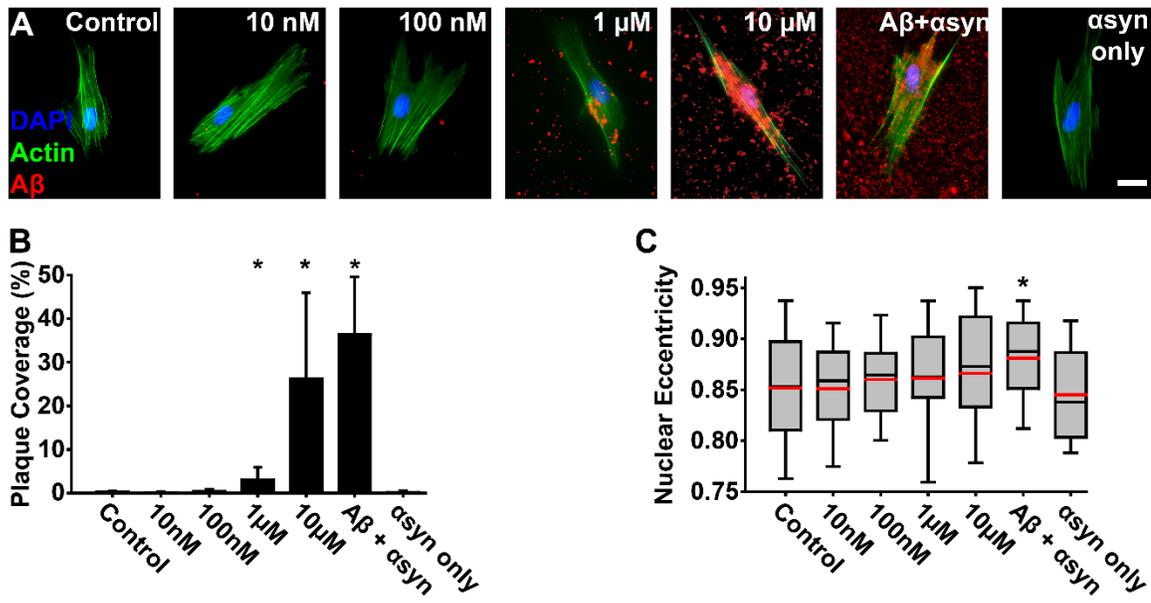
Figure C.1. Co-treatment of VSMCs with Aβ and α-synuclein does not attenuate plaque formation.
(A) Representative immunofluorescent images of single VSMCs for different treatment conditions. Blue: DAPI-stained nuclei, Green: f-action, Red: AB2286-stained Aβ fibrils, Scale Bar: 25 μm. (B) Aβ plaque coverage significantly increases in higher concentrated treatment. Alpha-synuclein does not attenuate Aβ plaque formation. (C) Co-treatment with Aβ and α-synuclein results in significantly increased nuclear eccentricity. *: significant difference, $p < 0.05$.
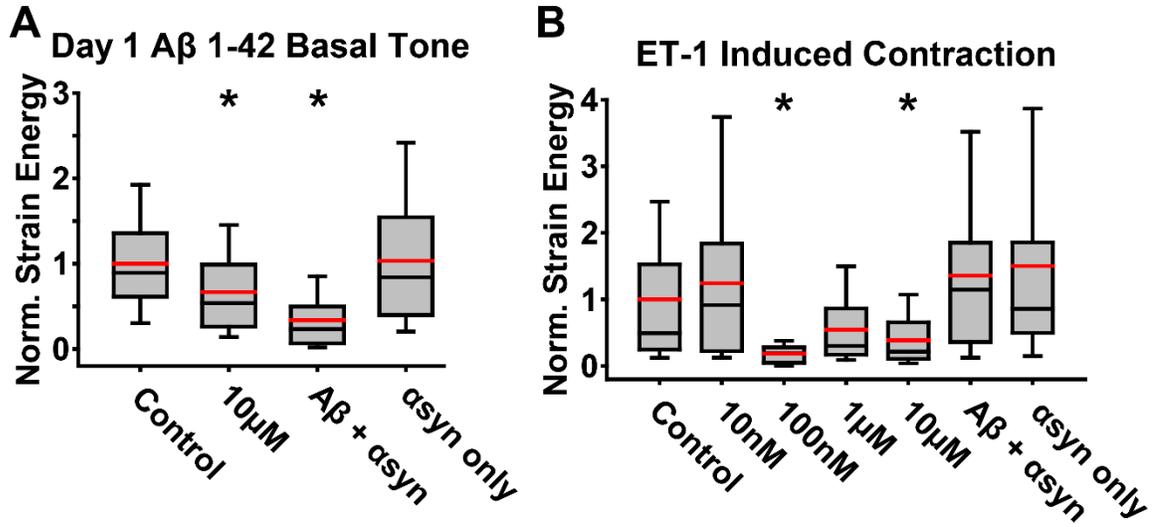
Figure C.2. Effects of Aβ/α-synuclein co-treatment on VSMC functional contractility.
(A) Co-treatment with Aβ/α-synuclein further exacerbates reduction in VSMC basal function. Alpha-synuclein alone has no impact on basal function. (B) Vasoactive response to ET-1 induced contraction is re-gained in VSMCs co-treated with Aβ/α-synuclein. *: significant difference, p<0.05.